AN ABSTRACT OF THE DISSERTATION OF

Caitlyn E. Clark for the degree of Doctor of Philosophy in Mechanical Engineering presented on December 9, 2019.

Title: Risk- and Reliability-Based Design Optimization of Offshore Renewable Energy Systems

Abstract approved: _____

Bryony L. DuPont

Offshore wind and wave energy have the potential to be significant sources of future global electricity production, reduce carbon emissions, decrease dependence on energy importation, and stimulate economic growth in coastal and remote areas. Fixed-foundation and floating offshore wind and wave energy technologies are at different stages of development, but they all have the potential to successfully function in the renewable energy sector if developers can provide reliable, efficient technologies that can survive their harsh environment to be economically profitable. To achieve this, developers need to consider reliability simultaneously with power production and cost early in the design process. This thesis uses risk- and reliability-based design optimization to consider reliability, cost, and performance during subcomponent, device, and system design to enable the exploration of optimal solutions in offshore wind and wave technologies.

The included work advances the state-of-the-art of reliability-based design optimization (RBDO) in offshore renewable energy systems via three research foci: 1) establishing relationships between component reliability, failure costs, power production, and layout optimization of offshore wind arrays, 2) evaluating how geometry optimization of WECs affects component reliability and power production, and 3) quantifying how co-location of offshore wind turbines and wave energy converters (WECs) in the same ocean space affects power production, reliability, and cost.

Through these research foci, this thesis aims to achieve the objective of improving the design and market competitiveness of offshore renewable energy systems by establishing relationships between component reliability and systems optimization and creating methods for including reliability into design at component and system levels.

Risk- and Reliability-Based Design Optimization of Offshore Renewable Energy Systems

by

Caitlyn E. Clark

A DISSERTATION

submitted to

Oregon State University

in partial fulfillment of
the requirements for the
degree of

Doctor of Philosophy

Presented December 9, 2019
Commencement June 2020

Doctor of Philosophy dissertation of Caitlyn E. Clark presented on December 9, 2019.

APPROVED:

Major Professor, representing Mechanical Engineering

Head of the School of Mechanical, Industrial, and Manufacturing Engineering

---

Dean of the Graduate School

I understand that my dissertation will become part of the permanent collection of Oregon State University libraries. My signature below authorizes release of my dissertation to any reader upon request.

Caitlyn E. Clark, Author

ACKNOWLEDGEMENTS

The work contained in this thesis was a collaborative effort spanning multiple institutions and several years, and would not be possible if not for many bright minds and generosity.

To start, this work was supported by funds from the Danish-American Fulbright Commission, the National Renewable Energy Laboratory, and the Ocean Energy Systems Blue Energy Collaborative Scholarship. Thank you to these institutions for their support in making this work possible.

I would like to thank those who contributed to this work. In Chapter 2, Yi Guo (NREL) and Jan Helsen (Vrije Universitet) provided the drivetrain model, and María Iñigo Labairu and Pieter-Jan Daems aided in L_{10} methodology reporting. Also in this Chapter, Jason Jonkman and Kelsey Shaler provided support implementing FAST.Farm. In Chapter 3, Anna Garcia-Teruel (The University of Edinburgh) implemented her power take-off model and Genetic Algorithm to enable the work. The fixed-foundation offshore wind turbine monopile response and fatigue analysis in Chapter 4 was completed by Joey Velard (Aalborg Universitet), and the floating offshore wind turbine mooring cable simulation and fatigue analysis was completed by Guilherme Moura Paredes in Chapter 5. Others that have provided guidance for this work include: Shawn Sheng, Owen Roberts, Walter Musial, Jens Peter Kofoed, Francesco Ferri, John Dalsgaard Sørensen, Simon Ambühl, and David Forehand. Special thanks goes to my graduate committee in providing persistent technical support and guidance through my PhD tenure: Irem Tumer,

Flaxen Conway, Eduardo Cotilla-Sanchez, and Pedro Lomonaco. Thank you to my colleagues at Oregon State University, the Pacific Marine Energy Center, Aalborg Universitet, and the National Renewable Energy Laboratory for your camaraderie and support.

I have enormous gratitude for the personal and professional support from my main mentors. Thank you to Jannie Sønderkær Nielsen for mentoring me during my time at Aalborg University, connecting me to resources to learn, sharing her technical knowledge, and welcoming me into her life. Thank you to Garrett Barter for all that he has taught me during my time at NREL. He has enabled me to pursue my research interests, and continually challenges and inspires me to bridge expertise and rigorously and meticulously chase down answers to scientific questions.

Lastly, I have not the words to express my gratitude for Bryony DuPont. Her persistent guidance, advocacy, and mentorship has enabled my graduate career and enormous personal and professional growth. This graduate experience has been a wild, unforgettable ride, and all the opportunity that I have been so fortunate to receive has been because of her. To all the friends I have met before and along this ride, thank you for all the joy and unforgettable experiences we have shared. And to my parents and sister, thank you for your unparalleled love and support; no victory is sweet, no obstacle surmountable, without you by my side.

TABLE OF CONTENTS

TABLE OF CONTENTS (Continued)

TABLE OF CONTENTS (Continued)

LIST OF FIGURES

LIST OF FIGURES (Continued)

LIST OF FIGURES (Continued)

LIST OF FIGURES (Continued)

LIST OF FIGURES (Continued)

LIST OF FIGURES (Continued)

LIST OF FIGURES (Continued)

LIST OF TABLES

Chapter 1: Introduction

Offshore wind and wave energy have the potential to be significant sources of future global electricity production, reduce carbon emissions, decrease dependence on energy importation, and stimulate economic growth in coastal and remote areas. Available offshore wind and wave energy off the United States (U.S.) Pacific coast alone exceeds U.S. household energy consumption [60, 104], and with population and energy use density growth concentrated along coastlines, these technologies could generate electricity where it is used. While fixed-foundation and floating offshore wind and wave energy technologies are at different stages of development, they all have the potential to successfully function in the renewable energy sector if developers can provide reliable, efficient technologies that can survive their harsh environment to be economically profitable. To achieve this, developers need to consider reliability simultaneously with power production and cost early in the design process.

In this body of work, I develop reliability-based design optimization (RBDO) methods to consider reliability, cost, and performance during subcomponent, device, and system design and enable the exploration of optimal layouts. I aim to expose fundamental relationships between component reliability and systems optimization in offshore wind and wave energy applications. To achieve this, I will characterize reliability across critical failure components and design parameters in

each technology and create optimization algorithms that identify optimal design solutions at both the device and array level. My central idea, based on previously published research, is that the lack of incorporation of reliability into the design process of these systems has substantial techno-economic disadvantages. By investigating key relationships between component reliability and systems optimization, this work will enable offshore renewable energy stakeholders to be better equipped to create market-competitive solutions.

The rationale for this approach is two-fold: 1) many of these foundational relationships between component reliability and systems performance and cost have not yet been quantitatively described, and 2) there is little prior, analogous industry experience to inform emerging technology design. These two barriers render stakeholders unable to use objective methods for implementing reliability metrics into systems design and optimization, and thus fully optimize their energy systems. Further, the computational ability to implement systems optimization through iteratively simulating wind and wave conditions is computationally too expensive. By defining key relationships that govern optimal design and creating computationally-efficient RBDO methods, this work can make quantitative incorporation of reliability more accessible to academic and industrial audiences, who can implement these design methodologies to build a better industry.

The research objective of this body of work is to improve the design and market competitiveness of offshore renewable energy systems by establishing relationships between component reliability and systems optimization, and creating methods for including reliability into design at component and system levels. The work achieves

these objectives and advances the state-of-the-art of reliability-based design optimization (RBDO) in offshore renewable energy systems via three research foci: 1) establishing relationships between component reliability, failure costs, power production, and layout optimization of offshore wind arrays, 2) evaluating how geometry optimization of WECs affects component reliability and power production, and 3) quantifying how co-location of offshore wind turbines and wave energy converters (WECs) in the same ocean space affects power production, reliability, and cost.

The expected significance of this research is that it will incite research in this area by introducing reliability techniques used in other applications as valuable to offshore renewable energy applications, expose foundational relationships between component reliability and systems optimization, and provide information and methods to enable researchers and developers to better design offshore renewable energy systems through incorporation of reliability.

1.1 Current Use of Reliability in Offshore Renewable Energy

While fixed-foundation offshore wind, floating offshore wind, and wave energy technologies are at different stages of development, these technologies could all benefit from incorporating reliability into component and system design. Component and system failure rates depend on wind and wave conditions, and have direct effects on capital costs, operational costs, and power production. During the array's pre-installation phase, required reliability levels–or the probability a component

or system operates as designed for its design life–impact the design of the components and system, which directly affect their costs. During operation, component and system failures affect downtime (during which power is being produced sub-optimally or not at all) and failure costs (including the cost of repair, labor, equipment, and transport). Improving reliability of these technologies will enable devices to endure energy-dense sea states, lengthen operational life, decrease costly operations and maintenance (O&M), and decrease financial risk premiums. Incorporating RBDO can enable increased market competitiveness, but has different challenges for each technology based on technological maturity.

1.1.1 Status of Offshore Renewable Energy Technologies

Fixed-foundation offshore wind energy technology has reached widespread commercial-scale installation in Europe, recent significant price decreases, and market development in emerging markets in the U.S. and China. Despite recently achieving subsidy-free bids in select markets, the cost of energy associated with these systems is still not cost competitive with other renewable energy technologies like solar photovoltaic systems (Figure 1.1) [58]. Furthermore, as fixed-foundation developers continue to stretch the dimensions of their designs to accommodate larger capacity turbines, installed further offshore in deeper waters where wind loading is higher and more consistent, the industry will have to adapt to step-wise design changes (for example, from gearbox to direct-drive systems) and increased failure costs (resulting from decreased accessibility and availability). While this industry

is currently growing rapidly, pervasive subsidy removal only emphasizes the need to increase reliability and power production in these systems while decreasing costs.

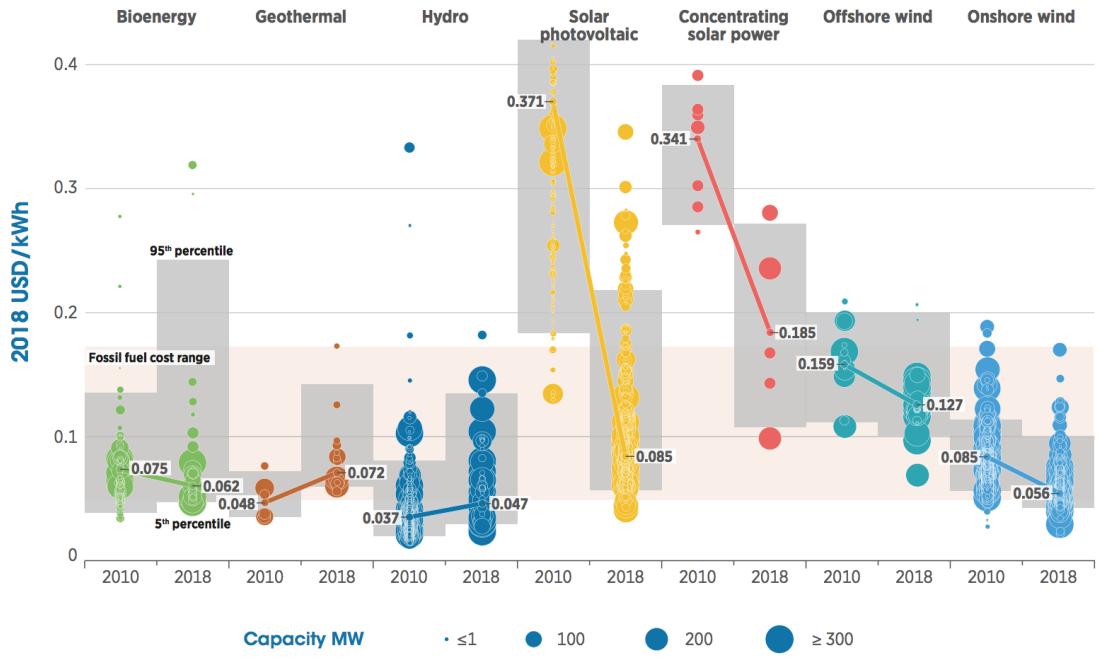

Figure 1.1: Global LCOE of utility-scale renewable power generation technologies, commissioned in 2010–2018: the diameter of the circle represents the size of the project, the center of the circle represents the cost of the project, and the thick lines are the global weighted-average LCOE [58]

Floating offshore wind technology promises to expand the offshore wind market into deeper waters where wind resource is higher and more consistent, but where fixed foundations are infeasible to install. While fixed-foundation offshore wind energy technology has nearly thirty years of operational experience and is a mature technology, floating offshore wind energy technology is still in demonstration stages of development. Although most developers leverage fixed-foundation offshore wind

turbine experience by using the three-bladed horizontal-axis wind turbine design, the novel technology in the floating industry—the floating platform design on which the turbine is mounted—has no emergent, dominant design and is still undergoing product innovation. Growth plans conveyed in the roadmaps are overly optimistic [11] and a complete set of design guidelines and standards are still being developed, but the first commercial demonstration of floating offshore wind turbines was grid-connected in late 2017 (by Equinor, then Statoil), with other platform technologies close behind (Principle Power, for instance, deployed a 25-MW demonstration array in mid-2018).

Wave energy technologies are less mature, with no commercial-scale installations. The wave energy sector is currently in a stage of product innovation, small-scale testing, and prototyping. Hundreds of patents exist for unique WEC designs, with no clearly dominant design emerging. Comprised of mostly novel technology, wave energy research and development has less previous work to leverage from other industries, few and developing design standards and guidelines, limited commercial testing experience, and only recent advances in the supporting technical and political frameworks for wave energy technologies.

1.1.2 Opportunity for Reliability-Based Design Optimization Application

Currently, in the fixed-foundation offshore wind market, loads and reliability are considered as static constraints during the design process (as depicted in Figure

1.2), driven by design standards and guidelines modified from offshore oil platform guidelines for shallow-water developments.

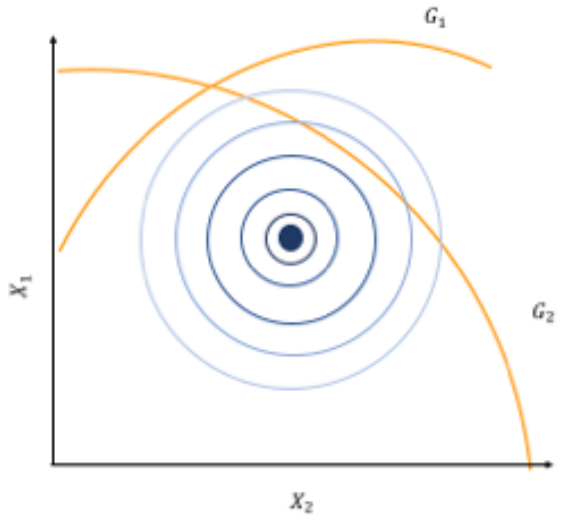

Figure 1.2: Traditionally, reliability is used as a constraint in optimization problems. For instance, optimize two parameters (X_1 and X_2) that define turbine blade shape to maximize power (F_{x_1}) and minimize cost (F_{x_2}), given a required reliability of 95% confidence that the blade lasts a mean of 20 years (which generate G_1 and G_2).

In contrast, many design guidelines and standards are still evolving for floating offshore wind and wave energy conversion technology. In early design concepts for WECs, reliability—if considered at all—is often considered secondary to power development and cost. At this state in development, many incentives and funding schemes emphasize testing a WEC which creates the most power at the least cost [118]. If reliability is considered in early design, it is often in an ad-hoc manner, such as gaining an estimate of hull structural reliability through the failure of a WEC hull midway through a testing campaign. Considering reliability as a

constraint for components has enabled the current status of these technologies, but achieving ambitious industry goals for reducing costs of energy will require intentional consideration of reliability as an objective to reduce O&M costs and failures, not just across components, but systems.

RBDO can be used in fixed-foundation offshore wind technology both to extend standard designs to new load cases, as well as to help avoid reliability issues in new component designs. Any reliability issues experienced by the fixed-foundation offshore wind energy industry up to this point will only multiply in cost as component size, wind loading, and distance from shore increase. It will be critical to elucidate foundational relationships between component reliability and systems optimization to address any outstanding reliability issues in the paradigm designs. In floating offshore wind energy systems, RBDO can be used to avoid costly failures in novel floating platform designs prior to installation, and also to help identify optimal solutions as the industry converges on installation-worthy designs. This is even more true for the WEC industry, given the extensive catalog of WEC designs patented. The WEC industry could benefit from intentionally incorporating RBDO in early design to help the industry identify more optimal designs which consider performance, cost, and reliability. More importantly, RBDO could help expose foundational relationships between reliability and WEC design that are not currently understood, such as the relationship between WEC hull shape and power take-off (PTO) reliability.

This work explores relationships between component reliability and systems optimization that span all three technologies (fixed-foundation offshore wind, floating

offshore wind, and wave energy technologies), and bridges critical components in each system. This approach will help establish RBDO methodologies to address each technology's needs given their varying levels of maturity. This approach will result in a better understanding of the component and system parameters that drive failure and associated costs in these complex systems, and how to leverage this understanding to improve reliability and reduce failure costs.

1.2 Research Objectives and Impact of Achieving Objectives

Through this body of research, I will answer the following motivating research question: how are critical component reliability and system optimization related in offshore renewable energy systems, and how can systems optimization methods be used to improve reliability in these critical components?

I theorize that system-level design can reduce component damage, failure, and costs through wind and wave load modification. The quantitative relationships between component, device, and system levels will be explored by focusing on the reliability of specific components, but will expose fundamental relationships and establish methods that can be applied to other similar components. The motivating research question above is decomposed into three specific research areas, which I will briefly describe in Sections 1.2.1, 1.2.2, 1.2.3.

1.2.1 Reliability-Based Layout Optimization of Offshore Wind Turbine Array Layouts

How does offshore wind turbine array layout and resulting wind-wake interactions affect critical component reliability, power production, and associated failure costs?

In this research focus, I construct an optimization algorithm to optimize offshore wind turbine array layout for maximizing power production and minimizing failure costs based on drivetrain planetary bearing failure in a gearbox design. This knowledge will be used to establish how array layout and component failure can impact each other, and their relative impact on cost of energy. This relationship and method can then be applied to other critical failure components with high probabilities of failure and associated failure costs, including emerging design innovations.

1.2.2 Reliability-Based Design Optimization of Wave Energy Converter Hull Geometry

How does WEC hull shape affect critical component reliability?

In this research focus, I optimize WEC hull shape for power take-off reliability and power production in a point-absorber type WEC. Power take-off (PTO) systems in WECs are mechanisms which translate the primary converter's absorbed

energy into useable electricity. I use structural fatigue analysis and power production modeling to draw general conclusions about how damage to the PTO rod weld connecting the PTO to the hull changes with WEC hull shape and PTO orientation across sea state conditions. Results from this investigation will inform the relative importance of these foundational system design parameters on critical component damage.

1.2.3 Mooring and Foundation Reliability in Co-Located Wind-Wave Systems

How does co-location affect foundation and mooring reliability and associated failure costs in offshore wind turbines?

In this research focus, I investigate the relative impact of including WECs windward of a wind turbine array on 1) fixed-foundation offshore wind turbine monopile structures, and 2) floating offshore wind turbine mooring chain. This includes quantifying the effects of WEC array size and layout on damage equivalent loads (DELs) experienced by fixed-foundation offshore wind turbine monopile foundations and floating offshore wind turbine mooring chains. The results of this study provide insight into the potential opportunity of co-located systems, about which there is little research.

1.3 Dissertation Roadmap

These three research foci will enable offshore renewable energy researchers and developers to make more informed design decisions in offshore wind and wave energy systems for improved reliability, power production, and cost. Chapter 2 highlights the relationship between offshore wind turbine array layout and drivetrain failure, enabling improved offshore wind turbine array layout design. Chapter 3 documents the relationship between WEC hull shape and PTO orientation to PTO reliability and power production. Understanding how these design parameters interact with design is critical to advancing and converging on optimal WEC designs. In Chapters 4 and 5, opportunities to advance both offshore wind and wave energy industries through co-location of devices in the same ocean space are explored. Specifically, Chapter 4 considers the impact of co-locating WECs windward of offshore wind turbines on the offshore wind turbine monopile foundations, and Chapter 5 considers the impact of that co-location on the mooring of floating offshore wind turbines. By understanding how wind (fixed and floating) and wave energy technologies interact from a reliability, power production, and cost perspective, offshore renewable energy developers can make more informed decisions about this potential development opportunity.

Chapter 2: Reliability-Based Layout Optimization in Offshore Wind Turbine Arrays

2.1 Introduction

Since the first industrial installation of offshore wind turbines in 1991, cumulative installed capacity of global offshore wind energy has reached over 17.5 GW [49, 127]. While established markets in the United Kingdom, Germany, and Denmark continue to lead in installed capacity, offshore wind is also growing in emerging markets in Asia and North America. This adoption and growth is firstly enabled by continued advances in turbine technology, learning-curve benefits, and economies of scale achieved via industry experience and maturation in Northern Europe, and secondly by political support (for instance, by state policies and renewable energy portfolio standards in the U.S., or China's national offshore wind targets and nationally-funded megaprojects [49, 37]). In the Northern European offshore wind market, levelized costs of energy have decreased by more than 50% over the past five years, and in some cases, projects have been initiated without explicit subsidies [113]. Turbines are being installed increasingly farther offshore, where the wind resource is faster and less turbulent, and visual impacts (a frequent barrier to development) are reduced.

These promising trends underline the importance of realizing cost reductions

and technical improvements in offshore wind; while costs are currently economically feasible, offshore wind energy remains more costly than traditional forms of electricity production, and is still more expensive than other renewable energy technologies [58]. The proposed cost decreases and subsidy-free bids seen in recent auctions are indicative of the strength of this growing market, and are made possible by the growing interest and confidence of energy buyers to enter into offshore wind energy Power Purchase Agreements, or financial agreements between developers and power purchasers to ensure rates at which the proposed project's electricity will be bought. In emerging markets where confidence of energy buyers is growing (like the U.S. and China), or in markets that put responsibility for additional costs, such as grid connection and site surveys, on developers (like in the U.K.), subsidies will be required for the foreseeable future if nothing is done to further reduce costs [4]. Increasing market shares and cost competitiveness in the renewable energy sector remains a major objective for the offshore wind energy industry.

One way to decrease costs for offshore wind development is through increased component and system reliability. The probabilities of failure for components and systems depend on wind and wave conditions and have direct effects on capital costs, operational costs, and power production. During pre-installation, required reliability levels–for example, through dictated design standards or by expected lifetime or scheduled maintenance estimates–impact the design of the components and system, which directly affect their capital costs. During operation, component and system probabilities of failure affect downtime (during which power is being

produced sub-optimally or not at all) and failure costs (including cost of repair, labor, equipment, and transport). O&M costs alone currently account for up to 30% of overall offshore wind array costs [83].

Time at sea performing O&M drives cost for offshore wind turbine operations, and is compounded by short weather windows for repairs, limited trained personnel and vessels, availability of spare parts, and profit loss from lack of production during downtime. Developing in areas further offshore in deeper waters allows for exploitation of the greater wind resource, but will potentially increase time at sea, increased costs, and decrease accessibility. First, consistently stronger and less turbulent winds expose turbines to higher wind and wave loads in both nominal and extreme conditions, which requires increased capital costs to design and build devices with sufficient reliability levels. Second, accessing equipment that requires repair or maintenance is more difficult in areas further offshore (which requires access using a helicopter or boat), given that wind speed and wave height are strongly correlated. Especially as turbines increase in capacity and size and are installed further offshore, decreasing the failure rate of components and systems could decrease downtime, lost revenue, and failure costs.

Predicting failure and associated costs is complicated by the lack of knowledge about the relationship between component reliability and system design. Nearly thirty years of industry experience has led to the identification of the most costly and common failure modes and components. Predicting required warranty renewal and part repair and replacement is identified as a common problem in this industry [73], but has become an acceptable uncertainty and is most commonly addressed

through expert judgment based on worker experience. This reliance on operational experience has led to unexpected issues with reliability and performance. In some cases, fixed-foundation offshore wind turbines are exhibiting widespread shorter operational life expectancy and lower estimates of lifetime power production than as they were designed [54, 72]. In other cases, developers have begun the practice of curtailing specific installed turbines to reduce their wake production and allow the array to produce more power overall [131, 41]. If the industry wishes to avoid unexpected issues with reliability and performance in the future, tools need to be developed to leverage both operational experience and systems failure prediction and design.

Despite the importance of considering, simulating, and predicting wind system reliability, the relationship between turbine array layout, component failures, and associated costs is not well understood. While models exist to calculate wind loads from wind condition inputs, models that sufficient capture dynamic or unsteady wind conditions are computationally expensive and thus not suitable for research applications requiring hundreds or thousands of evaluations, e.g., optimization. Furthermore, models that transfer these wind loads to the structural or mechanical components and estimate their reliability are component-specific, expensive to develop due to experimental testing requirements, and rarely used in wind systems optimization. Thus, there is an opportunity to develop computationally inexpensive means of estimating component reliability from varying, realistic wind conditions in offshore wind turbine arrays, and the impact on O&M costs and power production. Wake interactions are a cause for non-uniform failure rates

and performance variations [133], but the relationship between wake interactions and component failures has not been quantitatively described.

In this study, I create an optimization algorithm that accounts for wake interactions in fixed-foundation offshore wind turbine array layouts based on power production and costs associated with drivetrain failure, specifically planetary bearing fatigue failure. This layout optimization directly relates coordinates of wind turbines in an array, and the environmental conditions at those coordinates, to component and system reliability and performance. This approach provides insight to the component and system parameters that drive failure and associated costs in these complex systems, and how to leverage this understanding to improve reliability and reduce failure costs. The schematic for this research is described in Figure 2.1.

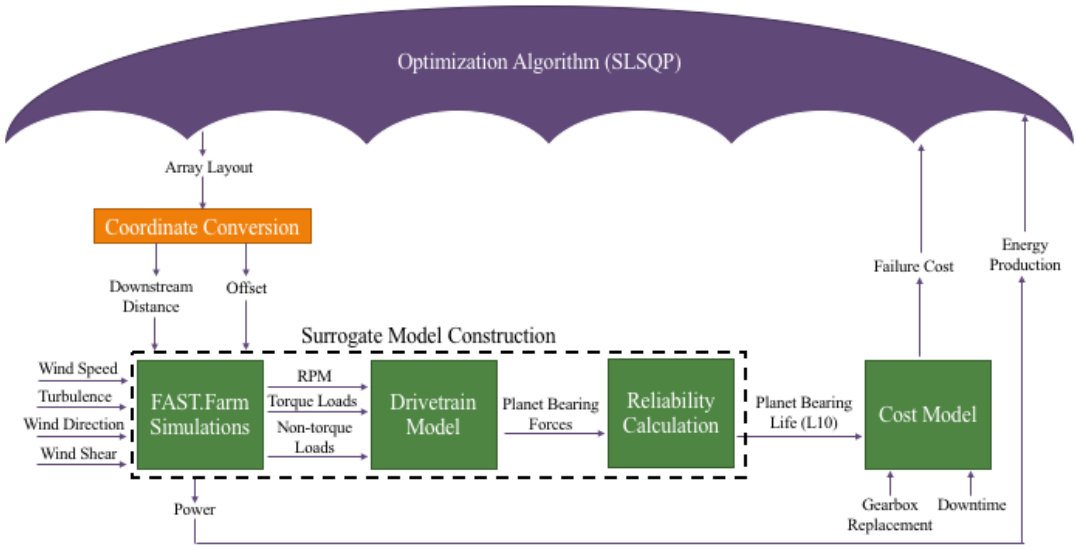

Figure 2.1: The main components and workflow of the RBLO computational framework; components used to develop the surrogate model are indicated by the dashed line

The following sections describe how I developed and implemented the models for this reliability-based layout optimization (RBLO) framework, highlighted in Figure 2.1, as well as findings from the development of the surrogate model and the optimization cases. Section 2.2 describes the specific turbine model and its gearbox configuration, highlighting the function, failure, and impact of planet bearings on O&M in offshore wind turbine arrays. The methods developed and used to explore the relationship between array layout and component reliability are then divided into two sections. Section 2.3 details the development of the surrogate model used to translate inflow wind conditions to planet bearing lifetime estimates (indicated in Figure 2.1 by the dashed line). Additionally, the physical relevance for the surrogate model and the underlying relationships between reliability and array

layout is discussed. Section 2.4 details the methods for RBLO. Then, the results of the optimization for various cases are discussed, relating the findings of the surrogate model to what is seen in the resulting optimized layouts. Finally, Section 2.5, highlights the main findings of this work and the potential impact on how the wind energy community understands reliability and its role in wind energy systems design and optimization, as well as opportunities for future work.

2.2 Background

Offshore wind turbines are getting larger, requiring the analysis of load response in wind turbine components as they are scaled to larger capacity systems. Figure 2.2 compares the annual average turbine capacity (blue bars) to the largest capacity prototypes available (multicolored shapes) the year they were built.

From Figure 2.2, it is seen that the average offshore wind turbine capacity surpassed 5MW for the first time in 2017, and is now just under 7MW. Further, with about three years to advance a prototype to serial production, the average wind turbine capacity is projected to increase [127]. What is more difficult to see in this graph is the shift in the design approach in industry. Until recently, the design approach has been to extend the nameplate power rating of an already existing turbine technology platform by incrementally upscaling structural components and increasing drivetrain and rotor capacities, while maintaining rotor size. In 2018, however, General Electric, Siemens Gamesa, and Senvion all announced significantly larger prototypes—10-12MW capacity (2-6MW larger than their previous

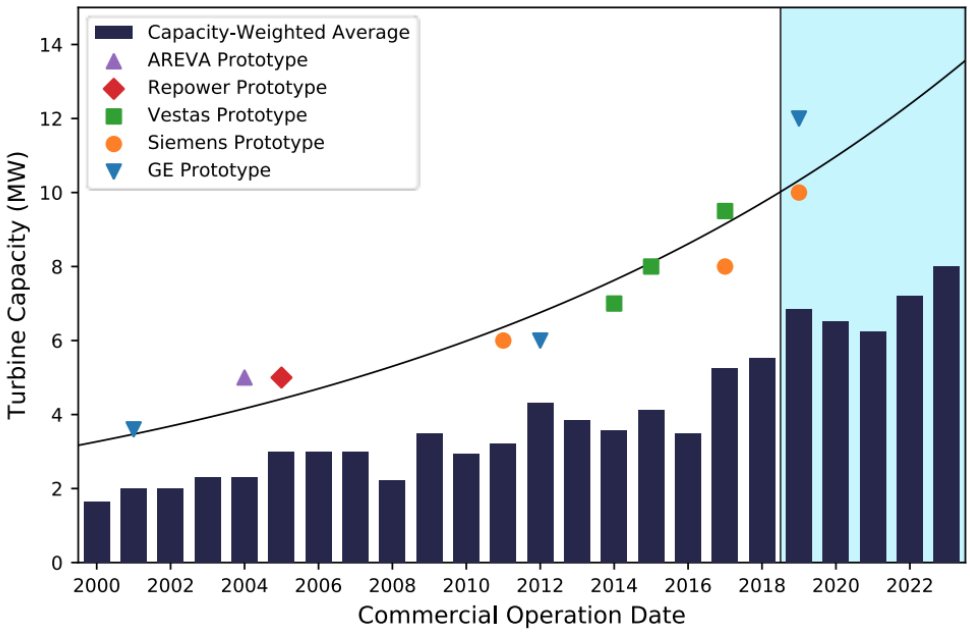

Figure 2.2: Average commercial offshore wind turbine rating compared to prototype deployment by year [127].

technology platforms)—with both increased rotor diameters (upscaling) and the adoption of direct drive systems over gearboxes (step-wise design changes).

Despite these market trends, turbine technology platforms in the 5-7MW range with gearboxes currently remain the dominant installed technology with the majority of market share. Additionally, this turbine size range has available reference models that include upscaled structural and mechanical components, whereas the next generation of reference turbines has yet to be fully described to the detail required for this RBLO work.

In this study, I use the 5MW National Renewable Energy Laboratory (NREL) reference wind turbine [63] and gearbox (Figure 2.6) [80] due to the current status of drivetrain technology and wind turbine size. In addition, I chose this turbine

because of the availability of gearbox models for critical failure components like planet bearings. The planet bearing model used in this study was developed as part of NREL's Gearbox Reliability Collaborative to investigate load sharing of planet bearings under non-torque loads [51]. Figure 2.3 shows the steady-state responses for the turbine as a function of wind speed [63]. For the wind conditions used to build this surrogate model, the turbine is operating in region 2.

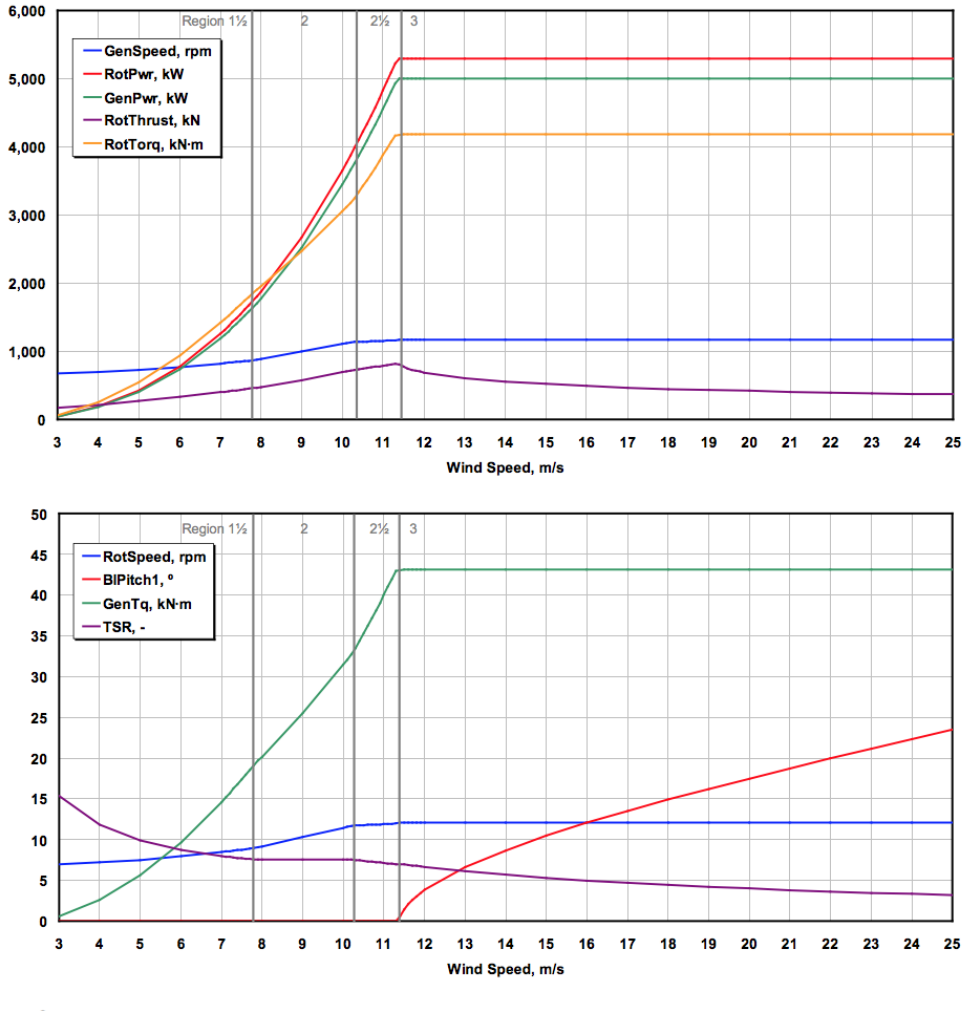

Figure 2.3: Steady state responses for the NREL 5MW reference wind turbine over wind speed; to note are the generated power (green line in the upper graph), rotor torque (yellow line in the upper graph) and rotor speed (green line in the lower graph) [63]

Figure 2.4 shows the main components of a wind turbine, with the gearbox highlighted. The drivetrain contains the generator and gearbox, which together convert the torque—or rotation of the blades—into electricity. Figure 2.5 provides

a detailed look at the gearbox design used in this study. The gearbox takes the relatively low rotation rate of the blades (5-15 rpm) to high speeds (1000-1800 rotations per minute) required to generate electricity with a high-speed induction generator. The number of high-speed moving parts makes this component susceptible to wear and failure [119].

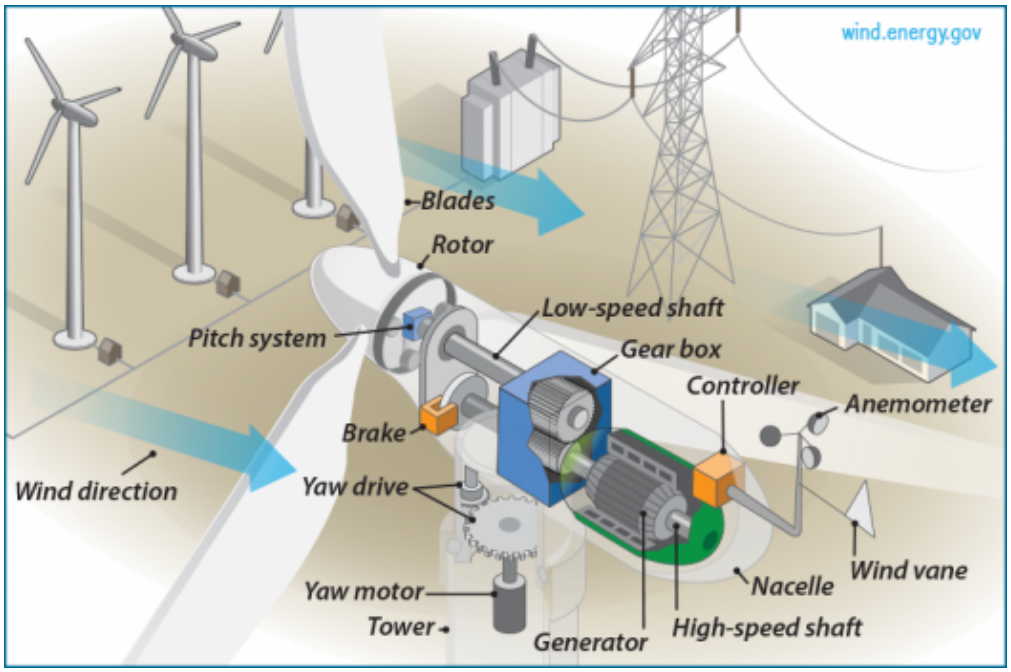

Figure 2.4: The main components of a wind turbine [35]

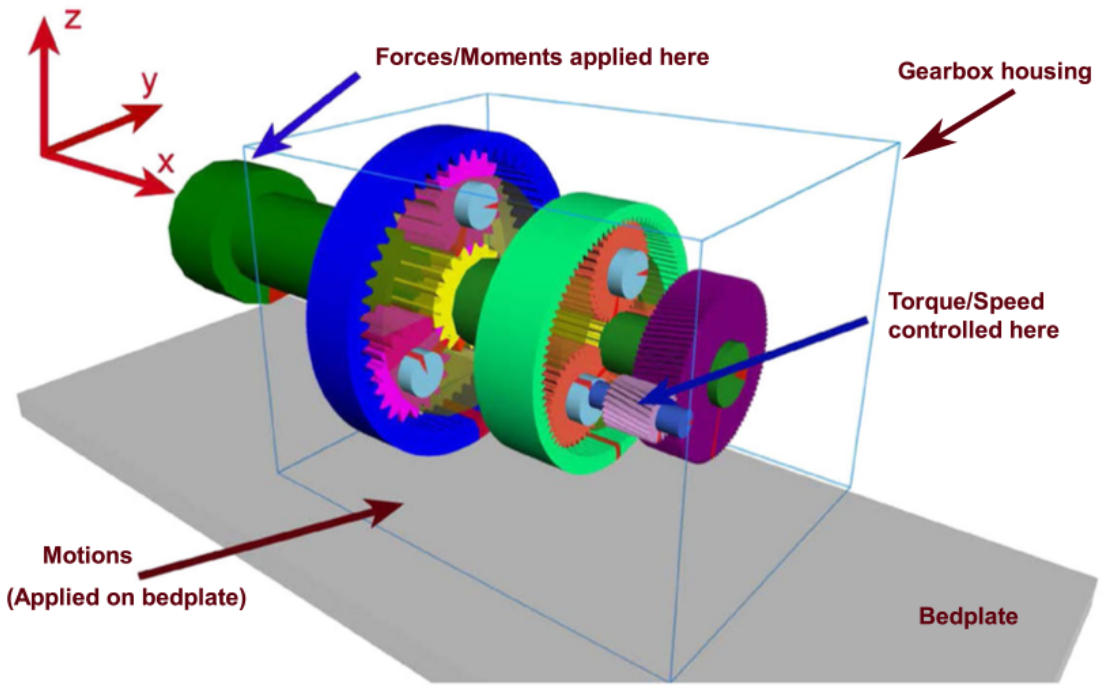

Figure 2.5: NREL 5MW Reference Offshore Wind Turbine Multibody System Model [80]

The 5MW reference high-speed gearbox used in this study has two planetary gear stages and one parallel stage (Figure 2.5 and 2.6), with three planet gears each. In the first and second stages of this reference gearbox, spur gears are used in the planetary configurations. The gears in the high-speed stage are parallel helical gears. The gear ratio per stage is optimized to minimize the total gearbox weight (Table 2.1).

This study focuses on planetary bearing fatigue failure due to the relatively high probability of gearbox failure and the severe consequence gearbox failure has on power production and O&M. Gearbox replacement has a moderately high rate of failure (Figure 2.7), causes one of the highest downtimes for repair among wind

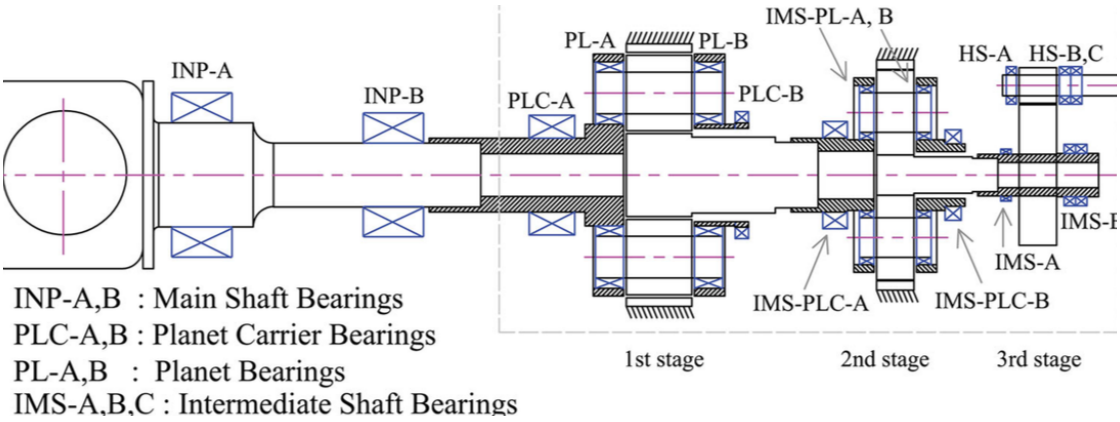

Figure 2.6: NREL 5MW reference offshore wind turbine schematic [80]

Table 2.1: 5MW reference wind turbine gearbox specifications

Parameter	**Value**
Type	Two planetary + one parallel
First stage ratio	1: 3.947
Second stage ratio	1: 6.167
Third stage ratio	1: 3.958
Total ratio	1: 96.354
Designed power (kW)	5000
Rated input shaft speed (rpm)	12.1
Rated generator shaft speed (rpm)	1165.9
Rated input shaft torque (kN-m)	3946
Rated generator shaft torque (kN-m)	40.953
Total dry mass (x1000 kg)	53
Service life (year)	20

turbine subsystems (Figure 2.8), and is expensive to repair [18, 66]. The material cost of gearbox replacement is the greatest subsystem repair cost (twice that of the second highest material cost of hub or blade repair) [18]. Gearbox repair requires the most technicians as well, second only to those required for blade repair [18].

Drivetrain planet bearings are a critical failure component within the gearbox

Table 2.2: 5MW reference wind turbine gearbox planet bearing specifications

Parameter	**Value**
Mass of carrier (kg)	5800
Center distance (m)	863E-3
Pressure angle (radians)	$20/180 * \pi$
Mass of shaft (kg)	18E3
Mass of planet bearing (kg)	1500
Number of planet bearings	3
Bedplate tilting angle (°)	[0.0,0.0,0.0]
Mounting angle (°)	18E3
Distance from hub to carrier center (m)	4.25
Length of shaft (m)	3.22
Distance between main shaft and planetary bearing system center (m)	5
Number of teeth in ring gear	56
Number of teeth in planet gear	17
Bearing capacity (N)	4730000
Exponent of life equation	10/3

and drivetrain system; if the planet bearings fail, they inhibit gearbox function and require a full gearbox replacement (estimated gearbox replacement was $\$628,000$ USD2011 [135]). Planet bearings have a relatively high failure rate, accounting for 76% of gearbox failures [51, 64, 81, 85] within the gearbox subsystem. Additionally, they are a source for premature failure (data show they only last a fraction of their designed life [43, 85]).

Of planet bearing failures, the most common are cracking, abrasion, adhesion, fretting corrosion, fatigue wear, and bending fatigue [106]. Fatigue wear Cracking occurs from heated conditions originating from excessive impact or loading. Abrasion occurs when the surface of a bearing comes into contact with another surface,

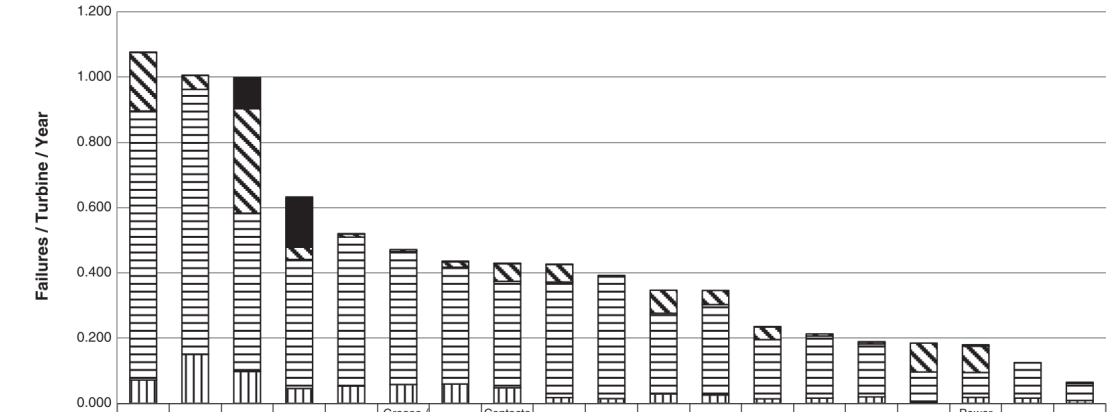

	Pitch / Hyd	Other Components	Generator	Gearbox	Blades	Grease / Oil / Cooling Liq.	Electrical Components	Contactor / Circuit Breaker / Relay	Controls	Safety	Sensors	Pumps/ Motors	Hub	Heaters / Coolers	Yaw System	Tower / Foundation	Power Supply / Converter	Service Items	Transformer
Major Replacement	0.001	0.001	0.095	0.154	0.001	0.000	0.002	0.002	0.001	0.000	0.000	0.000	0.001	0.000	0.001	0.000	0.005	0.000	0.001
Major Repair	0.179	0.042	0.321	0.038	0.010	0.006	0.016	0.054	0.054	0.004	0.070	0.043	0.038	0.007	0.006	0.089	0.081	0.001	0.003
Minor Repair	0.824	0.812	0.485	0.395	0.456	0.407	0.358	0.326	0.355	0.373	0.247	0.278	0.182	0.190	0.162	0.092	0.076	0.108	0.052
No Cost Data	0.072	0.150	0.098	0.046	0.053	0.058	0.059	0.048	0.018	0.015	0.029	0.025	0.014	0.016	0.020	0.004	0.018	0.016	0.009

Figure 2.7: Average failure rates for wind turbine (offshore and onshore) subassemblies and cost categories [18]

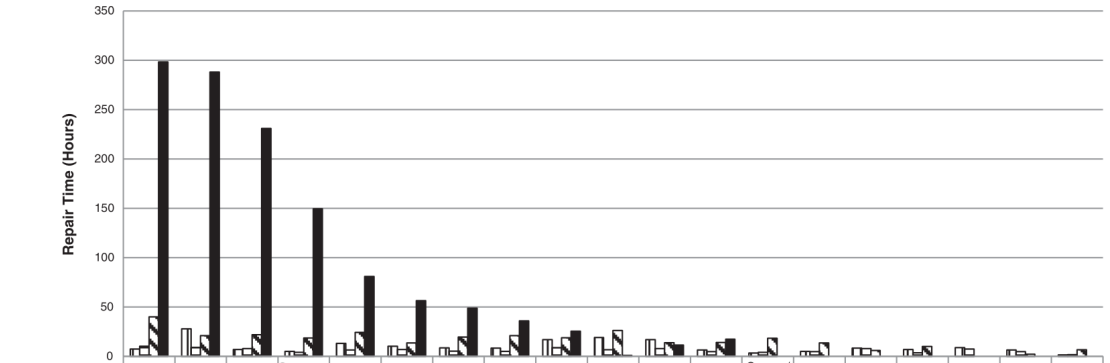

	Hub	Blades	Gearbox	Contactor / Circuit Breaker / Relay	Generator	Power Supply / Converter	Yaw System	Other Components	Pitch / Hyd	Transformer	Controls	Electrical Components	Grease / Oil / Cooling Liq.	Heaters / Coolers	Sensors	Pumps/Motors	Service Items	Tower / Foundation	Safety
No Cost Data	8	28	7	5	13	10	9	8	17	19	17	7	3	5	8	7	9	6	2
Minor Repair	10	9	8	4	7	7	5	5	9	7	8	5	4	5	8	4	7	5	2
Major Repair	40	21	22	19	24	14	20	21	19	26	14	14	18	14	6	10		2	7
Major Replacement	298	288	231	150	81	57	49	36	25	1	12	18	0	0	0	0	0	0	0

Figure 2.8: Average repair times for wind turbine (offshore and onshore) subassemblies and components [18]

made rough by the presence of debris or particles. Adhesion is caused by the bearing slipping, which causes it to lose material to that other contacted surface.

Deterioration of gear tooth surface is due to cyclic contact and small vibrations [106]. Fatigue wear and bending fatigue occur from the cyclic use of the bearing over time, with fatigue wear representing wear from equal loading between the bearings, and bending fatigue representing wear from unequal load distribution between the bearings.

Previous studies have shown that drivetrain loads are most affected by the shear exponent α, turbulence standard deviation in the primary wind propagation direction σ_u [50, 101]. Therefore, by focusing on relating wind conditions and array layout to main shaft damage equivalent loads, planet bearing forces, and planet bearing reliability, the relationship between array layout and failure costs for planet bearings in offshore wind turbines can be explored.

2.3 Surrogate Model Construction

Accurately predicting power performance and structural loads of wind turbines in an array requires the use of complex models that, depending on their fidelity, can be computationally expensive. This expense can limit optimization and space exploration. FAST.Farm is a mid-fidelity multiphysics engineering tool that was built to solve the aero-hydro-servo-elastic dynamics of each turbine in an array, with additional consideration for array-specific physics. Namely, these additional considerations include ambient wind in the atmospheric boundary layer across the array, a wind array super controller, and wake deficits, advection, deflection, meandering, and merging [62]. Although a powerful tool, FAST.Farm and TurbSim

(a model that provides inflow conditions for FAST.Farm simulations) [61] are too computationally demanding to be integrated into an optimization framework in which many evaluations are required. Consequently, providing a surrogate model of FAST.Farm would enable the use of optimization across a potentially large and complex solution space.

Two surrogate models are constructed in this study, one to predict L_{10} reliability of planet bearings based on torque and non-torque (bending) moments on the main shaft of the NREL 5MW reference wind turbine [63], and one to predict power produced by the turbine, both in offshore conditions. The first model specifically focuses on drivetrain damage equivalent loads (DELs) on the planet bearings, driven by torque and non-torque (bending) loads on the main shaft, which are heavily influenced by rotor plane inflow conditions.

By using FAST.Farm to train the surrogate model, users benefit from incorporating the dynamic response of the wind turbines without having to use or have familiarity with FAST.Farm. While the computational expense required to generate the FAST.Farm outputs is high for the generation of training data, it will significantly reduce additional computational expense by providing interpolated outputs that would otherwise have had to be generated via FAST.Farm in an optimization routine.

This section details how the surrogate models are constructed, starting from input wind conditions and two-turbine array configuration, and ending at L_{10} estimation output, as depicted in Figure 2.9. Section 2.3.1 describes the methods sampling, FAST.Farm simulation and load data acquisition at those sampled

points. In Section 2.3.2, methods to transfer these loads from the main shaft of the drivetrain to the planet bearings is described. Section 2.3.3 chronicles how the planet bearing forces calculated by the drivetrain model are used to calculate L_{10}, as well as how the surrogate model was trained using that L_{10} data.

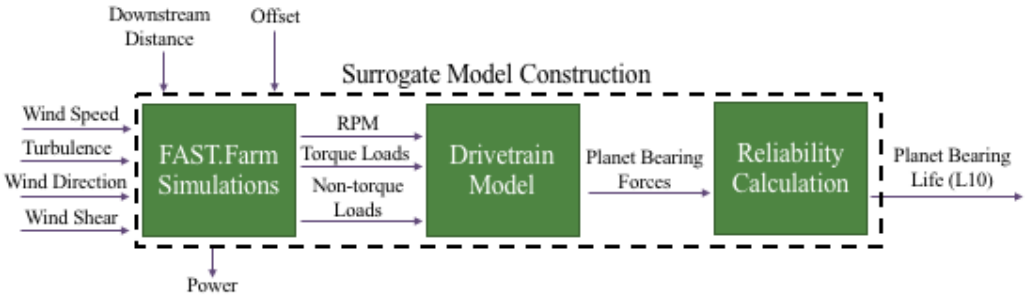

Figure 2.9: Schematic for surrogate model construction

2.3.1 Sampling and Load Data Acquisition via FAST.Farm Simulation

To provide enough data and to adequately describe the features of the solution space for surrogate method training, an appropriate sampling method must be determined. The sampling method used in this study is a full factorial method, or linear-spaced sampling across the design space. By sampling across the input parameters' domains, the results can provide insight about a solution space that is relatively unknown. Previous work has explored surrogate models for FAST that describe the relationship between turbulence, chord distribution, and twist distribution on damage equivalent moments on wind turbine blades [56], and blade loads [111]. In both studies, a full factorial sampling method was used, as in this

study.

In the creation of the surrogate model, each array is defined by two turbines and the relative downwind (x) and crosswind (y) distance between them. The data points were sampled uniformly in the downwind distance (5D, 6D, 7D, 8D, 9D, 10D where D is the rotor diameter and equal to 126 m) and nine data points in the offset direction (-2.0D, -1.5D, -1.0D, -0.5D, 0.0D, 0.5D, 1.0D, 1.5D, 2.0D). The locations of Turbine 2 (the downwind turbine) relative to Turbine 1 (the upwind turbine) are shown in Figure 2.10.

The framework to create the surrogate model is set up to sample parameters across wind speeds between 8 and 24 meters per second, and across IEC turbulence intensity classes (A, B, and C), although only results for a wind speed of 8 m/s and turbulence intensity class A are included in this thesis. For FAST.Farm simulations, I assume a single shear value of 0.3, a single wind direction, and that the turbines are always yawed into the oncoming wind direction. For each parameter combination (x, y), the simulation is repeated ten times (or with ten seeds). The number of FAST.Farm seeds was chosen based on previous work [2, 15, 92] to be an adequate number to understand the variability and uncertainty between FAST.Farm simulations. Each simulation runs for 2000 s using a 0.025 s time step.

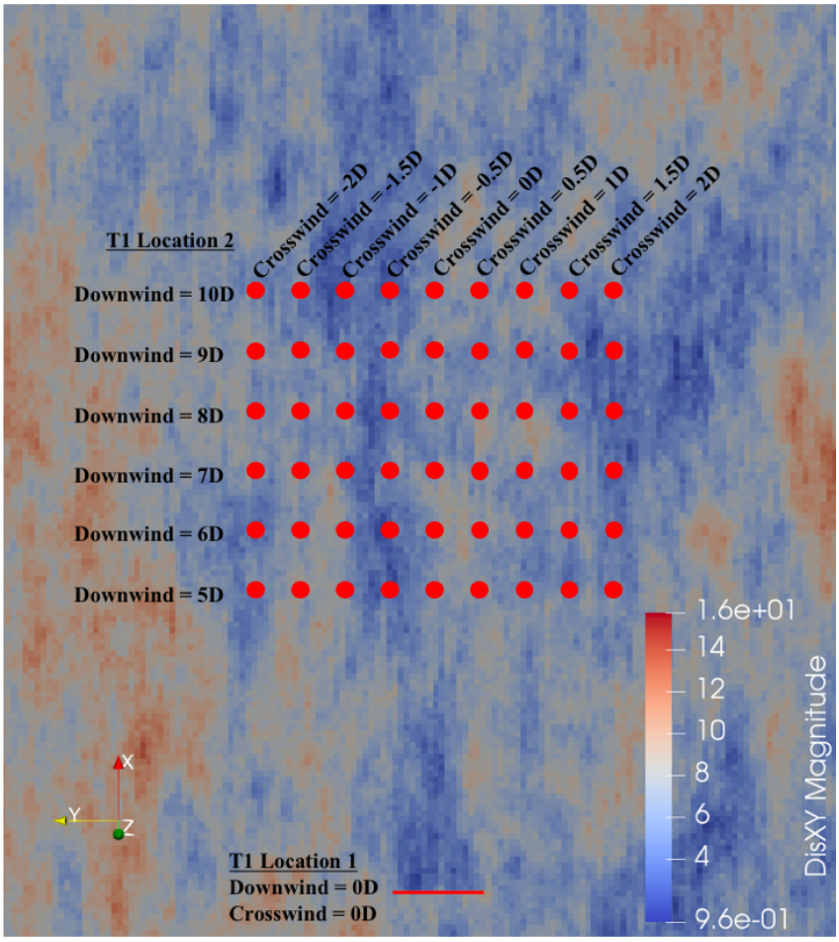

Figure 2.10: Here, the 54 locations for Turbine 2, on which the surrogate model is built, are depicted. Turbine 2 locations are relative to Turbine 1, located at (0, 0). The colormap represents the wind velocity.

Therefore, there are 54 data points to build the surrogate models. Each data point consists of ten concatenated FAST.Farm time series for each output channel. Output channels include generated power, rotor speed, and torque, bending moment in the y-axis, and bending moment in the z-axis on the main shaft. Figure 2.11 gives the orientation for the torque and non-torque moments on the main shaft.

The non-torque loads include pitching moments caused by the rotor weight and tower shadow, wind-induced moment, moment caused by the controller, thrust.

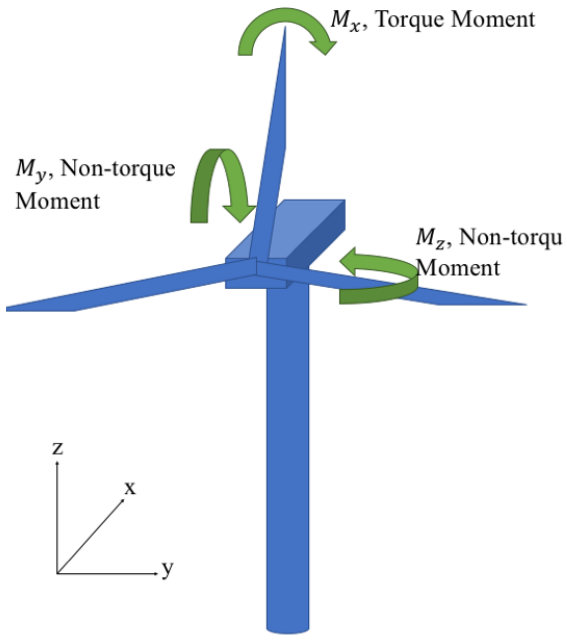

Figure 2.11: Orientation of turbine moment loads

The resulting mean loads and their standard deviations are depicted in Figures 2.12a through 2.12f. Figures 2.12a, 2.12c, and 2.12e depict the average mean load based on output FAST.Farm load time series for each of the 54, two-turbine array configurations, while figures 2.12b, 2.12d, and 2.12f depict their standard deviation. All load values are in Newton-meters (N-m) and the red line on the legend to the right of each figure represents the corresponding value of the upwind turbine.

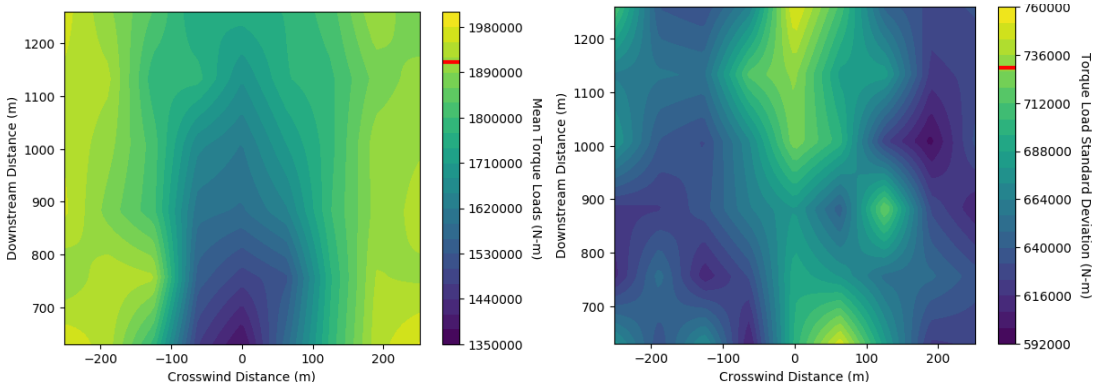

(a) Mean Torque Loads (N-m)

(b) Torque Load Standard Deviations (N-m)

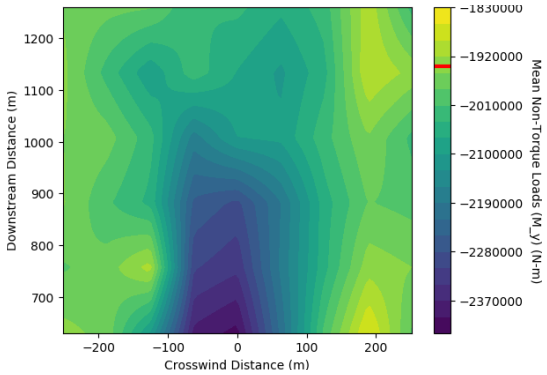

(c) Mean Non-Torque (M_y) Loads (N-m)

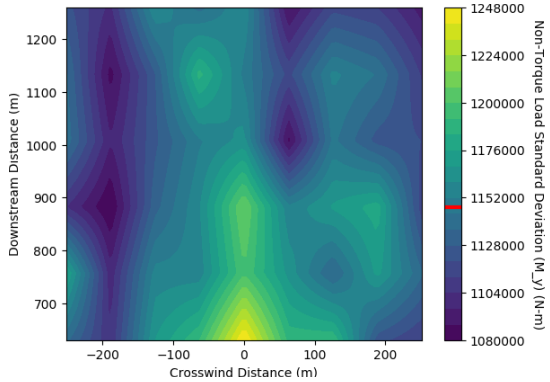

(d) M_y Standard Deviations (N-m)

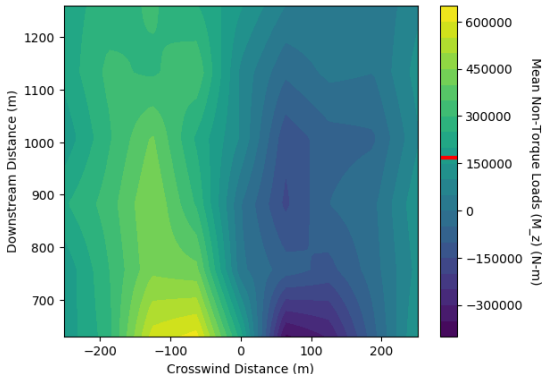

(e) Mean Non-Torque (M_z) Loads (N-m)

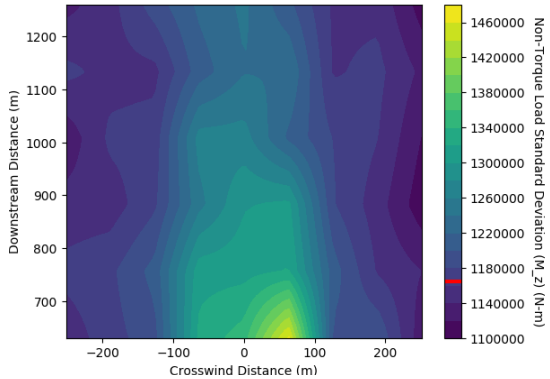

(f) M_z Standard Deviations (N-m)

Figure 2.12: Main shaft loads for varying two-turbine configurations

Worth noting about Figures 2.12a-2.12f is the symmetry of the loading across the crosswind distance of the downwind turbine, as well as the locations of extreme values. Mean torque loading and non-torque loading in the y-axis is symmetrical along x = 0, meaning that if the downwind turbine is directly behind the upwind turbine, moving it to the left or right will result in a similar increase in loading. There is a small offset in symmetry for non-torque loading in the y-axis, which is due to the gravitational forces experienced by the rotor as it spins, as well as the turbine spinning into the wake (if the turbine is left of the upwind turbine) or out of (if the turbine is right of the upwind turbine). Non-torque loading in the z-axis, however, is reflected across x = 0 and y = 0. This is due to the direction of rotation of the turbine. The turbine spins in a clockwise direction, so if the turbine is located to the right of the upwind turbine, it is experiencing less non-torque loading in the z-axis than if it is located to the left of the upwind turbine and is spinning into the wake.

The minimums and maximums follow this symmetry, with the minimum of both the mean torque loading and non-torque loading in the y-axis near a cross-wind distance of 0m, or when the downwind turbine is directly behind the upwind turbine, and when it is closest to the upwind turbine. Both of these load moments increase as downwind distance increases, and as the downwind turbine moves to the right or left of the upwind turbine. Meanwhile, non-torque load bending moment in the z-plane has a minimum just under 100m to the right of the upwind turbine, while the maximum is -100m (left) of the upwind turbine. These loads negligibly increase as the downwind turbine gets closer to the upwind turbine if the

turbine is to the left of the upwind turbine, and decrease if they are to the right of the upwind turbine. Lastly, the magnitude of these load moments differ between torque and non-torque load moments in the y-axis, which are comparable, while the non-torque load moments in the z-axis are three times smaller than the other load moments. This is expected, but reflects that one should expect a lower load contribution from the non-torque loads in the z-plane than from the other loads.

2.3.2 Drivetrain Modeling

After acquiring the load data, I used an analytical, experimentally-validated model developed through the Gearbox Reliability Collaborative at NREL [51] to transfer the main shaft loads (as in Figure 2.12 down the drivetrain and calculate the planetary loads on each of the three bearings. Figure 2.13 shows the main shaft load forces and moments (in this study, outputs from FAST.Farm).

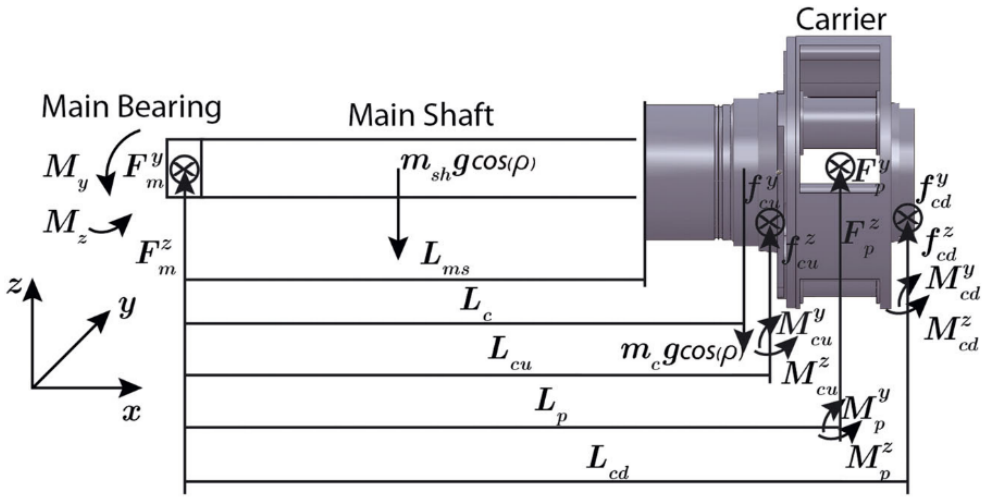

Figure 2.13: Force diagram of the main shaft and carrier [51]

From this force diagram, the torque (T_{in}) and non-torque loads (M_y and M_z) on the main shaft are formulated as:

$$T_{in} = \sum_{i=1}^{3} f_{t,i} d_c \tag{2.1}$$

$$M_y = \frac{1}{2} m_{sh} g L_{sh} \cos(\rho) + m_c g L_c \cos(\rho) - \left[\sum_{i=1}^{3} f_{t,i} \cos(\Omega_c t + \beta_i + e_i) - \sum_{i=1}^{3} m_p g \left[\sin(\Omega_c t + \beta_i + e_i) \right]^2 \cos(\rho) \right] L_p \tag{2.2}$$

$$M_z = \sum_{i=1}^{3} -m_p g \sin(\Omega_c t + \beta_i + e_i) \cos(\rho) - \left[\sum_{i=1}^{3} f_{t,i} \sin(\Omega_c t + \beta_i + e_i) + \sum_{i=1}^{3} m_p g \sin(\Omega_c t + \beta_i + e_i) \cos(\Omega_c t + \beta_i + e_i) \cos(\rho) \right] L_p \tag{2.3}$$

where $f_{t,i}$ and $f_{r,i}$ are the summation of the upwind and downwind row-bearing

forces in the tangential and radial directions, d_c is the center distance, m_{sh}, m_c, m_p are the masses of the main shaft, carrier, and planetary bearing, respectively, and g is the gravitational force. L_{sh}, L_c, and L_p denote the distance from the main bearing to the centers of gravity of the main shaft, carrier, and planetary gear, respectively. ρ is the bedplate tilting angle that supports the gearbox, Ω_c is the angle from the planetary gear center to the carrier center, which changes with t, time. β_i is the mounting angle, and e_i is the deviation angle from the designed circumferential position. Values used for these variables in the current study are provided in Table 2.2.

After solving for $f_{t,i}$ and $f_{r,i}$, the tooth loads on the i^{th} sun planet and ring planet meshes, $f_{sp,i}$ and $f_{rp,i}$ can be calculated via the equations:

$$f_{sp,i}\cos(\alpha) + f_{rp,i}\cos(\alpha) + m_p g\cos(\Omega_c t + \beta_i + e_i)\cos(\rho) + f_{t,i} = 0 \tag{2.4}$$

$$f_{sp,i}\sin(\alpha) + f_{rp,i}\sin(\alpha) + m_p g\sin(\Omega_c t + \beta_i + e_i)\cos(\rho) + f_{r,i} = 0 \tag{2.5}$$

$$f_{sp,i} r_b - f_{rp,i} r_b + I_p \ddot{\vartheta} = 0 \tag{2.6}$$

where α is the pressure angle, r_b is the base radius, I_p is the moment of inertia of the planet bearing, and $\ddot{\vartheta}$ is the rotational acceleration. Orientation of the variables in Equations 2.3 and 2.6 are depicted in the force diagrams for the carrier (Figure 2.14) and a single planet bearing (2.15.

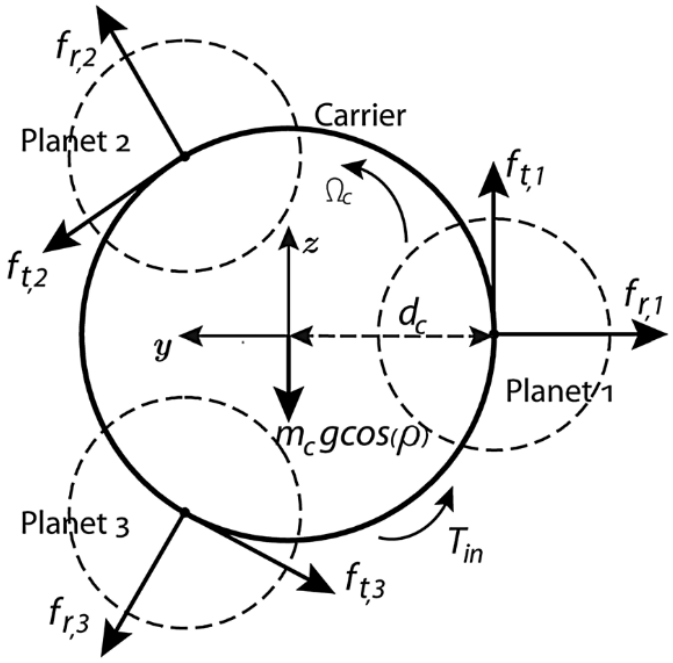

Figure 2.14: Force diagram of the planet bearing carrier [51]

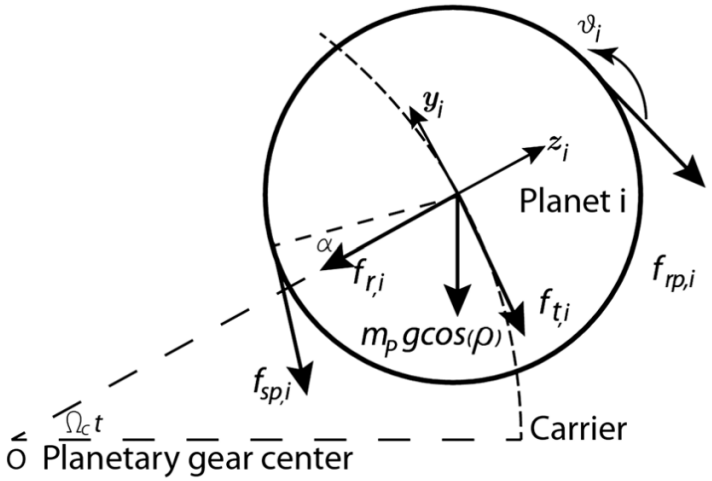

Figure 2.15: Force diagram of the planet gear [51]

2.3.3 Bearing Life (L_{10}) Calculation

From these calculated planet bearing forces, the L_{10} can be calculated. L_{10} represents the number of hours, or life, of a bearing with 90% reliability, in accordance with the ISO 281 standard [107]. Because L_{10} is a single value to estimate bearing life, the forces on the three planet bearings must be summarized into a single planet bearing system force. To aggregate the three bearings' force time series, the maximum planet bearing force is calculated at each time step in this study. By selecting the maximum force at each time step, a metric to estimate the reliability of the planet bearing system is estimated, rather than of each bearing. Further, the maximum force gives a more conservative estimate and includes the forces that drive the bearing degradation over time, whereas the mean force at each time step would result in an overestimate of bearing reliability.

An example planetary load time series for three bearings in a turbine for a single revolution is depicted in Figure 2.16.

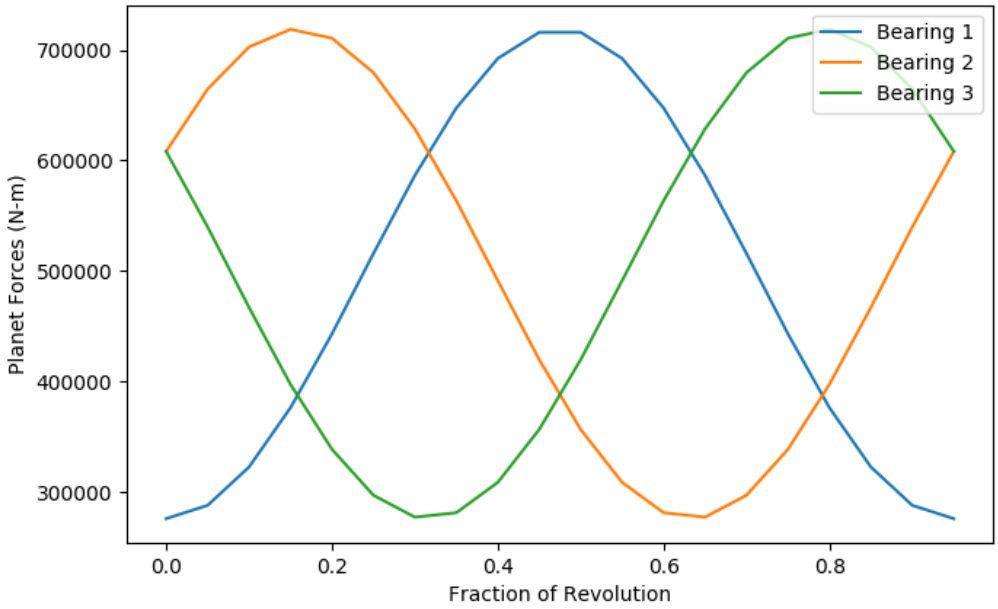

Figure 2.16: Planet bearing force time series of three bearings over a single revolution

One can see that the three bearing force time series for a single revolution is a translated sine wave. This is to be expected, and in an ideal model in which the planet bearings and carrier are unworn and equally share load, these time series will be exactly equal.

An example of this aggregated force time series for the case in which the downwind turbine is 8D directly behind the first turbine is shown in Figure 2.17. One can see that for each time step along the x-axis of a time series like in Figure 2.16, a single maximum force value is obtained and plotted in a time series like that in Figure 2.17.

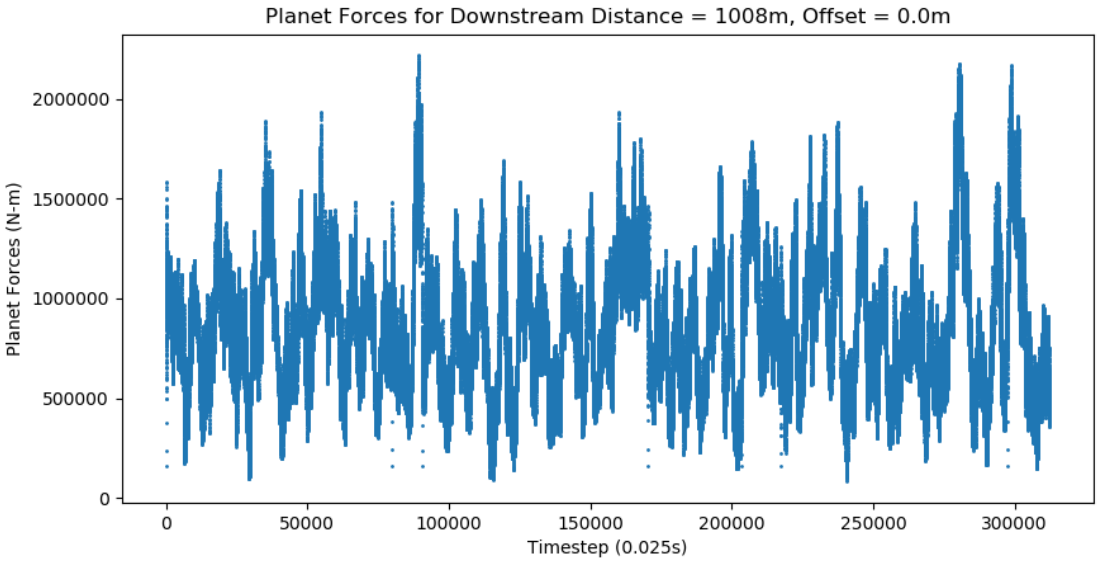

Figure 2.17: Maximum combined load time series (torque and non-torque bending moments) of the three planet bearings

Along with the force on the bearings, planet bearing speed is required to calculate the L_{10} reliability metric. An example time series of the planet bearing speed in the downwind turbine at a downwind distance of 5D and offset of 0D is depicted in Figure 2.18. The planet bearing speed is the same for all three bearings, so the time series in Figure 2.18 is representative of all three.

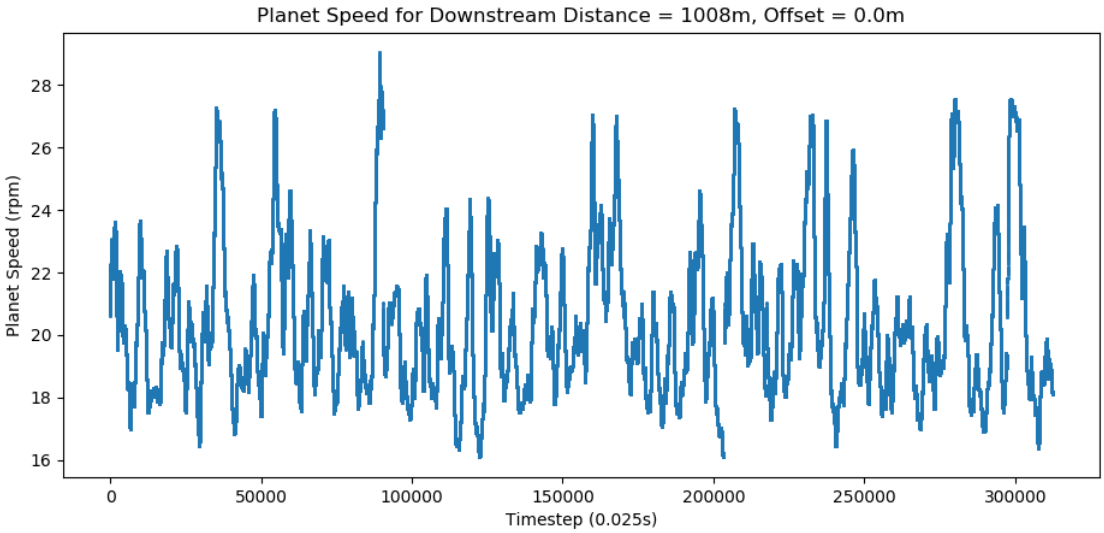

Figure 2.18: Time series of the planet bearing speed due to the rotation of the turbine

Following the time series generation for the planet bearing forces, each time series for a given downwind and crosswind distance is summarized into a Load Duration Distribution (LDD) and Load Revolution Distribution (LRD). Creating these distributions then allows for the calculation of the equivalent load and equivalent speed for the L_{10} calculation. An example of an LDD and LRD are given in Figures 2.19 and 2.20, respectively.

The LDD and LRD were created using automated bin assignment via Python's NumPy [105], and used to calculate the equivalent dynamic bearing load and equivalent speed via Equations 2.3.3 and 2.7. In Equations 2.3.3 and 2.7, each load bin is weighted by its contribution (in terms of time) and summed for the equivalent dynamic bearing load. A similar process is repeated for equivalent speed.

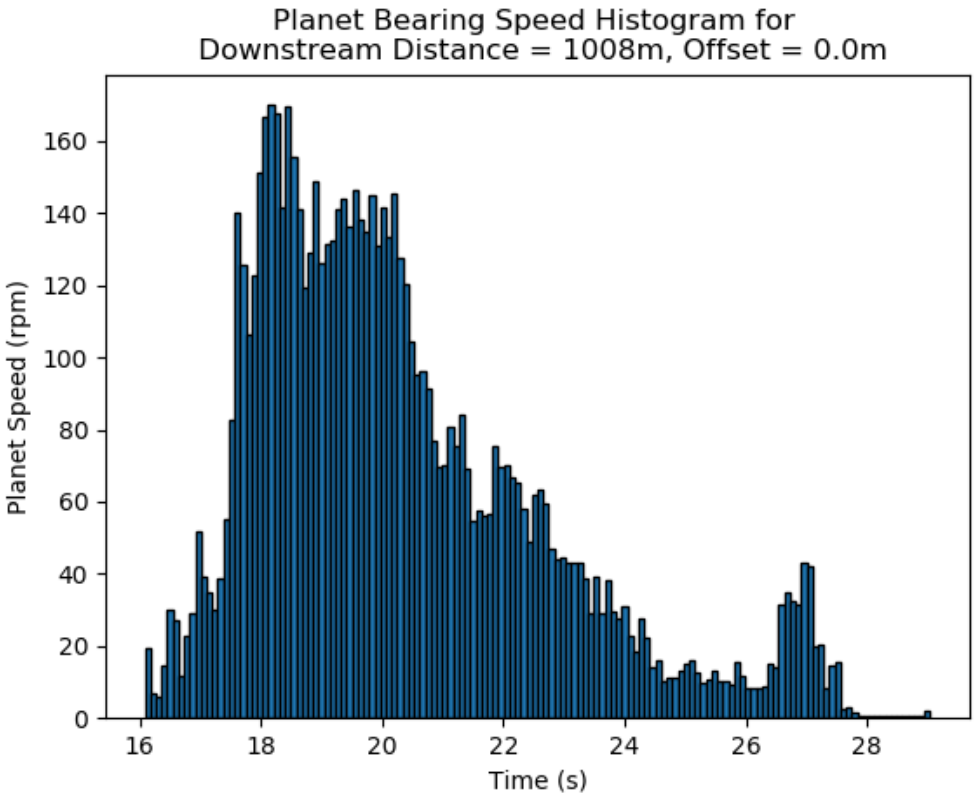

Figure 2.19: Histogram representing the maximum planet bearing speed time series

To calculate the mean equivalent speed, each LRD bin (representing the number of revolutions in rpm) is divided by the time spent by the bearings at that speed, and then multiplied by the relative contribution (in time) of that load range (Equation 2.3.3).

$$n_{eq} = \frac{\sum_i LRD_i LDD_i}{\sum_i LDD_i} * 60$$

where $LRD[i]$ is the mean speed for each bin, i, in rotations per minute (rpm) per

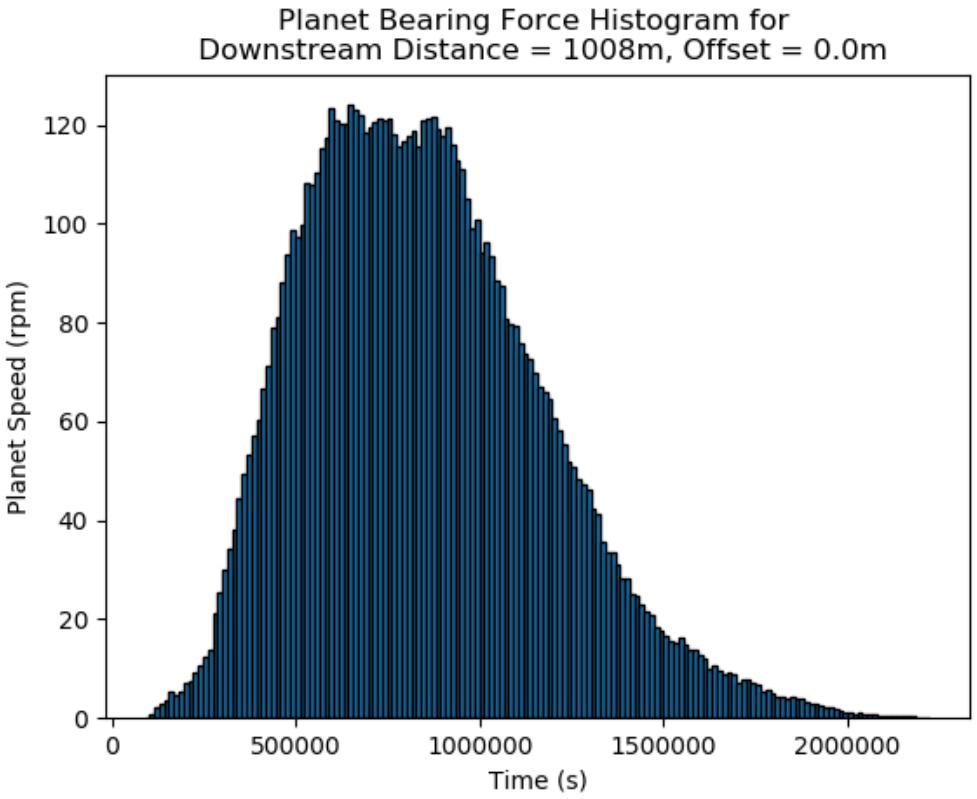

Figure 2.20: Histogram representing the maximum planet bearing force time series

second. $LDD[i]$ is the time (in seconds) spent at that speed for bin i. $\sum LDD[i]$ is the total simulation time (in seconds), and is used to determine the relative contribution of bin i. The equation is multiplied by 60 to create consistent units.

The mean equivalent dynamic load considers each discrete loading phase and the percentage of total travel that each load is applied during the cycle, as described in Equation 2.7:

$$F_m = \left(\frac{\sum_j |F_j|^e L_j}{\sum_j L_j} \right)^{1/e} \tag{2.7}$$

where L_j is the distance travelled during each phase, F_j is the load during each phase, and e is equal to $\frac{10}{3}$ for roller bearings.

Once the equivalent speed and load are determined, they are used to calculate the L_{10} reliability metric, as described in Equation 2.8:

$$L_{10} = \frac{10^6}{60 n_{eq}} \left(\frac{C}{F_m} \right)^e \tag{2.8}$$

where L_{10} represents the number of estimated hours until 10% of bearings fail. There is a 10% probability that at the applied load and speed, 10% of a population of identical bearings would suffer a fatigue failure, typically pitting on the raceway of the bearing. Note that this does not address other common failures caused by other conditions such as contamination, wear, misalignment, and improper lubrication [117]. n is the shaft speed (rpm), which is calculated as the equivalent speed. C is the basic dynamic load rating (N), which represents the constant stationary radial load which a roller bearing can theoretically endure for one million revolutions, reported by the bearing manufacturer for an appropriately sized bearing (the bearing size was determined by the definition of the 5MW Reference wind turbine [80] and is equal to 4730000 N in this study [107]). F_m is the equivalent dynamic bearing load (N), and e exponent of the life equation, and equal to $\frac{10}{3}$ for roller bearings [107].

After the L_{10} is calculated at each of the training data points, the surrogate model can finally be made. For this study, the Radial Basis Function was used for the surrogate model. Radial Basis Functions interpolate a surface using n-

dimensional scattered data within a given data range, are symmetric about a center point. Therefore, the Radial Basis Function interpolant used is a set of basis functions that are centered around each of the data sites, and is dependent upon only the radial distance. A multiquadratic basis function is used to smooth the basis functions and create continuity.

2.3.4 Surrogate Model Results and Discussion

Figure 2.21 shows the interpolated surface for L_{10} values over varying downwind and offset distances in a single wind condition in which wind speed is 8 m/s and turbulence intensity is IEA Class A, equal to 16%.

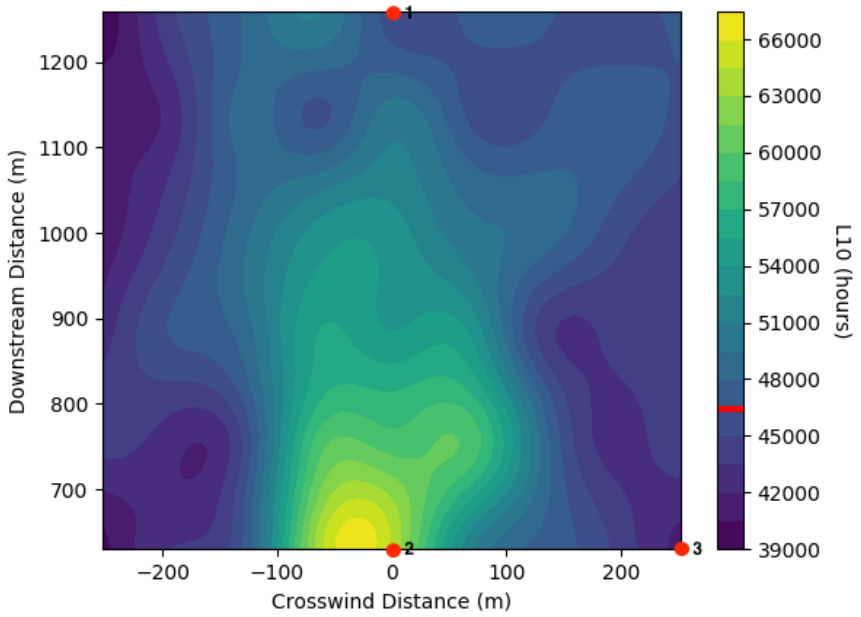

(a) The L_{10} surrogate model contour surface. The legend's red line represents the upwind turbine L_{10}, and the red dots represent three locations to be further analyzed.

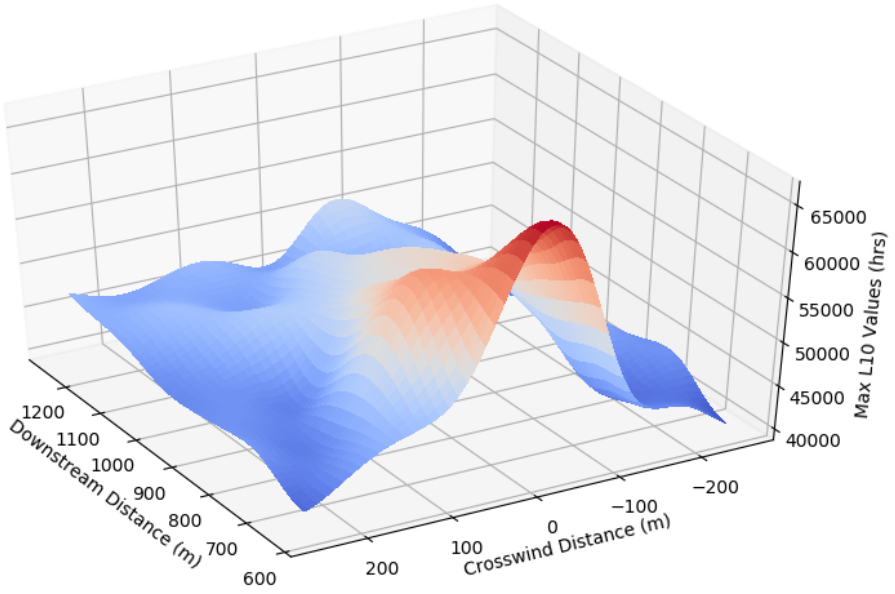

(b) 3D surface of the L_{10} surrogate model

Figure 2.21: The L_{10} surrogate model for planet bearings in the NREL 5MW Reference Turbine in offshore wind conditions U_w = 8m/s and TI = IEA Class A (16%)

Traditionally in wind system layout optimization research, algorithms place turbines to avoid wakes such that they produce more power at less cost. Reliability has an inverse relationship with wakes in components and systems driven by torque loads, as indicated also in Figure 2.21 for the planet bearings. Torque, dependent on wind speed, is less in the lee of turbines. Therefore, the power and reliability objectives are conflicting when optimizing wind array layout.

The impact of these results is significant. The difference in the minimum and maximum reliability values is 27000 hours, or 3 years. While the non-waked turbine has an average L_{10} value of 5.3 years, the optimal layout L_{10} value is over two years higher, 7.5 years. Therefore, this surrogate model suggests that the most optimal layout for reliability between two turbines is to place the downwind turbine directly behind the upwind turbine, 5D downwind. Exploiting this relationship, therefore, could result in up to two to three years gained before 10% of planet bearings fail. To verify these findings, the following sections will further explore how this surrogate model was created, and compare the global maximum to two other points in the L_{10} surrogate model. In particular, there are two interesting characteristics of this interpolated surface that will be discussed: first, its asymmetry, and second, the locations of extrema.

2.3.4.1 Asymmetry

Observing the interpolated surface, one would expect to see symmetry in the cross-wind distance, across $x = 0D$. That is, one would expect the reliability to reflect

the symmetry in the wake produced by an upwind turbine, so that the reliability would change similarly as the downwind turbine is moved crosswind in either direction. Instead, the surrogate model is mostly symmetrical, but around a crosswind distance of about x = -0.25D. There are a couple reasons that could explain this.

First, a certain amount of wake deflection from the rotation of the turbine is expected. In the FAST.Farm simulations, when the wake deflects, it moves off $x = 0D$, so that the area of low wind speed and high turbulence is located near $x = -0.25D$. The lower the wind speed, the fewer revolutions (and fatigue cycles) the planet bearings will experience, increasing bearing life.

Second, because of the direction of rotation of the turbine, partially waked turbines will experience different loading conditions depending on which side of the wake they are. This is due to the wind turbine spinning clockwise into the wake on the left side (negative crosswind distances), and out of the wake on the right (positive crosswind distances). Stanley and Ning [111] describe the effect of partial waking on wind turbine root blade loads for two-bladed turbines (Figure 2.22); as the turbine spins, gravitational and aerodynamic forces accentuate or dampen cyclic loading depending on the partially waked conditions.

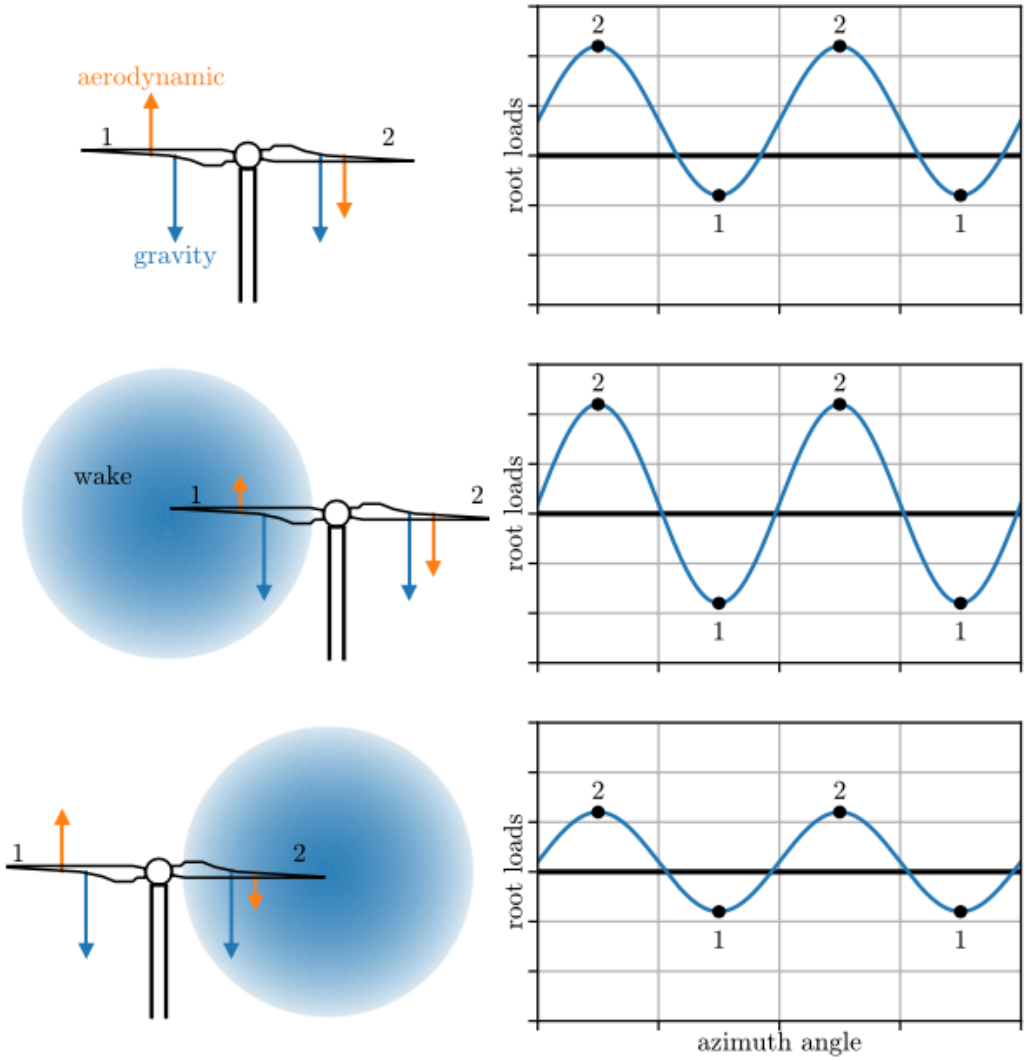

Figure 2.22: The top figure shows loads experienced in a non-waked scenario, the middle figure shows loads increased due to partial waking, and the bottom figure shows loads decreased due to partial waking [111]

In a non-waked condition, such as is the case in an upwind turbine, the forces cause a positive translation of the loading, so that the blade root experiences

greater loading when it is falling than when it is rising. When the turbine is partially waked so that the wake most affects the rising blade, the rising blade root loads increase in magnitude. When the turbine is partially waked so that the wake most affects the falling blade, the falling blade root loads decrease in magnitude. It has been suggested that this amplifying or dampening effect of the spinning blades could be another reason for the assymetrical L_{10} values, however, the results show this phenomenon is characteristic for blade root loads, but not for main shaft loads.

To see if partial waking could influence drivetrain loads, I compared main shaft load time series in four waking conditions: non-waked, partially waked on the falling blade, fully waked, and partially waked on the rising blade. Because Figure 2.22 is based on two-bladed turbine simulations in which turbulence is not included, its oscillations are consistent. The time series of the four partially waked conditions for this study's thee-bladed turbine FAST.Farm simulations does include turbulence, however, which adds variability to the load oscillations due to the turbine rotating (see Figure 2.23). Therefore,Figure 2.24 shows the statistical summary of those time series.

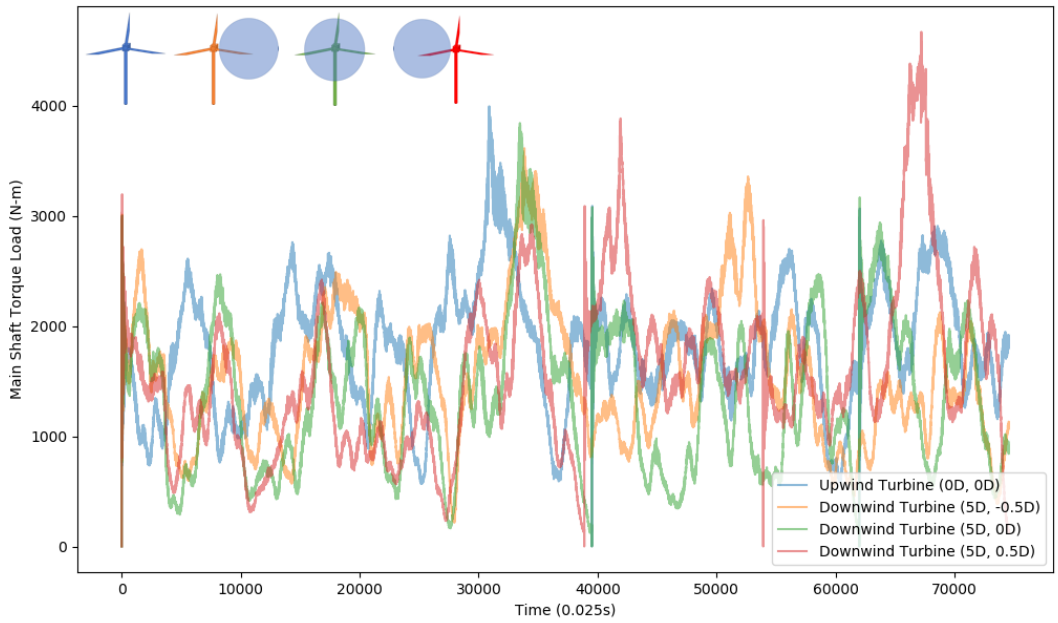

Figure 2.23: Time series of torque loads for four partially waked conditions: 1) an upwind turbine (blue), 2) a turbine partially waked on its falling blade (orange), 3) a fully waked turbine (green), and 4) a turbine partially waked on its rising blade (red)

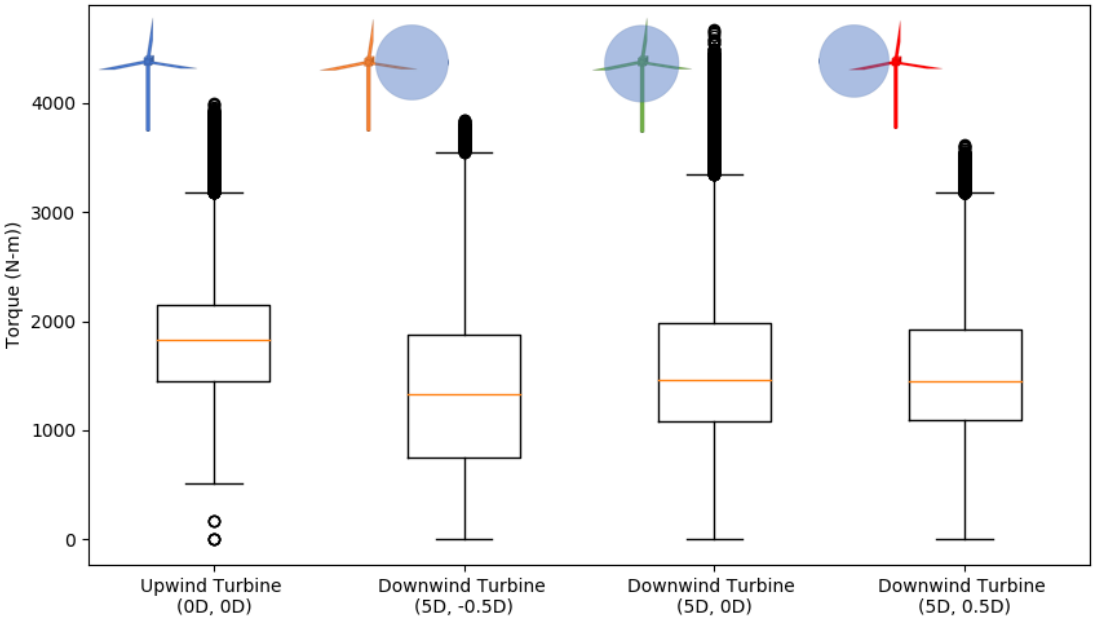

Figure 2.24: Statistical summary of torque loads for four partially waked conditions: 1) an upwind turbine (blue), 2) a turbine partially waked on its falling blade (orange), 3) a fully waked turbine (green), and 4) a turbine partially waked on its rising blade (red)

Figure 2.24 shows that the effect of partial waking on main shaft torque loads differs than that on blade root loads. The fully waked downwind turbine and the turbine that is waked on its rising blade side have about the same median main shaft torque load, and the turbine partially waked on its falling blade side has the lowest median main shaft torque load. In the time series plot, the turbulence creates variability, which is reflected here in Figure 2.24, but I can see these same trends reflected in Figure 2.12. In Figure 2.12, the torque loads are fairly symmetrical along the line x = 0, with the lowest loading on the main shaft near x = 0, and increasing with crosswind distance in the positive or negative direction. The

non-torque bending moment in the y-plane is less symmetrical, with lower loads centered around a slightly negative crosswind distance, and higher loads in the positive crosswind distance. Finally, non-torque loads in the z-plane show asymmetry, with maximum loads centered around the line x = -100, and minimum loads centered around the line x = 100. While torque is the main contributor to the forces experienced by the planet bearings after the torque and non-torque loads have been transferred down the main shaft, it is thought that the asymmetry of the torque and non-torque loads collectively contribute to the asymmetry of the L_{10} surrogate model.

2.3.4.2 Optima

This discussion of asymmetry not only in the L_{10} surrogate model, but also in the main shaft loading outputs in FAST.Farm leads to the next feature requiring further discussion: the location of local and global optima. Within the boundaries of the simulations (from -2D to 2D crosswind and 5D to 10D downwind), there is a global maximum reliability close to -0.25D crosswind and 5D downwind, with decreasing reliability as the downwind turbine moves further downwind and crosswind from that minimum. The gradient in the crosswind direction is more steep than that in the downwind direction, so that higher reliability values are maintained for longer in the downwind direction, and lower reliability values occur at x = -2D and 2D.

The two inputs to the L_{10} calculation are equivalent speed and equivalent load.

While the equivalent speed is a constant value and therefore does not contribute to optima in the L_{10} surface, Figure 2.25 shows an interpolated surface for equivalent loads.

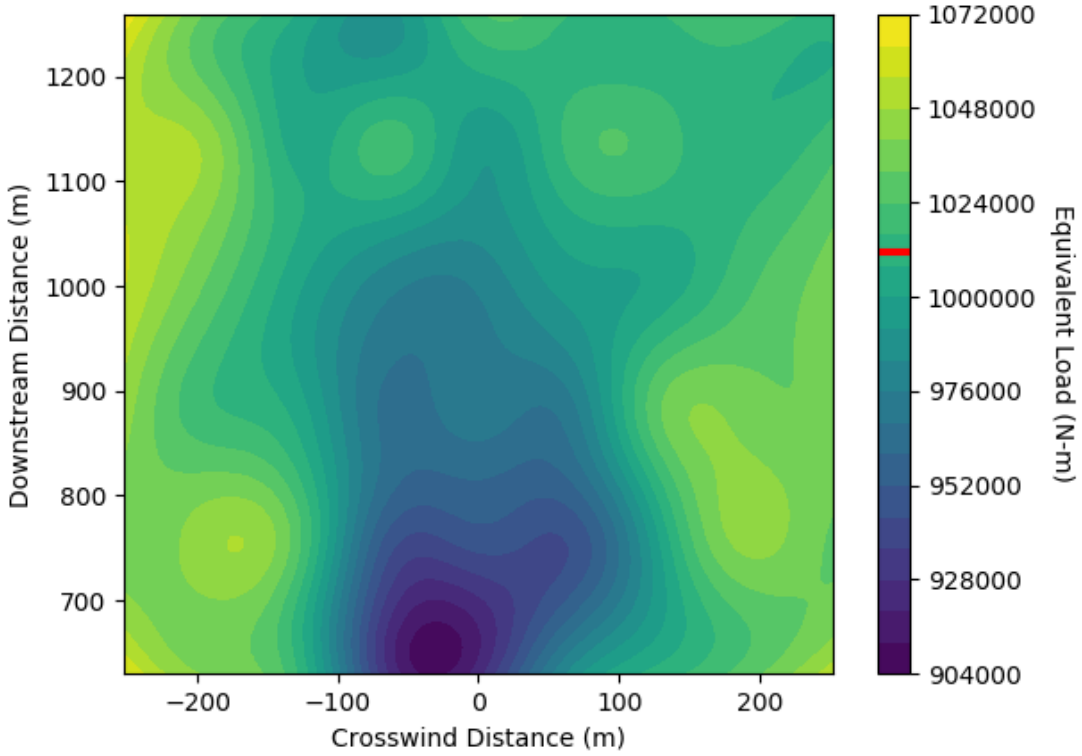

Figure 2.25: An interpolated surface of equivalent loads used to build the L_{10} surrogate model: the red line indicates the equivalent load of a non-waked turbine, and the red dots represent three locations to be further analyzed

Optima of the equivalent load surface reflect similar patterns as the L_{10} surface. Minima of the surface indicate lower equivalent loads as offset and downwind distance decrease. There is symmetry along the line x = -0.25D, which causes loads to affect partially waked turbines in negative crosswind distances more than those partially waked in positive crosswind distances. The standard deviation for

these 54 data points is 33,271 N-m, about a third of the mean value (=1,010,993 N-m), indicating a significant amount of variation. Figures 2.12b, 2.12d, and 2.12f also reflect a significant amount of variation, particularly in close to fully waked regions.

Since the equivalent load surface and main shaft loading supports the characteristics I see in the L_{10} surrogate model, two questions need further investigation: do the patterns in the L_{10} calculation originate 1) in the translation of main shaft loads to the equivalent loads, or 2) in the turbulence and wind speed, which dictate the loading on the main shaft?

To explore these questions, three locations near optima are further analyzed. These locations are indicated by the red dots in Figures 2.25 and 2.21. The locations represent the nearest datapoint to the global minimum, at (0D, 5D), and two points farthest away from the global minimum in the downwind (0D, 10D) and crosswind (2D, 5D) directions. These locations are depicted again in Figure 2.26 with a wake from the upwind turbine, as well as the approximate bladespan of the turbines.

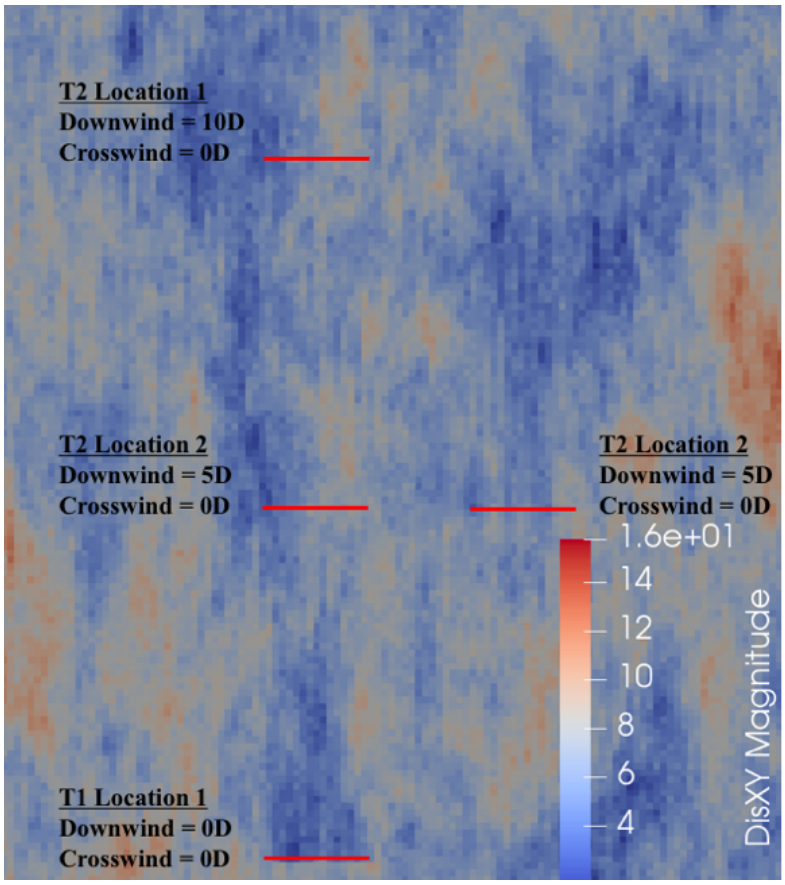

Figure 2.26: Locations of three turbines for further analysis and the wake of the upwind turbine generated via FAST.Farm (inflow is from the bottom of the figure)

The calculation of planetary forces relies on inputs from the FAST.Farm loads on the main shaft, and provide output for the equivalent load calculation. The equivalent load is a value representing the weighted contribution of the binned planet forces time series, such as that shown in Figure 2.17. Figure 2.27 compares the histograms of the planet bearing force time series from the three locations indicated in Figure 2.26.

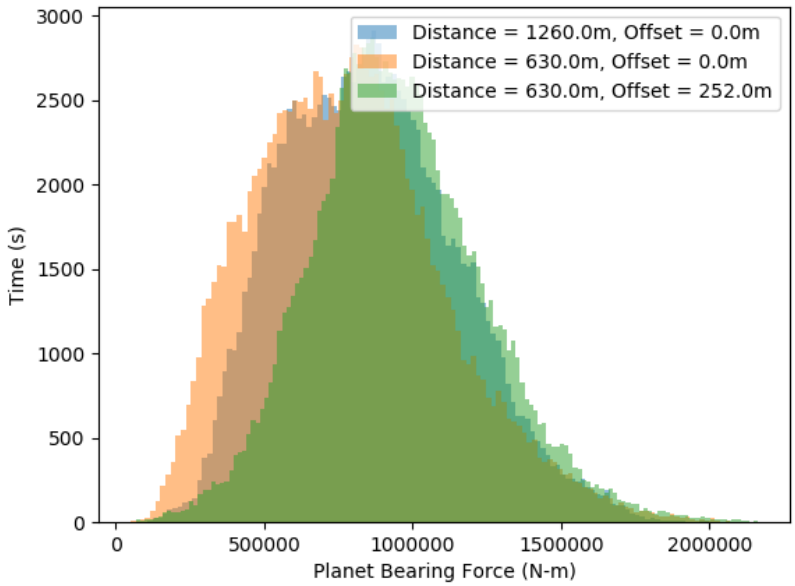

Figure 2.27: Histogram representing the planet bearing force time series at three locations

Figure 2.27 shows that the downwind turbine at Location 2, which is fully waked and closest to the upwind turbine, has the lowest mean planet bearing forces. The turbine at Location 1, which is directly behind the upwind turbine but at the maximum distance downwind from it, experiences higher mean planet bearing forces than the turbine at Location 2, but has a similar standard deviation to the turbine at Location 2. The turbine at Location 3, which is offset in the crosswind direction, has a smaller standard deviation and the highest mean planet bearing forces, but the longest tails of all three locations.

These results support the patterns seen in the L_{10} surrogate model, with increasing forces and decreasing reliability with increasing downwind and crosswind distance. Since these forces rely on main shaft loads, and therefore turbulence in-

tensity and wind speed, wind speed (U), the standard deviation of the wind speed (σ) and turbulence intensity (U/σ) for each of the 54 turbine locations are plotted in Figure 2.28. Turbulence intensity is a measure representing the variability of the wind velocity due to dissipation of the wind's kinetic energy into thermal energy via creation and destruction of progressively smaller eddies. In this study, the statistical definition of turbulence intensity is used:

$$TI = \frac{\sigma_u}{U} \tag{2.9}$$

where U represents the u-component of the wind velocity (along the x-axis defined in Figure 2.11), and σ_u represents the standard deviation of the u-component of the wind velocity.

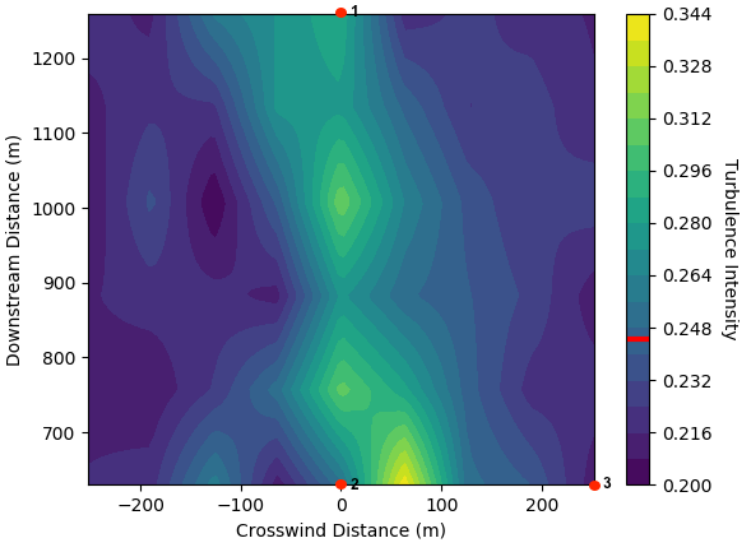

(a) Turbulence intensity (σ/U)

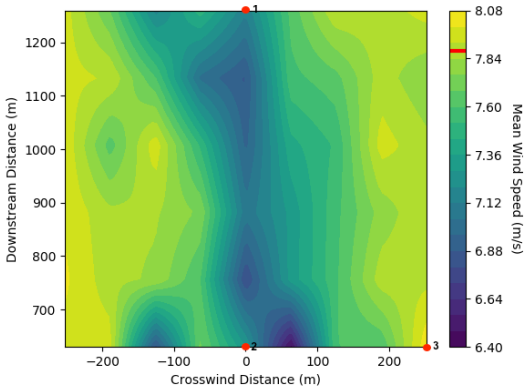

(b) Mean wind speed (U) (m/s)

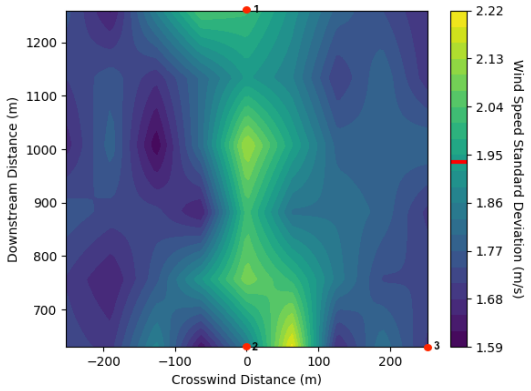

(c) Standard deviation of wind speed (σ) (m/s)

Figure 2.28: Turbulence intensities, mean wind speeds, and standard deviations of the wind speeds at different downwind turbine locations: the red lines on the color bars represent the reference value for the upwind turbine.

Figure 2.28a shows high turbulence intensity along the line x = 0D, near where one would expect the wake of Turbine 1 to be. There is a minimum near (-0.5D, 5D), with an area of higher turbulence intensity near (-1D, 5D). The area

of higher turbulence intensity meanders in the crosswind direction as downwind distance increases. Looking at the distribution of wind velocity at three optima (indicated by the red dots in Figure 2.28a), the difference in mean wind velocity and standard deviation can be more clearly seen. Figure 2.29 and Table 2.3 show the magnitude of the difference.

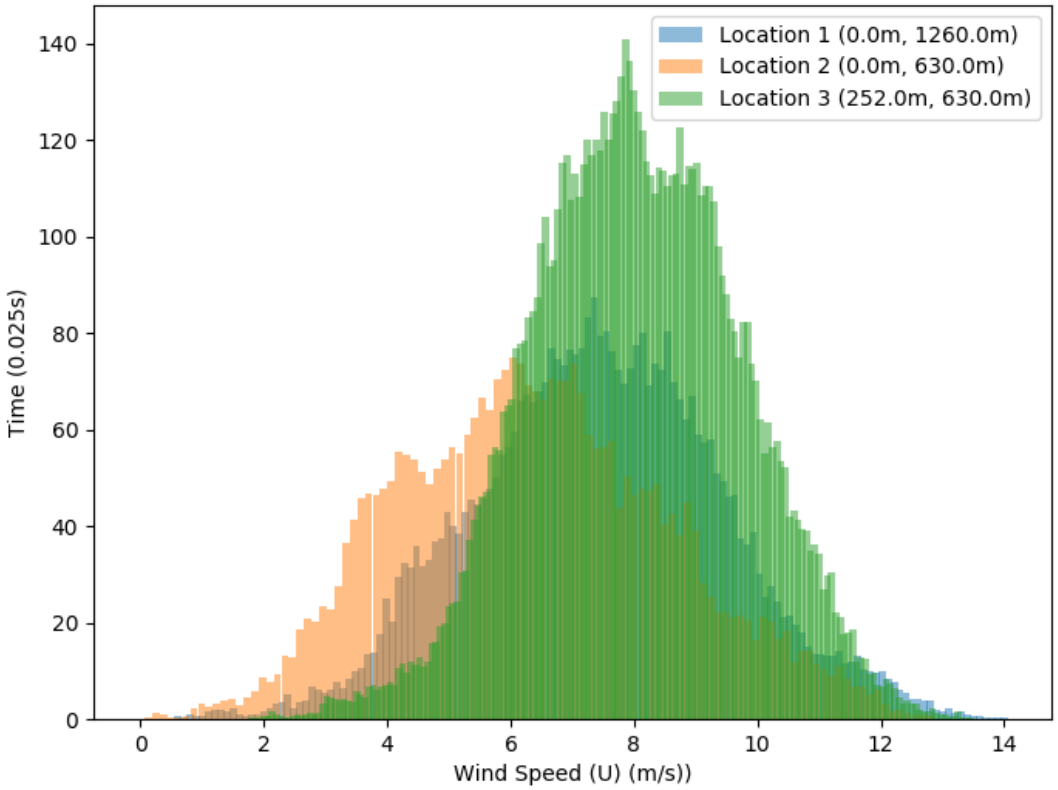

Figure 2.29: Histogram representing the wind speed at three locations

Looking at the corresponding velocity and standard deviation surfaces and the statistics used to develop them (Table 2.3), Figure 2.28b depicts a similar meandering, with velocity minima at approximately (0.5D, 5D), (-1D, 5D), and along a line from approximately (0D, 6D) to (0D, 10D). Figure 2.28c shows similar

Table 2.3: Wind speed (U) statistics for three locations

	Location 1	**Location 2**	**Location 3**
Mean	7.481672	6.441999	8.056694
Standard Deviation	2.041272	2.203938	1.700374
Turbulence Intensity (μ/σ)	0.272837	0.342120	0.2110511108763632
Minimum	0.604	0.002734	1.794
25% Quartile	6.124	4.814000	6.884
50% Quartile	7.485	6.363000	8.026
75% Quartile	8.838	7.932750	9.238
Maximum	14.1	12.93	13.52

patterns surrounding variability in the wind speed. These areas of low velocity and high variability, resulting in high turbulence intensity, suggest the path of the wake from the upwind turbine as it meanders traveling downwind. If this is true, I would expect higher planet forces in this region, higher equivalent loads, and therefore lower reliability. Contrarily, despite the evident decrease in mean velocity and increase in turbulence intensity, Figure 2.21 shows a region of high reliability near the line x = 0D, with the highest reliability closest to y = 5D. This indicates that velocity has a greater influence on equivalent loads, and therefore L_{10} values, than turbulence intensity. There are a few reasons this could be the case.

There is physical relevance for planet bearings to be more affected by wind speed than turbulence intensity, at least for this failure mode. Wind velocity drives torque loads, which dictates the number of revolutions each bearing makes, and therefore also the number of fatigue cycles experienced. Thus, wind velocity has a significant impact on L_{10} values, and the wind velocity trends mirror L_{10}

surrogate model trends.

Turbulence intensity, however, has a more nuanced relationship with planet bearing fatigue failure. Because turbulence intensity represents the variability in the u-component of wind speed, it does not take into account the variability in the y- and z-planes. All three components of velocity, and their variability, contribute to torque and non-torque bending moments on the main shaft. Specifically, torque contributes to bearing fatigue, but non-torque bending moments (especially pitching moments) can result in changes in bearing clearance and uneven distribution of load between the three planet bearings, significantly increasing the likelihood of failure, not just of fatigue, but of skidding or other failure modes [51]. Furthermore, bearing clearance reduced planet bearing load carrying capacity, so that loads are transferred to other components in the gearbox, such as gear meshes, reducing gearbox life.

Despite the importance of these non-torque loads, the drivetrain model used assumed even load sharing between the three planet bearings (or constant clearance and carrying capacity). This was done to isolate bearing fatigue as a failure mode and so that L_{10} could be used as a reliability metric, but the tradeoff is that bearing failure is limited to fatigue, which is mostly dependent on torque loads.

Turbulence intensity also has diminished effect on bearing life because of the standard way bearing life is estimated via the L_{10} metric. In Section 2.3.3, I described how the time series of planetary bearing forces is summarized via two weighted contribution statistics called equivalent speed and equivalent load. Although there was negligible variation in equivalent speed, the variations in planet

bearing forces from turbulence and planet bearing rotation and revolution (see Figure 2.17) were masked by the calculation of the single equivalent load statistic. Although the L_{10} metric is commonly used to describe bearing fatigue, it has limitations in this research context.

2.3.5 Surrogate Model Benefits, Limitations, and Future Work

Until now, the reliance on computationally-expensive wind turbine and array simulations, force calculations, and component reliability estimations have limited reliability-based systems level optimization of wind arrays. By building this framework to estimate component reliability from FAST.Farm simulations through a surrogate model, this research enables wind energy system optimization based on component reliability and power production. The code for this surrogate model has been developed in modules to allow users to substitute their own wind conditions, wind simulation software, component load models, and reliability metric calculations in efforts to increase its usefulness across the wind energy community. This surrogate model is a starting point for future reliability-based design optimization for wind energy systems, and has potential to be further developed and expanded for greater applicability.

Despite the benefits of this first framework iteration, there are several key limitations of this approach that must be understood so that the code can be used appropriately and improved in the future.

Foremost, this surrogate model is component- and failure mode-dependent.

The transfer of the output FAST.Farm loads to the planetary bearings is based on an analytical model that was verified empirically. To consider another component or failure mode would require similar model development and verification. Planet bearings are a critical failure component, so their failure is an important consideration in overall turbine reliability. However, planet bearings only constitute one critical failure component. To assess overall reliability of the turbine, all critical failure components need to be assessed simultaneously. Furthermore, while planet bearing fatigue life proved to be dominated by velocity and thus torque loads, other modes of planet bearing failure or other critical failure component life estimations may be dominated by turbulence and bending moments. By taking a holistic approach to defining critical failure modes and components and assessing their influence on system reliability simultaneously, offshore wind energy stakeholders can use the results of such a study as actionable information.

Not only is this framework component-dependent, it is failure mode-dependent. The calculation of reliability is based on the fatigue failure of the bearings. It does not consider ultimate loading nor uneven load sharing among the planet bearings. Inclusion of the most frequent failure modes for several critical failure components based on ultimate and fatigue loads would lead to more realistic turbine reliability estimation and is a future development goal for this framework.

Another limitation of this framework is the use of the L_{10} metric for reliability. L_{10} is the most common metric to use for planet bearing reliability, so for those who specialize in bearings, it is intuitive to use this metric. However, as discussed in Section 2.3.4, the L_{10} reliability metric relies on equivalent speed and

load calculations, which reduce the impact of planet bearing force oscillations and variability on the bearing life. Thus, the L_{10} metric accurately considers the influence of wind speed on the planet bearings, which is sufficient for fatigue failure, but insufficiently considers turbulence or uneven load distribution, which drive other failure modes.

Currently, this framework is based on a single wind speed and turbulence intensity condition over downwind locations listed in Section 2.3.1. The framework is set up to run FAST.Farm over a range of possible turbulence intensities and wind speeds, but has yet to be executed. Inclusion of this range of wind speeds and turbulence intensities is imminently planned so that future results can be based on a wind speed distribution and wind rose. Furthermore, the minimum in Figure 2.21 suggests that more optimal regions may lie in the space from y = 0D to 5D. Expansion of the surrogate model to include these arrays and the global optimums is forthcoming.

Finally, a convergence study of FAST.Farm simulations and cross validation of the surrogate model is needed. A convergence study of FAST.Farm will allow for the reduction of uncertainty and variability in load outputs, so that the surrogate model is built on a converged dataset. Cross validation of the surrogate model is needed to verify if the 54 datapoints used to build the surrogate model is a sufficiently large dataset. Cross validation will also allow us to quantify the uncertainty in the model, so that I can evaluate multiple interpolation methods, find the best fit for the dataset, and avoid error in L_{10} estimation originating from the interpolant method.

Now understanding the capabilities and limitations of this surrogate model, the following sections will discuss the implications of the surrogate model on the optimization.

2.4 Layout Optimization Algorithm Formulation

Traditionally, wind farm layout optimization problems optimize power production and cost objectives [33, 34, 42, 48, 59, 70, 75, 84, 86, 89, 94, 96, 97, 98, 102, 103, 112, 128]. This problem often is simplified into a wake avoidance problem. When wind passes through a turbine, energy is extracted and a wake is formed in which velocity decreases and turbulence increases. Since power production increases with increasing velocity and decreasing turbulence, wind farm array layout optimization results in minimizing turbine placement in waked zones. Despite this understood influence of wakes on wind turbine component reliability [53, 65, 109], incorporating component reliability into wind farm layout optimization problems is relatively unexplored.

In the fixed-foundation offshore wind energy market, loads and reliability are considered as static constraints during the design process, driven by design standards and guidelines modified from offshore oil platform guidelines for shallow-water developments. In reliability-based design optimization for wind energy systems problems, structural component parameters are optimized to meet failure constraints. Reliability is not considered as an objective. Considering reliability as a constraint for components has enabled the current status of offshore wind

energy, but achieving ambitious industry goals for reducing costs of energy will require considering reliability as an objective to reduce O&M costs and failures, not just across components, but systems.

RBLO combines wind farm layout optimization and reliability-based design optimization to consider reliability dynamically as an objective. Wake effects on reliability have been considered (albeit limited), and therefore can be leveraged in in layout optimization. This layout optimization method would directly relate coordinates of wind turbines in an array, and the environmental conditions at those coordinates, to component and system reliability and performance. In previous work, Sørenson et al. minimize wind turbine separation distance for Vindeby offshore wind farm to meet blade failure constraints [110]. Réthoré et al. optimize separation distance in a one-dimensional array at Middlegrunden for power production, electrical grid cost, degradation and O&M costs, taking into account tower base overturning bending moment [97]. In this work, I use the surrogate model described in Sections 2.3 and 2.3.4 to optimize wind array layout for gearbox replacement costs and power production.

2.4.1 Layout Optimization Methods

The purpose of this optimization approach is to explore the relationship between wind turbine array layout, component reliability, and failure costs by incorporating reliability as an objective, rather than as a constraint. The optimization problem is formulated in Equation 2.11:

$$\begin{aligned} \underset{C_f,P}{\text{minimize}} \quad & \mathrm{C_f}, \frac{1}{\mathrm{P}} \\ \text{subject to} \quad & d_{min} \geq 5D \\ & \text{boundary constraints} \end{aligned} \tag{2.10}$$

where C_f is the total cost of failure for the array over the array lifetime and P is the power of the array over the lifetime of the array. The optimization problem is subject to two inequality constraints: 1) a spacing constraint dictating no two turbines may be closer than the minimum distance, d_{min}, which is equal to five times the diameter of the turbine, and 2) a boundary constraint. The boundary constraint is flexible within the optimization, so that the user can define the shape and size of the array.

The cost model is represented by Equation 2.11:

$$C_f = C_{replacement} * x \tag{2.11}$$

where C_f is defined as the cost of gearbox replacement, $C_{replacement}$, which is equal to \$715920 [129, 135] multiplied by the number of replacements, x (Equation 2.12). The number of replacements is determined via the L_{10} surrogate model. It is assumed that, at the L_{10} planet bearing life, gearbox replacement is required. Power is determined by Equation 2.12:

$$P = P_{array} - DT * x \tag{2.12}$$

where P_{array} is determined from a surrogate model, pictured in Figure 2.30. This model was developed similarly to the L_{10} surrogate model: using FAST.Farm power outputs to estimate power at 54 array configurations and the RBF model to interpolate a surface based on these data point. This surrogate model is available via a GitHub repository [22].

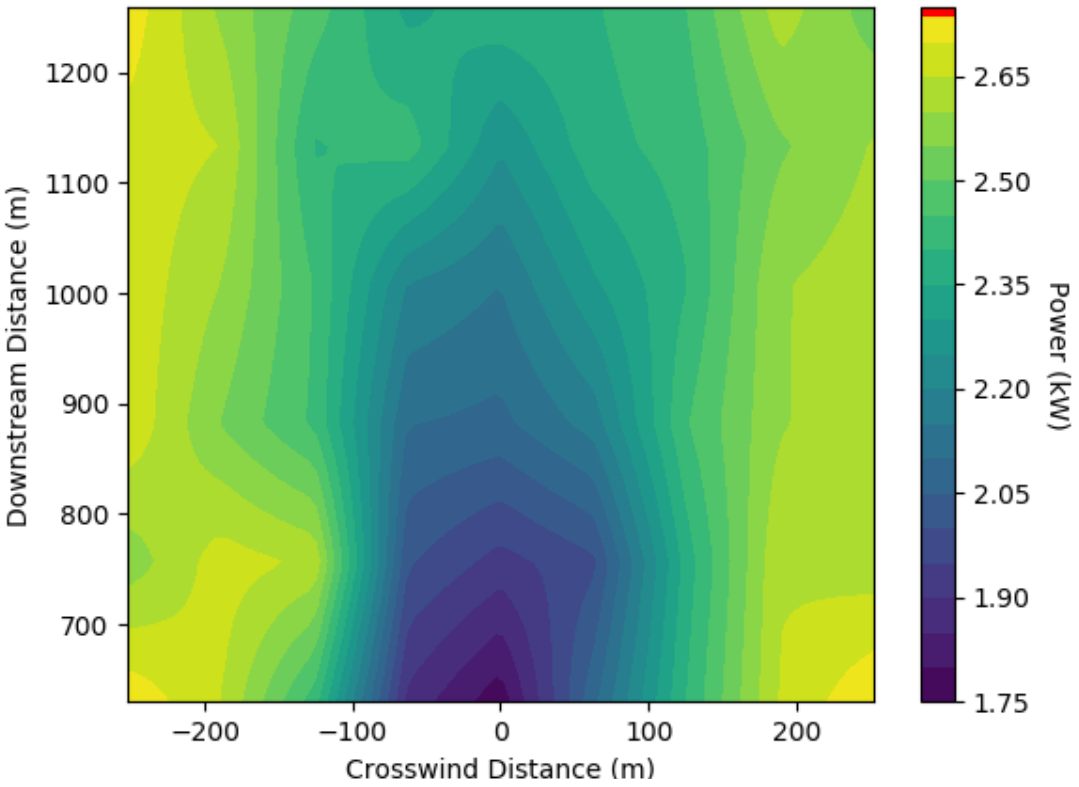

Figure 2.30: Surrogate model for power estimation of a downwind turbine

Downtime, DT, is assumed to be 230 hours [18], and x represents the number of replacements, so that P is equal to the power the turbines would produce over the lifetime of the array, less the downtime caused by gearbox replacement.

In this study, I use the Sequential Least Squares Programming (SLSQP) opti-

mizer from SciPy, a non-linearly constrained, gradient-based optimization method. SLSQP and other gradient-based optimization methods are particularly effective at solving problems with large design spaces and many design variables (significantly more than the number of objectives and constrains). They are also relatively computationally efficient due to rapid convergence rates with clear convergence criteria, but they also easily converge on local optima, so that global optimality is difficult to guarantee [91]. To overcome this disadvantage, multistarts are used, in which multiple random starting solutions are used to search the solution space and compare local optima [29]. In wind farm layout optimization problems, the design space and number of design variables is large, consisting of an x and y coordinate for each turbine in the array, each of which are continuous variables. Because of this large number of design variables, there are many locally optimal solutions, especially since the layout problem often is related to wake avoidance, which is relative between turbines. Small changes in one turbine location can cause similarly small changes in other turbine locations so that one locally optimal solution is not significantly different than another. Additionally, many dissimilar arrays may share the same evaluation, making it difficult report on a globally optimal layout. From Figure 2.31, it can be seen that 90-100 seeds are required before convergence is reached, or before the average of the seeds becomes constant, and no one optimization run is significantly leading to variation in the average objective function.

Beyond the multi-start, I also report on a set of optimal layouts that all have similar evaluations, which help elucidate the underlying patterns of the locally op-

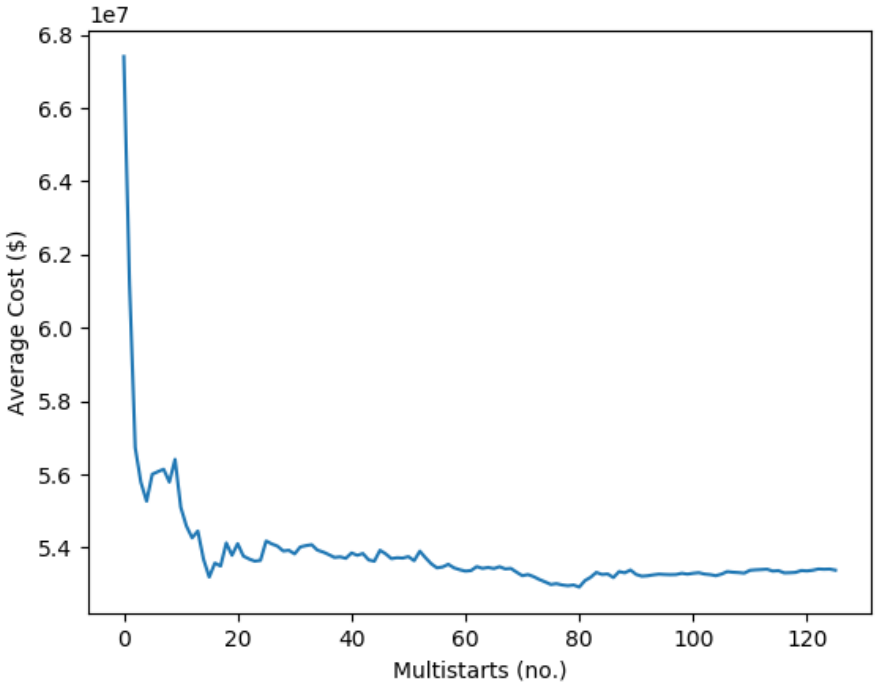

Figure 2.31: Convergence of the objective is achieved around 100 multi-starts

timal solutions and the relationship between power and reliability in layout design. As such, the purpose of reporting the following preliminary optimization results is to explore these relationships and test the framework developed for RBLO. Further surrogate model expansion and refinement, cost model development, and optimization algorithm tuning are required.

2.4.2 Layout Optimization Results and Discussion

The focus of this section is twofold: 1) to understand how incorporating reliability- and power-based objectives affects wind array layout optimization and 2) to demonstrate the use of this framework. To achieve these goals, this study employs a test

case consisting of a square, smaller array and simple wind conditions. The wind array contains, at most, 15 turbines, and the boundaries are set to be just large enough for the maximum number of turbines while maintaining the minimum distance constraint of 5D. The incoming wind is set to 8 m/s and IEC Class A turbulence intensity (16%). There are three incoming wind directions: 270°, 315°, and 0°, as depicted in Figure 2.32.

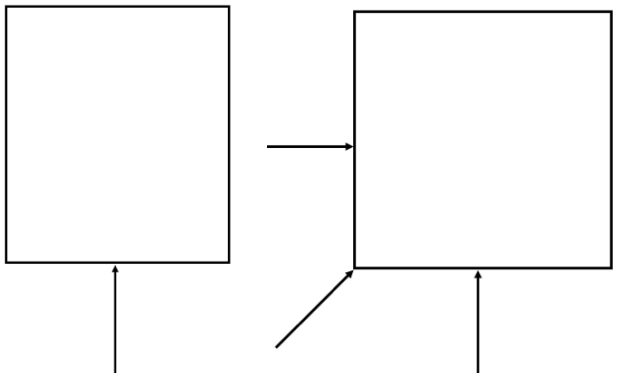

(a) Case 1 (b) Case 2

Figure 2.32: Wind direction cases: a) unidirectional (0°) and b) three wind directions (270°, 315°, and 0°), all of equal probability of occurrence

Considering the surrogate models for L_{10} (reliability) and power, it can be seen that the optimization algorithm will have competing objectives. In waked zones, the velocity is lower, which increases reliability but decreases power. In unwaked zones, the velocity is higher, which will increase the power and decrease the reliability. Figure 2.33a depicts the original and optimized layout of two turbines in an array for a cost of failure objective, and Figure 2.33b depicts the original and optimized layout for a power objective. Both of these figures have a single

incoming wind direction (Case 1). In Figure 2.33a, it can be seen that if the original spacing of the turbines is greater than 5D, the optimization algorithm places the turbines closer together so that they leverage the reliability minimum close to 5D. This is different than in Figure 2.33b, in which the turbines are placed farther apart (about 10D) to produce more power.

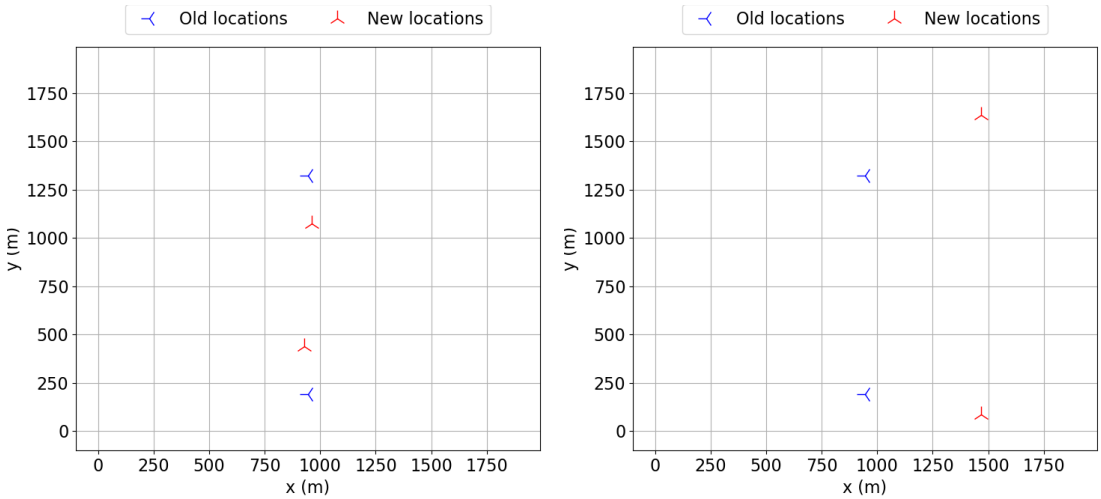

(a) Cost objective (b) Power Objective

Figure 2.33: A layout optimized for cost and reliability subject to a single wind direction (Case 1)

Minimizing cost by placing turbines closer in waked zones is consistent as the number of turbines and wind directions increase, although space becomes increasingly important in dictating layout with increasing turbines. Figure 2.34 and shows two example layouts of five turbines optimized for cost.

Figure 2.34a shows a layout with five turbines for a cost function and a single wind direction (Case 1), while Figure 2.34b shows the same array with three wind directions (Case 2). The turbines are arranged so take full advantage of the waked

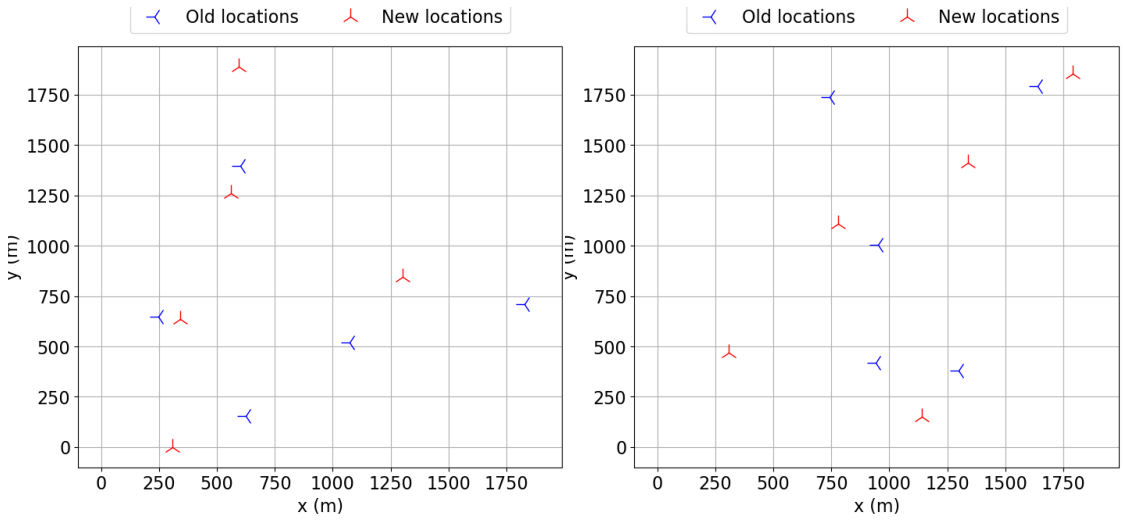

(a) One wind direction (Case 1) (b) Three wind directions (Case 2)

Figure 2.34: Layouts optimized for cost for five turbines under two wind direction cases

zones, with 5D separation distance between four of the five turbines in both wind cases. The fifth turbine, which is not able to be placed in the wake because of space constraints, is placed in a non-waked position.

Finding a balance between the two objectives will be further challenged by space constraints; as more turbines are added to the space, turbines will be forced closer together. In Figure 2.35, the average cost per kW per turbine decreases until about ten turbines, but then increases as the space becomes crowded with over ten turbines. This is due to the relative importance of energy production over failure cost reduction; while the turbines have enough space to avoid wakes and produce maximum power when there are less than ten turbines, more than ten turbines causes overcrowding of the space so that turbines can not produce power

optimally, despite the relative reduction in failure costs.

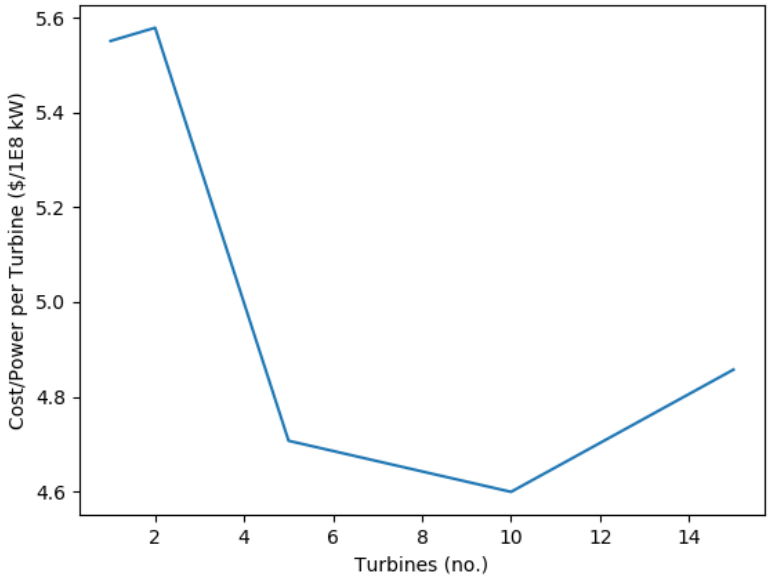

Figure 2.35: The most optimal layouts are achieved at approximately ten turbines. As the number of turbines increases to ten turbines, the cost per kW per turbine decreases from enhanced power production. As the number of turbines increases beyond ten turbines, the cost per kW per turbine increases due to overcrowding and degraded power production.

The dominance of the power objective is evidenced again in Figure 2.36. This Pareto curve shows the relative influence of each objective in the objective function (failure cost and power production), as they are weighted. The data point with the lowest failure costs is the average objective evaluation for a cost-only objective, with the next data point representing an objective of $\frac{0.9*\text{Cost}}{0.1*\text{Power}}$, then next $\frac{0.8*\text{Cost}}{0.2*\text{Power}}$, and so on until the last data point, which has a power-only objective. The relatively constant slope of the Pareto curve indicates that both power and failure costs are near equally dominant. The ideal balance between power production and failure

cost reduction is a cost weighting of 0.6. The error bars in this curve, however, indicate that there is a significant amount of variability in the objective evaluations. Therefore, the optimization algorithm needs to be further tuned and constrained to produce more consistent optimal layouts.

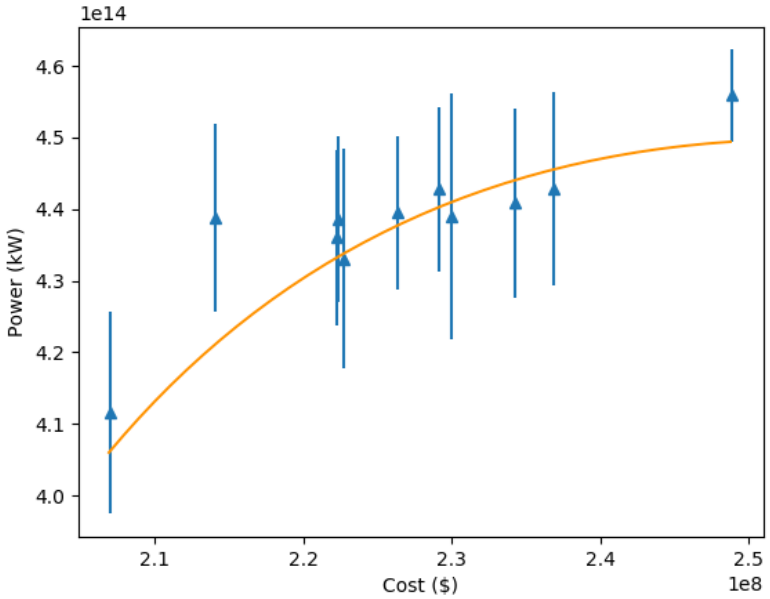

Figure 2.36: A Pareto front indicating subtle dominance of failure costs over power production

2.4.3 Layout Optimization Benefits, Limitations, and Future Work

Optimization results indicate a slight dominance of power between the failure cost and power objectives. Critical to this layout optimization study is inherent conflict between the two objectives, in which the failure cost objective drives turbine placement in waked regions with minimal downwind separation distance, and the power

objective drives turbine placement out of waked regions with maximum downwind separation distance. This interaction is influenced by space constraints, which decrease distances between turbines. While this is beneficial because of increased power production, overcrowding causes non-optimal layouts.

These preliminary results begin to provide insight into the relationship between reliability and power in wind array layout optimization, but there are still areas of the work that must be further developed and investigated to fully elucidate and validate results.

First, the optimization algorithm needs to be further refined so that optimal layouts are more consistent. Currently, there are many locally optimal layouts, with small translations or changes of the array resulting in multiple optimal solutions. There are also many layouts that obtain the same evaluation. Adding more turbines to the space reduces the number of locally optimal solutions, but then also drives artificial favoring of the reliability objective because failure costs are minimized when turbines are placed close together in waked regions. Tuning parameters to achieve the appropriate sensitivity of the gradient search will allow the algorithm to more effectively search the solution space, rather than get stuck in local minimums. Using a non-gradient based search algorithm is also a potential solution, so that there is more exploration of the solution space.

Second, this layout optimization approach considers simplified wind conditions for a small array. To obtain better estimates of wake interaction, more realistic wind conditions should be incorporated, such as the use of wind rose data, a wind speed distribution, and correlated wind speed and turbulence intensity conditions.

Further, this layout optimization is built on the interaction of an upwind and downwind turbine, so deep array effects or interaction of multiple wakes are not considered. Further development of the surrogate model to account for these effects could result in better wake-induced effects.

Additionally, preliminary optimization results suggest a need for heuristic optimization methods, rather than gradient-based. Figure 2.21 shows the presence of local optima, which generated a range of locally optimal layout solutions. To overcome this issue in this study, many simulations were run per case. However, even with replication, these simulations resulted in high standard deviation of objective evaluations (as seen in the standard deviation for power in Figure 2.36). Leveraging a heuristic method in the future would lead to more of the simulations finding the globally optimal layout, decreasing the variability in results.

Lastly, the failure cost model used in this optimization study is limited to the cost of gearbox replacements, so that the number of replacements and the cost of the replacement are the only variables considered. In the future, implementing a more sophisticated O&M model would result in more realistic costs associated with gearbox failure. To further this consideration, if a cost model that accounted for capital expenditures, operational expenditures, and decommissioning were included, this study could provide levelized cost of energy estimates, a result that may be more relevant and actionable to the offshore wind energy industry. Additionally, assumptions of the cost model, such as average downtime for gearbox replacement, were sourced from onshore and offshore data, and often did not contain detailed maintenance strategy details. O&M costs are highly context-dependent, so these

details about maintenance strategies, site-specific and time-dependent wave conditions, and location-specific O&M resources significantly impact resulting failure or O&M costs. Incorporating a more advanced O&M model that accounts for these details in an offshore-specific context would greatly benefit the understanding of the specific failure costs associated with this failure mode of planet bearings.

2.5 Conclusions

In this study, I chronicled the development of a framework for reliability-based layout optimization, in which component reliability is considered dynamically as an objective alongside power development. The inclusion of reliability in layout optimization is a conceptual demonstration of a more holistic approach for decision making in offshore wind energy systems. While this work advances reliability-based optimization and wind energy system design, there are key limitations to this work, and opportunity to continue to enhance its capabilities in future development efforts.

As part of this framework, I developed a surrogate model for the 5MW NREL reference wind turbine to estimate planet bearing life and power based on FAST.Farm output loads and offshore conditions. Surrogate model results suggest that power and planet bearing life are inversely related, so that power performance increases when wakes are avoided, while reliability decreases. This result is due to the methods used to estimate the planet forces and the reliability metric (L_{10} using equivalent load and speed) used in the surrogate model. By assuming the planet

bearings equally share the load, this model focuses solely on fatigue failure, whereas turbulence-induced non-torque bending moments drive other planet bearing failure modes. Further, the L_{10} calculation relies on velocity and torque as the main driver of planet bearing fatigue failure, whereas the effects of turbulence have a relatively minor influence. Thus, while power performance increases with increased velocity and decreased turbulence (outside waked regions), planet bearing reliability increases with decreased velocity (in waked regions).

Although alternative means of measuring reliability in planet bearings is required before layout optimization will provide results that adequately incorporate turbulence, the surrogate model enabled us to complete a framework for multi-objective RBLO of an offshore wind array so that the relationship between component reliability and wind energy system design could be investigated. The competing objectives of power and planet bearing fatigue failure resulted in optimized layouts that sought low velocity areas of wake, corresponding with maxima in the surrogate model.

Based on the results of the L_{10} and power surrogate models, layouts optimized for failure costs and power highlighted the conflicting nature of the two objectives. Failure costs were minimized when turbines were placed in waked zones, while power production was maximized when turbines were placed in non-waked zones. Preliminary results indicate that power production is slightly dominant over failure costs, but further testing and algorithm tuning is required to validate this finding. Spatial constraints in the optimization algorithm further enforced minimal spacing between turbines, so that there was an optimal number of turbines to achieve

maximum power production while avoiding overcrowding.

The major limitations of this work stem from the need for further development and extension of the surrogate models and the layout optimization framework. The surrogate model is component- and failure mode-dependent, but the modularization of the code enables it to accommodate user-provided component models and variable reliability estimation calculations. In future work, the code should be developed to investigate different failure components and modes with more detailed reliability metrics. Reliability metrics that better represent dynamic wind conditions (such as turbulence intensity) will be required to accommodate failure modes that are driven by turbulence.

Representing realistic wind conditions will be integral in future work for this RBLO framework. The surrogate model needs to be extended to more wind conditions so that a user-defined wind speed distribution and wind rose can be integrated into the layout optimization framework.

Furthermore, the surrogate model needs to be extended to incorporate downwind turbine distances less than 5D, and more crosswind distances. There is a minimum in the L_{10} surrogate model beyond the boundaries of the surrogate model, so extending the model space is integral to understanding the surrogate model scape. Validation of this surrogate model is also required to understand the inherent uncertainty in the model.

Related to the optimization scheme, further parameter tuning and result replication is required to create consistency in optimal layouts. Local minima currently reflect variability in optimal solutions, so refining the layout optimization scheme

to reduce the variability by using a heuristic method will aid in understanding the relationship between failure cost and power production in layout optimization. Additionally, this optimization scheme could be enhanced through the incorporation of a more advanced O&M cost model or a levelized cost of energy model and wind turbine control effects.

Collectively, the contribution of this work is twofold. First, this work provides insight into how component reliability may affect wind energy systems optimization. While the results in this study focus on planet bearing fatigue failure, they also reveal lessons on how to model component reliability in a systems engineering context. The choice of reliability metrics, for instance, plays an influential role in how wind conditions and system dynamics are retained in a model. As another example, while these results suggest that planet bearing fatigue failures depend primarily on velocity, other planet bearing failure modes or other components might be more affected by turbulence. Considering multiple critical failure components and failure modes simultaneously is a dynamic process within wind energy system analysis and optimization, and critical for understanding implications to wind array O&M. Second, it provides the first iteration of a framework to enable RBLO. With continued model development and open source code publishing, this framework will become increasingly relevant and accessible for collaborative development to the wind energy community.

To increase the relevance of this research effort within the wind energy community, it is critical not only to build capabilities for currently installed turbines and components, but to anticipate and build framework capability to incorporate

market trends. These market trends could include: increasing turbine size, installations farther offshore in deeper waters, floating platforms, and new end-of-life uses (i.e.: lifetime extensions and repowering). As wind turbine developers build increasingly larger turbines, this framework could be expanded and used to accommodate increasing and varying structural and mechanical loads. For example, if larger, heavier blades are able to reach higher altitudes where wind speed is higher and more consistent, mechanical and structural components throughout the drivetrain will be affected by increased blade tip speeds, as well as changing loads and vibrations. Significant design changes such as material use, internal structural component architecture, and direct drive systems will demand different ways of modeling reliability. For floating systems, this demand will be even greater as designers consider wave loads, floating platform dynamics, and the effects of those load dynamics on mechanical components. The industry's movement towards life extensions and repowering offshore wind turbines underscores the importance to consider reliability in design. If this framework has the ability to suggest system design changes that extend critical failure component life, the life of the installation could also be extended and considered in the initial design of the array to minimize its levelized cost of energy and maximize installation life. Providing the ability for others to integrate these design choices into this coded framework will provide opportunity for enhanced wind energy system design as the wind energy community continues to strive for market competitiveness.

Chapter 3: Reliability-Based Geometry Optimization of a Point-Absorber with PTO Structural Reliability Objectives

3.1 Introduction

As the wave energy industry progresses towards commercialization, research and development efforts to characterize and improve reliability of wave energy converters (WECs) have increased. Issues with reliability and survivability of WEC designs have previously led to setbacks for private developers including closure and delayed or limited testing of devices [26]. Moreover, component or system failure rates directly affect capital costs, operational costs, and power production. Therefore, designing WECs to withstand highly energetic wave conditions without over-engineering them is critical to overcoming industrial and development challenges and enable their implementation.

Despite the importance of considering WEC reliability in early design phases, it is often considered secondary to power production. Maximizing power production across sea states can increase revenue potential, but also loads and costs. Thus, there is a design trade-off between power production and component reliability that should be considered throughout the WEC design process. Particularly in device geometry design, there is an opportunity to reduce structural and PTO loads [26]. Optimizing WEC shape for reliability and power could decrease downtime and

required maintenance costs. Ensuring that WECs perform as they were designed for their intended lifespan, while decreasing the levelized cost of energy, is integral to improving their feasibility.

3.2 Previous Work

Only recently has reliability information been integrated into WEC design, but the body of literature that encompasses WEC optimization is extensive. Therefore, this literature review will focus on the most relevant previous research pertaining to reliability-based geometry optimization of WECs, addressing three research foci: 1) WEC hull geometry optimization for cost and power production, 2) reliability-based design optimization of WEC foundations, and 3) WEC hull geometry effects on varying component loads. These three bodies of work lay the foundation of theory and methods to address the focus of this paper: relating critical component reliability to WEC hull geometry optimization. For more information on how reliability information is and can be integrated into structural and mechanical design and analysis of WECs, refer to References [23, 132, 116, 3].

WEC hull geometries have been optimized for cost and power production,in which costs varied with device size [74, 13, 7]. Most geometry optimization studies were based on simple shape definitions such as using cylinders or spheres. A method employing bi-cubic B-spline surfaces has shown to be able to generate very diverse shapes [74]. This approach has been re-implemented and expanded to be applicable to a range of different cases, in which, for example, different combi-

nations of modes-of-motion for energy extraction can be taken into account [47]. Previous studies focused on maximizing power production, simplifying cost estimation, for example through the hull's submerged volume or surface area. However, reliability was not considered. An initial step towards reliability-based WEC geometry optimization was presented by Kurniawan et al., who included the reactive force on the hinge of an oscillating surge WEC [67] in one of the objective functions. Work has since been limited in this area by the computational expense of integrating force calculation and reliability estimation into an optimization scheme and finding a meaningful way to represent the impact of reliability on WEC design.

Although it has not been extensively applied to geometry optimization, reliability has been incorporated into WEC design optimization, where the focus has been on both structural and mechanical component dimensions and reliability. Ambuhl et al. optimized foundation diameter and thickness for the WaveStar device given structural pile failure constraints to maximize profitability [3]. Failure was considered as a constraint of the optimization problem (as it is commonly) rather than an objective. In this study, fatigue failures were identified to be a common failure mode in WECs, occurring at welded joints or corroded bolts. Yang et al. focus on a point absorber Power Take-Off (PTO) system much like the current study. Whereas the current work focuses on the structural modeling and analysis of the welded joint between the hull and the piston cylinder, Yang et al. use an abrasion model to model the wear of the piston ring by the piston cylinder [134]. Although they only consider one sea state, Yang et al. develop methods to address critical component failure in a PTO system, a major contribution of their study.

Although there has been limited work on reliability-based WEC geometry optimization, a few studies have provided insight into the geometry-dependent structural integrity of WECs. Beirao et al. compared three geometries (a sphere, a horizontal cylinder, and a vertical cylinder with a conical bottom) for a heaving buoy of a point absorber and their effect on component loads. Using Finite Element Methods (FEM), they considered loads on the supporting cables and PTO cylinder rod [10]. They found that, compared to a fully submerged buoy or a buoy floating at the surface, a partially submerged buoy experienced the greatest stresses and excursion. When the piston was retracted the highest loads were observed in the cables, whereas in its extended position both the rod and cables were identified as critical components. The sphere showed the lowest stress values in both cases. Van Rij et al. [120] compared the resulting PTO DELs from two point absorber floater geometries (a vertical cylinder with truncated conical bottom and a rhombus) and two mooring configurations (a monopile and a spar-plate configuration). Using computational fluid dynamics to obtain viscous drag coefficients for the WECs, Van Rij et al. generated PTO force data from the time-domain model in WEC-Sim. The rhombus float with a spar-plate configuration resulted in the lowest fatigue loads. These two studies inform the understanding of how WEC geometry relates to various component reliability. They, however, employed finite-element and computational fluid dynamics models, which are too computationally-demanding to be used within an optimization process.

This previous literature has enabled the current work, which addresses the opportunity to implement reliability-based design optimization of hull geometries to

design more optimal WECs. This would allow for hull geometries with advantageous reliability scores to be prioritized, balancing cost, power production, and reliability objectives. The current work consists of two main efforts. The first is to develop a method by which to relate environmental loads the WEC experiences to the reliability of a critical failure component, as well as evaluate the sensitivity of its reliability to varying hull geometries. The second is to use that method of reliability analysis and the knowledge of more or less optimal hull geometries within an optimization scheme. In this study, I focus on the first research effort, developing an assessment method to evaluate PTO damage at the welded joint between the hull and piston and establishing the relationship between WEC floater geometry and PTO reliability. Details about the optimization algorithm developed and used in this work can be found in Garcia-Teruel [46].

To complete the analysis framework, I leverage previous work that generates WEC hull geometries and performs hydrodynamic analysis, from which power production and PTO-forces for each geometry can be obtained [74, 47]. From this PTO-force time series, I use Rainflow Counting and appropriate S-N Curves to count the number of fatigue cycles and relate it to Damage Equivalent Load (DEL) metrics. Investigating various WEC hull geometries will allow us to evaluate and compare several hull shapes and their resulting PTO damage.

This study is divided into three sections. First, the methodology is described in Section 3.3, which 1) defines the case studies, met-ocean conditions, and WEC system characteristics, 2) describes the hydrodynamic model used to determine the PTO-force time series for each case, 3) details the fatigue DEL calculation based

on that PTO-force time series, and 4) briefly describes the optimization method. The results for both the reliability analysis and optimization are presented and discussed in Section 3.4. Conclusions and future work follow in Section 3.5.

3.3 Methodology

This section details the methods developed and used for the reliability analysis and optimization of the WEC hull geometry. To investigate the effect of WEC hull geometries on PTO DELs, I consider three different floater shapes, two energy absorption modes, and two geographic locations. I introduce the met-ocean conditions and the main characteristics of the WEC-system in Subsection 3.3.1. Section 3.3.2 details the hydrodynamic model used to generate the PTO force time series. Section 3.3.3 describes the fatigue analysis methods. Finally, a brief description of the optimization methodology is described in Section 3.3.4.

3.3.1 WEC System Definition

In this study, I analyze a point absorber type WEC oscillating in a single mode of motion (either heave, or surge). The WEC floater reacts against a PTO, such as a linear generator or a hydraulic piston, fixed 1) perpendicular to the sea bed, or 2) perpendicular to some vertical surface in the water column (see Figure 3.1). I assume the PTO system is composed of a moving rod welded to the floating body and a fixed component. Three different floater shapes were considered: a sphere, a

barge, and a cylinder. I chose the dimensions of the three shapes so that their draft and characteristic width would be equivalent. These dimensions are also shown in Figure 3.1.

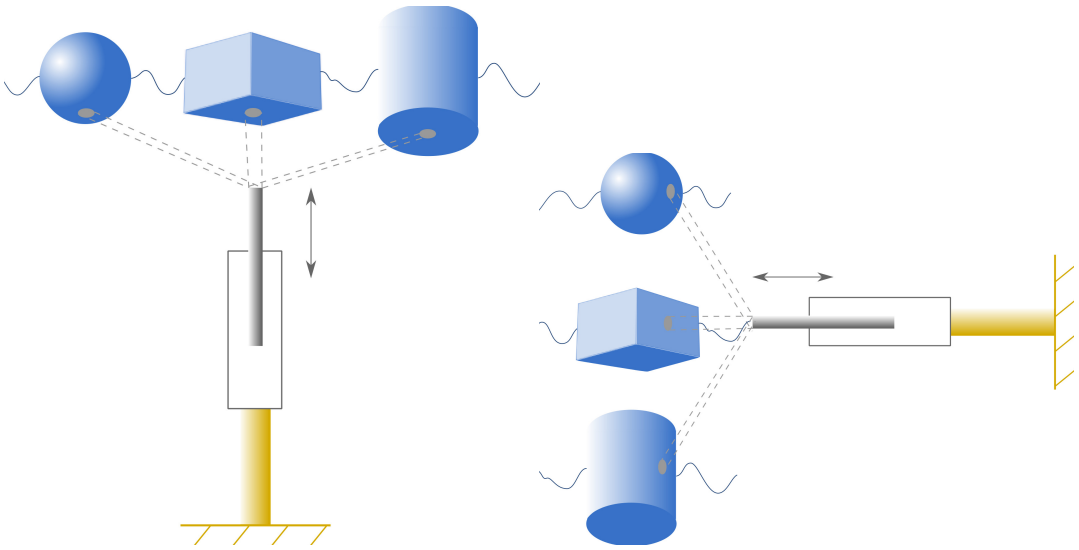

(a) Heave (b) Surge

Figure 3.1: Schematic representation of the WEC systems oscillating in (a) heave and (b) surge

3.3.2 Hydrodynamic Modelling

To model the sea states of the two locations, I first derived the characteristic sea states at each location, and then used the resulting significant wave height H_s, peak period T_p, and probability of occurrence as input for the WEC hydrodynamic model.

3.3.2.1 Study Areas and Sea State Conditions

To model the hydrodynamics of this system, I considered two geographic locations, each with their own set of characteristic sea states. I considered sea states 1) in the central North Sea and 2) off the southwestern coast of Norway (Figure 3.2). These two locations correspond to Site 15 and Site 14, respectively, of the European Union's MARINA Project (or Marine Renewable Integrated Application Platform) [108]. They were chosen for the availability of metocean data, as well as because their site conditions are distinct enough to compare WEC response dependence on location. For instance, the sites differ significantly in the average depth at the site, the level of protection from open ocean conditions, and the shape of the sea state conditions distribution. These site conditions are described in Table 3.1.

Table 3.1: Site Characteristics

	North Sea	**Norway**
Location	55.13N, 3.43E	61.85N, 4.23E
Water Depth (m)	29	200
Distance to shore (km)	300	30
50-year U_w at 10 m (m/s)	27.2	33.49
50-year H_s (m)	8.66	10.96
Mean value of T_p (s)	6.93	11.06

The MARINA Project provides marginal and joint distributions of wind and wave data for the study locations. The National and Kapodistrian University of Athens provided the 10 years (2001-2010) hourly raw data for the selected offshore sites. Both marginal and joint distributions are obtained by fitting analytic

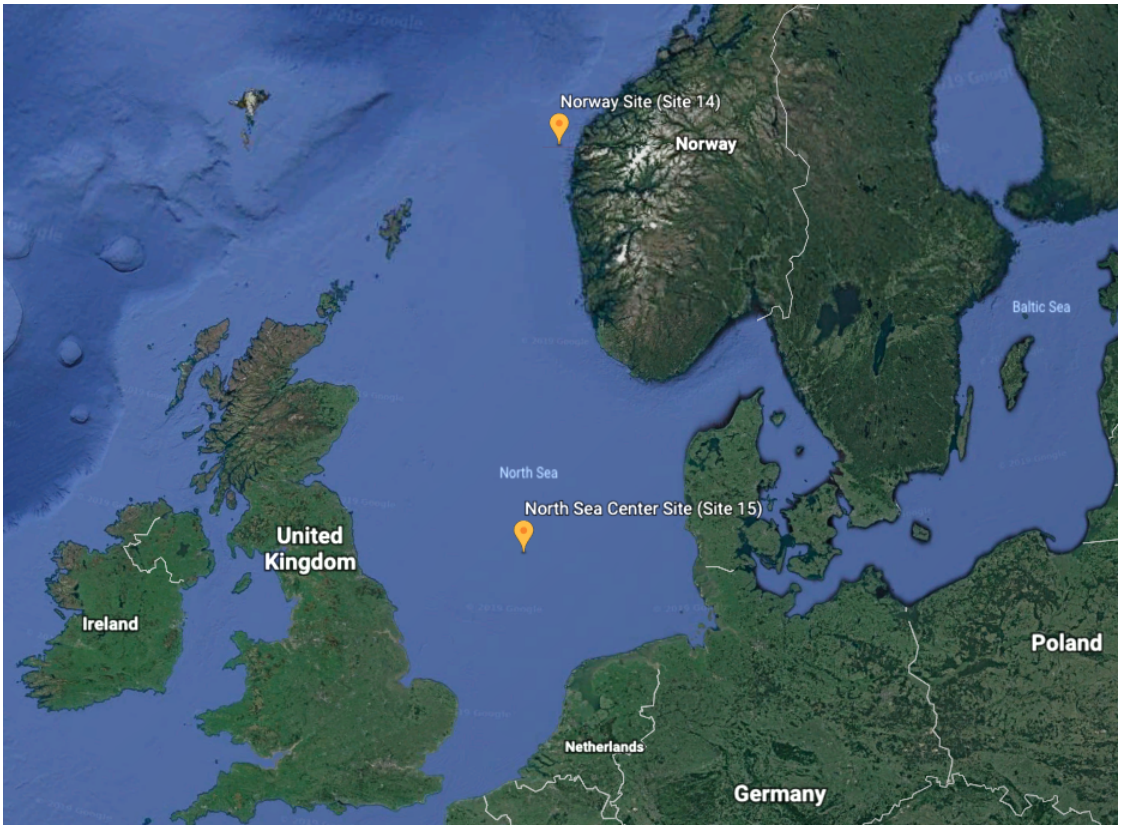

Figure 3.2: Site Locations: North Sea Center and Norway

solutions to raw data and are characterized by one-hour mean wind speed at ten meters above mean sea level (U_w), significant wave height (H_s) and spectral peak period (T_p) [69].

The joint Probability Density Function (PDF) of U_w, H_s, and T_p is defined by the marginal PDF of $U_w(f_{U_w})$, a PDF of H_s conditional on U_w ($f_{H_s|U_w}$) and a PDF of T_p conditional on H_s ($f_{T_p|H_s}$). The parameters and equations that define these distributions can be found in the original description of the site conditions [69]. The resulting representative sea states are described in Table 3.2 and 3.3.

For the purposes of this study, I assume the waves are unidirectional, approaching the WEC from the west.

Table 3.2: Characteristic Sea States for Site 15 (North Sea)

Sea State	H_s **[m]**	T_p **(s)**	**Prob. (%)**	**Occ./year (hrs)**
1	0.64	6.06	13.1	1145
2	0.73	6.13	8	698.2
3	0.77	6.17	2.1	186.2
4	0.8	6.19	0.3	27.9
5	1.26	6.55	5.8	512
6	1.43	6.68	17.3	1517.4
7	1.56	6.78	13.2	1154.3
8	1.63	6.83	3.9	344.4
9	1.66	6.86	0.6	55.9
10	1.69	6.88	0.1	9.3
11	2.22	7.28	1.9	167.6
12	2.37	7.4	9.5	828.5
13	2.51	7.5	8.5	744.7
14	2.58	7.56	2.6	223.4
15	2.61	7.58	0.3	27.9
16	3.21	8.05	0.6	55.9
17	3.35	8.16	3.9	344.4
18	3.48	8.26	3.5	307.2
19	3.55	8.32	1	83.8
20	3.59	8.35	0.1	9.3
21	4.21	8.85	0.2	18.6
22	4.35	8.96	1.4	121.09
23	4.47	9.06	1.1	93.1
24	4.54	9.11	0.2	18.6
25	5.22	9.68	0.1	9.3
26	5.36	9.8	0.4	37.2
27	5.47	9.89	0.2	18.6
			99.9	**8815.6**

Table 3.3: Characteristic Sea States for Site 14 (Norway)

Sea State	H_s **[m]**	T_p **(s)**	**Prob. (%)**	**Occ./year (hrs)**
1	0.67	9.48	3.3	282.2
2	0.70	9.51	3.9	335.0
3	0.73	9.55	1.1	92.7
4	0.77	9.59	0.1	9.5
5	1.50	10.30	7.2	615.9
6	1.54	10.33	12.5	1070.4
7	1.58	10.36	5.6	479.2
8	1.62	10.39	0.9	79.2
9	1.65	10.41	0.1	5.4
10	2.42	10.94	4.4	374.7
11	2.46	10.96	12.1	1035.5
12	2.51	10.99	9.4	806.9
13	2.56	11.02	2.5	212.9
14	2.59	11.04	0.2	21.3
15	3.35	11.46	1.1	93.7
16	3.40	11.48	5.3	541.4
17	3.46	11.51	8.2	699.5
18	3.52	11.54	3.8	327.5
19	3.56	11.56	0.6	49.4
20	4.30	11.91	0.1	10.1
21	4.34	11.93	1.1	92.2
22	4.41	11.96	3.8	326.4
23	4.48	11.99	3.7	315.4
24	4.53	12.01	0.9	479.8
25	4.56	12.03	0.1	6.4
26	5.29	12.33	0.1	8.6
27	5.36	12.36	0.9	78.9
28	5.43	12.39	2.2	185.5
29	5.50	12.42	1.1	91.7
30	5.54	12.44	0.1	11.3
31	6.30	12.73	0.1	9.3
32	6.38	12.76	0.7	62.4
33	6.46	12.79	0.8	72.0
34	6.52	12.81	0.2	15.6
35	7.33	13.11	0.1	11.0
36	7.42	13.14	0.4	36.0
37	7.49	13.16	0.2	16.3
38	8.37	13.46	0.1	10.4
39	8.46	13.49	0.1	12.1
40	9.42	13.81	0.1	5.9
			99.5	**8499.5**

3.3.2.2 PTO Force Estimation

To estimate the PTO force, the WEC motion at each location was analysed with a frequency-domain model. The model is based on linear wave theory, where wave height is assumed to be much smaller than wave length and water depth, and oscillations are assumed to be small. In this case, waves are represented as harmonic oscillations of different wave height and frequency, which can be linearly superposed to represent an irregular sea. For each sea state the relation of wave amplitude to frequency is defined by a Bretschneider spectrum, where 150 frequencies (ω_k) from 0 to 3 rad/s in 0.02 steps are analysed.

It should be noted that non-linear effects are not considered when using this method. This could lead to both under- or overestimation of the experienced forces. However, in [8], it was found that linear theory tends to overestimate the WEC dynamic response and absorbed power. With the purpose of developing a method suitable for hull geometry optimization at early design stages, the considered assumptions seem reasonable to provide upper limits of the system performance, while taking into account PTO-reliability.

Under these assumptions, the equation of motion of a WEC can be written as in (3.1), where the main forces affecting the motion will be the wave excitation force $\mathbf{F}_e$, the PTO-force $\mathbf{F}_{PTO}$, the WEC inertia $\mathbf{M}$, the radiation force composed of an added mass $\mathbf{M}_{rad}$ and an added damping $\mathbf{C}_{rad}$ terms, and the hydrostatic force represented by a stiffness term $\mathbf{K}_H$ following Archimedes principle. An additional damping term $\mathbf{C}_{loss}$ is included to represent friction losses as in [74]. The stiffness

value from the mooring lines is neglected, because it is considered to be much smaller than the hydrostatic stiffness value.

$$\hat{\mathbf{F}}_e + \hat{\mathbf{F}}_{PTO} = [-\omega^2(\mathbf{M} + \mathbf{M}_{rad}) + i\omega(\mathbf{C}_{rad} + \mathbf{C}_{loss}) + \mathbf{K}_H]\hat{\mathbf{X}}(\omega_k)$$

An idealised optimal control strategy is assumed, which sets the mass, damping and stiffness terms composing the PTO-force to match the impedance $\mathbf{Z}$, as defined in (3.1), at the energy period $T_e = 2\pi/\omega_e$. Here $\hat{\mathbf{U}}$ represents a vector of complex amplitudes of the oscillation velocity in six degrees of freedom, and $\hat{\mathbf{X}}$ is the corresponding vector of complex amplitudes of oscillation.

$$\hat{\mathbf{F}}_e = \mathbf{Z}\hat{\mathbf{U}} = \mathbf{Z}i\omega\hat{\mathbf{X}} \tag{3.1}$$

Then the PTO-force is defined by the complex conjugate of the impedance $\mathbf{Z}^*$ as shown in (3.2).

$$\begin{aligned}\hat{\mathbf{F}}_{PTO} &= -\mathbf{Z}\hat{\mathbf{U}} = \mathbf{Z}i\omega\hat{\mathbf{X}} \\ &= [-\omega^2(\mathbf{M} + \mathbf{M}_{rad}(\omega_e)) - i\omega(\mathbf{C}_{rad}(\omega_e) + \mathbf{C}_{loss}) \\ &\quad + \mathbf{K}_H]\hat{\mathbf{X}}\end{aligned} \tag{3.2}$$

The time series of the PTO-force $F_{PTO_{s,q}}(t)$ can then be obtained for each sea state s and set q of random phase shifts $\psi_{s,k,q}$ from the superposition of the single harmonic force representations at each frequency ω_k.

$$F_{PTO_{s,q}}(t) = \sum_{k=1}^{N} \left(\hat{F}_{PTO_s}(\omega_k) \cos(\omega_k t + \psi_{s,k,q} + \angle \hat{F}_{PTO_s}(\omega_k) \right) \tag{3.3}$$

Here, $\hat{F}_{PTO_s}$ represents each sea state component s of the vector $\hat{\mathbf{F}}_{PTO}$.

PTO-stroke constraints were first considered by setting the PTO-force to zero when the maximum stroke (5m) was exceeded, since it was assumed that the end stops would be taking all the load in this situation. It was found that setting the force to zero when the stroke limit is reached, might favor highly oscillating shapes. In those cases the DEL will not be representative for PTO reliability, because the end stops are not designed to be hit every 10 seconds. Within an optimization process the aim is to generate shapes, with a good trade-off between large enough oscillations for power production but small enough to minimize DEL. It is, therefore, recommended to not include this type of constraint for a better representation of the PTO reliability. PTO-stroke and rating constraints are, however, assumed here to calculate the average annual power as in [47], but are considered to have no effect on the PTO-force time series.

An example of the PTO-force time series for a heaving cylinder in the North Sea can be seen in Figure 3.3, where sea states are numbered according to Table 3.2.

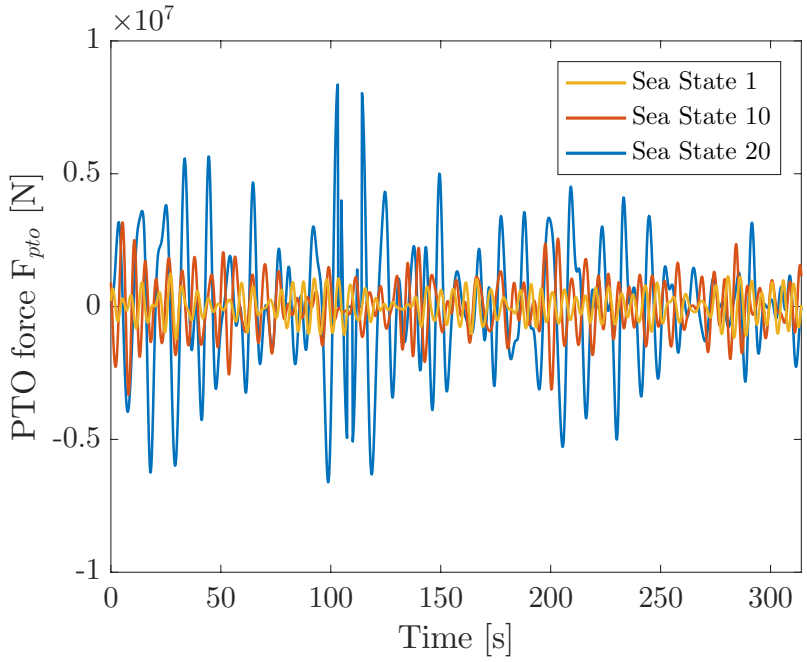

Figure 3.3: PTO force time series for a heaving cylinder in the North Sea for three different sea states

3.3.3 Fatigue Damage Analysis

In total, 10 PTO-force time series were generated for each case and wave condition, resulting in 1620 time series for the North Sea cases and 2400 time series for the Norway cases. Descriptions of these twelve cases are in Table 3.6.

The analysis focused on the fatigue failure of the rod weld connecting the floater to the PTO. Fatigue failures are speculated to be a common failure mode in WECs, occurring at welded joints or corroded bolts [3]. Furthermore, this type of failure has high technical and economic consequence, with the failure of the weld causing complete failure of the device and costly repair via re-welding either at sea or port.

Table 3.4: 5MW reference wind turbine gearbox specifications

Case	**Location**	**Motion**	**Shape**
1	North Sea	Heave	Cylinder
2	North Sea	Heave	Sphere
3	North Sea	Heave	Barge
4	North Sea	Surge	Cylinder
5	North Sea	Surge	Sphere
6	North Sea	Surge	Barge
7	Norway	Heave	Cylinder
8	Norway	Heave	Sphere
9	Norway	Heave	Barge
10	Norway	Surge	Cylinder
11	Norway	Surge	Sphere
12	Norway	Surge	Barge

After generating the force time series for a given case and sea state, I used the area of the PTO piston rod connecting to the hull to convert the force into stress. With the stress time series, I counted the number of stress cycles in that series with WAFO's Rainflow Counting algorithm [115]. I then used S-N curves to determine the cycles to failure of the weld given the selected material, the type of weld, and the magnitude of the stress cycles. I used DNV Standards on Fatigue Design of Offshore Steel Structures [30], specifically S-N Curve D in Table A5 for stress perpendicular to the weld, with a traverse splice in rolled sections. This curve assumes the weld is subject to seawater and has cathodic protection.

I binned the counted stress cycles by their amplitudes in 20 bins, as suggested by Wægter [125]. I then used Palmgren-Miner's rule to estimate the accumulated damage, or weld fatigue caused by each binned stress range for each sea state.

That is, for each bin, I divide the number of cycles in that bin by the number of cycles to failure for the given stress range. The cycles to failure, or the component capacity against fatigue, is determined by Equation 5.1.

$$n_c(s) = a_D s^{-m} \tag{3.4}$$

where $n_c(s)$ is the number of stress ranges (or the number of cycles) in a given amplitude, a_D is the intercept parameter of the S-N curve, s is the stress range (double the amplitude) in MPa, and m is the slope of the S-N Curve. These S-N Curve and Rainflow Counting details are included in Table 3.5.

Table 3.5: PTO fatigue analysis details

Parameter	**Value**
a_D	11.764e6
m	3
Rod Diameter (m)	6
Number of Force Range Bins	20
Lifespan (years)	20

The results for each sea state are then multiplied by the probability of occurrence during the lifetime of the structure to obtain a measure of the total fatigue damage. I repeat this for each case with ten PTO-force time series to gain an understanding of the variation in fatigue DEL, due to the random superposition of the wave frequency components.

3.3.4 Optimization Method

The optimization used in this study was a Genetic Algorithm originally developed by McCabe [74], and more recently, re-implementation and enhanced by Garcia-Teruel [46]. WEC hull geometries are defined based on a polyhedron symmetrical along the x-z plane. The corner points are used as vertices, between which further control points are defined through interpolation (Figure 3.4). The surface is then approximated by bi-cubic B-splines. Some of the vertices' coordinates are fixed, since the vertices lie on the free surface or on the symmetry plane, but the rest make up the genotype of the Genetic Algorithm and can be changed randomly within defined ranges to avoid open or physically irrelevant body shapes.

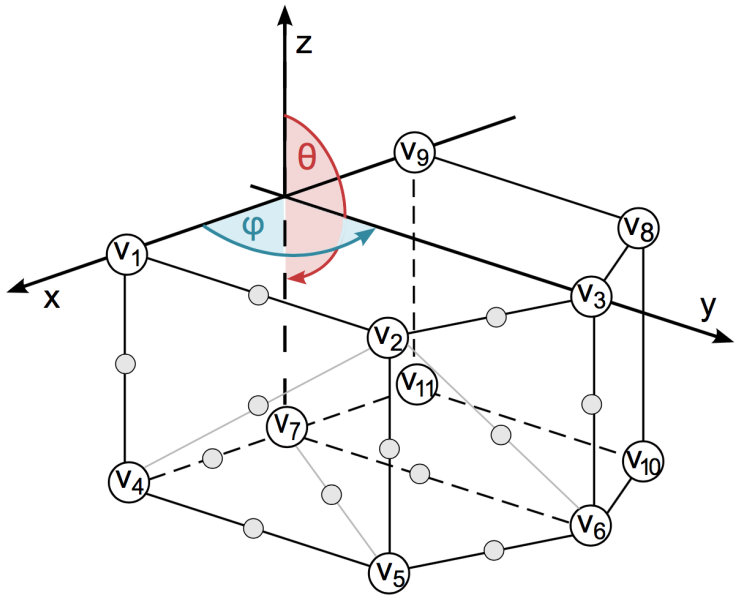

Figure 3.4: Polyhedron with numbered vertices and example representations of the interpolated control points in grey ([45])

The performance of each geometry for a particular side location is analyzed. The algorithm is implemented in Matlab and uses WAMIT–a frequency-domain program based on a Boundary Element Method (BEM)–to calculate the hydrodynamic characteristics for each shape based on the frequencies selected to represent the wave spectrum.

The objectives for this optimization include cumulative DEL, calculated through the fatigue analysis framework described in Section 3.3.3, and total power. The yearly average power is obtained via the sea states probability of occurrence. To normalize any results, the volume for each geometry can be obtained from WAMIT.

Constraints are instituted to maintain physically possible shapes. Radial coordinates, r_n are constrained by:

$$2.5m \leq r_n \geq 12.5m \tag{3.5}$$

Azimuth angles are constrained by:

$$\frac{\pi}{16} \leq \phi_n \geq \frac{15\pi}{16} \; n = 4, 5, 6, 10, 11;$$
$$\text{with } \phi_2 < \phi_3 < \phi_8;$$
$$\text{and } \phi_5 < \phi_6 < \phi_1 0;$$

Zenith angles (measured from the positive z-axis) are constrained by:

$$\frac{9\pi}{16} \leq \theta_n \geq \frac{15\pi}{16} \; n = 4, 5, 6, 10, 11; \tag{3.6}$$

Additional constraints are included to avoid the resulting optimal geometry being closed or crossing itself.

3.4 Results & Discussion

In this section, I separate results into two sections. Section 3.4.1 reports the results of the fatigue analysis for varying, hard-coded hull shapes. Section 3.3.4 then further develops those results through reliability-based shape optimization.

3.4.1 Fixed WEC Hull Fatigue Analysis

For the hard-coded WEC hull geometry fatigue analysis results, I partition the results by whether the WEC is heaving or surging and by its location (North Sea and Norway). The results are presented in terms of DEL absolute numbers, as well as normalized by the shapes' respective submerged volumes. This is done to eliminate the effect that the difference in submerged volume might have on fatigue results.

3.4.1.1 North Sea site

Figure 3.5 and 3.6 represents DEL results for the two motions of oscillation in the North Sea. Across the site-specific sea states, the heave case has lower DELs than surge case.

In both cases the trend of the Response Amplitude Operator (RAO) in heave and surge is reflected in the trends of the DELs. The RAO is a set of statistics that describe the likely motion of a floating structure. The DEL in heave increased with sea state. Figure 3.7 (a) indicates that the oscillation also increased with sea state. In the surge case a peak in DEL can be seen at Sea State 22. This coincides with the resonance period shown in Figure 3.7 (b). In conclusion, a relation between DEL behaviour, and RAO depending on period can be observed, that sets the overall pattern of the DEL.

When considering the DELs across shapes, the sphere results in higher DELs in the heaving case at high sea states, but the cylinder and barge have higher DELs at lower sea states. In the surging case, the cylinder and barge have consistently higher DELs than the sphere. However, the sphere shows the highest submerged volume normalized DELs in both, heave and surge, followed by the cylinder and then the barge. This is the case, because the sphere has the lowest submerged volume, followed by the cylinder and then the barge, which has two times the sphere's submerged volume.

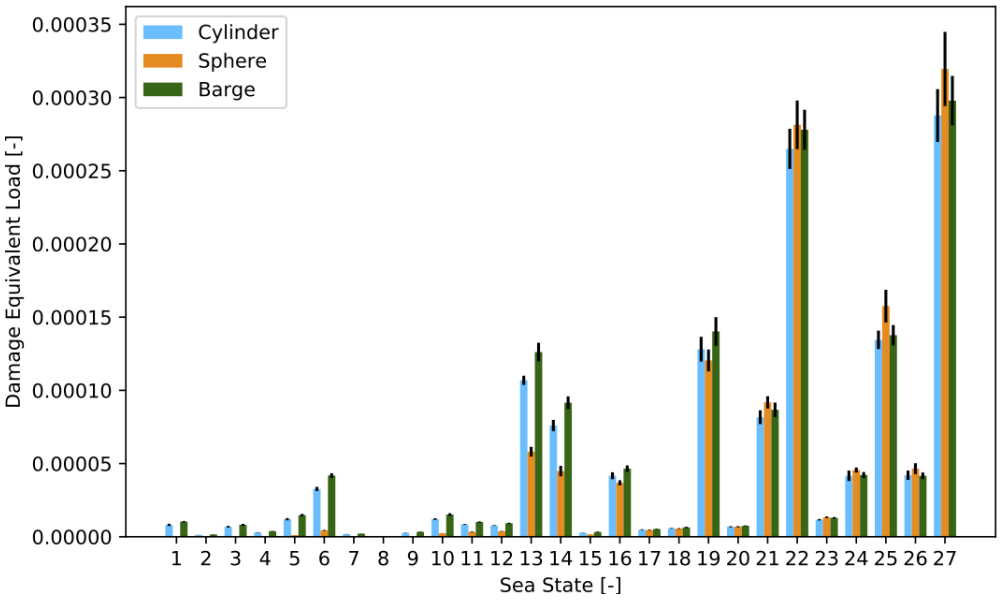

(a) DELs of a heaving WEC of varying shapes in the North Sea

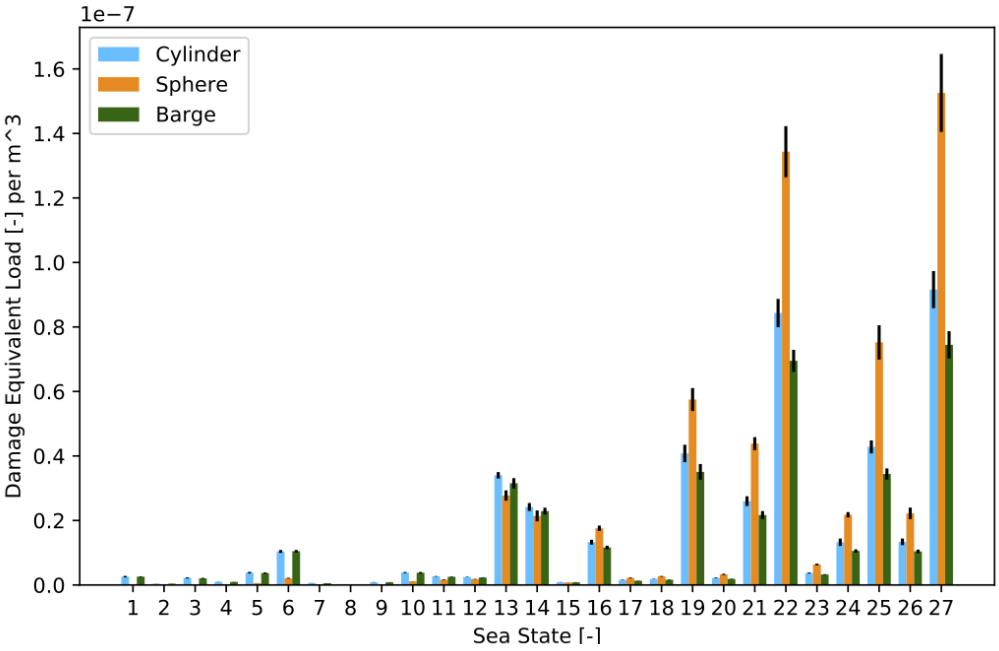

(b) DELs of a heaving WEC of varying shapes in the North Sea normalized by volume

Figure 3.5: Damage equivalent loads across sea states for a WEC of varying shapes in the North Sea oscillating in (a) heave and (b) normalized for volume

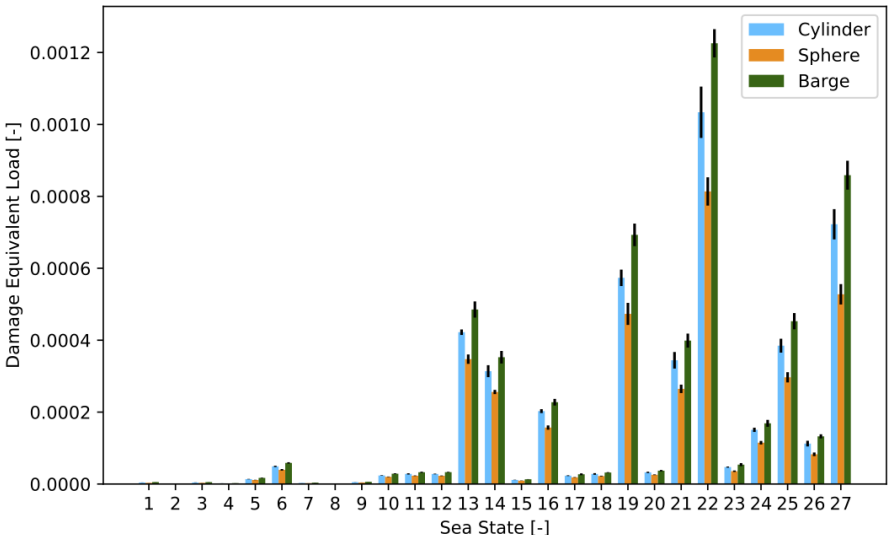

(a) DELs of a heaving WEC of varying shapes in the North Sea

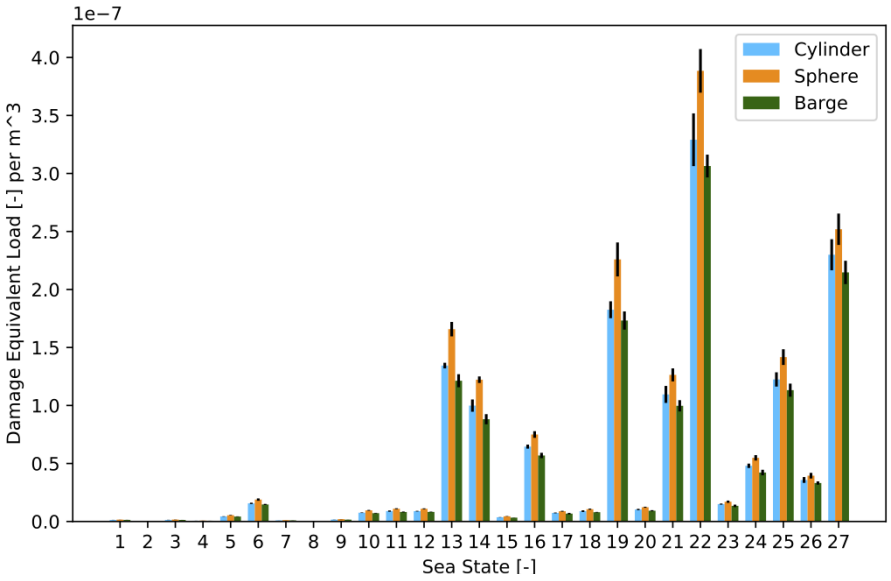

(b) DELs of a heaving WEC of varying shapes in the North Sea normalized by volume

Figure 3.6: Damage equivalent loads across sea states for a WEC of varying shapes in the North Sea oscillating in (a) surge and (b) normalized for volume

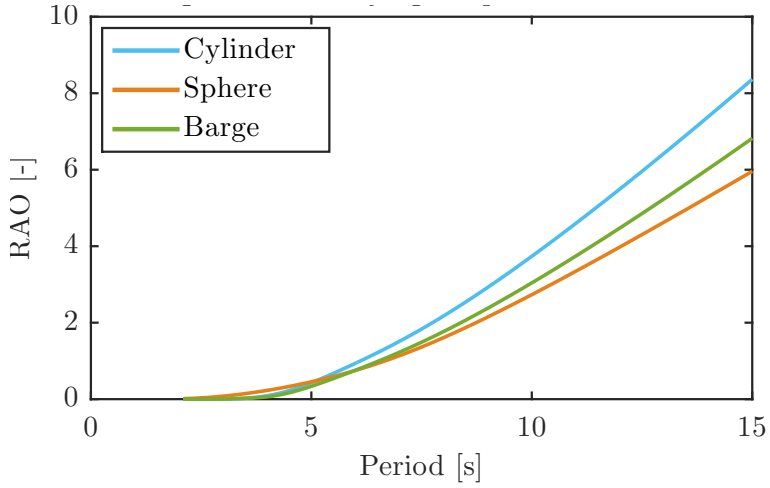

(a) Heave

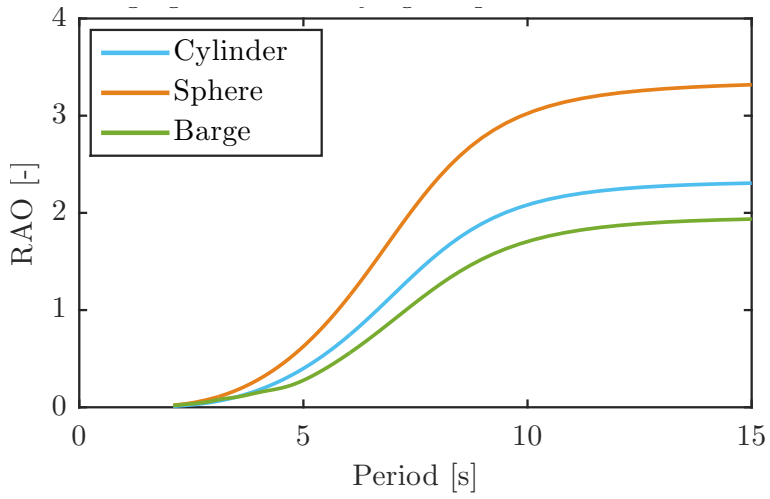

(b) Surge

Figure 3.7: RAOs of the different hull shapes in the North Sea oscillating in (a) heave and (b) surge

3.4.1.2 Norway site

Figures 3.8 and 3.9 depict the DELs for the two motions of oscillation at the Norway site. Here, contrary to the North Sea, higher DELs are obtained in the heave case than in the surge case.

Here again the trend of the RAO is reflected in the shape of the DEL diagrams. In the heaving case, an increase in DEL with sea state can be observed, which matches with the increasing RAO with period shown in Figure 3.10 (a). In surge, a peak in DEL can be observed in sea state 15, which coincides with resonance period shown in Figure 3.10 (b). The DEL is otherwise highest at middle-range sea states (20 to 24), which are slightly more energetic than sea state 15. There, T_p is between 11.9 and 12s, which still corresponds to the range of higher RAO's in Figure 3.10 (b).

When considering the DELs across shapes, in both heave and surge, the highest DELs are consistently achieved by the barge, followed by the cylinder and then the sphere. However, when looking at the submerged volume normalized DELs, in heave the order inverts with the sphere showing consistently the highest values.

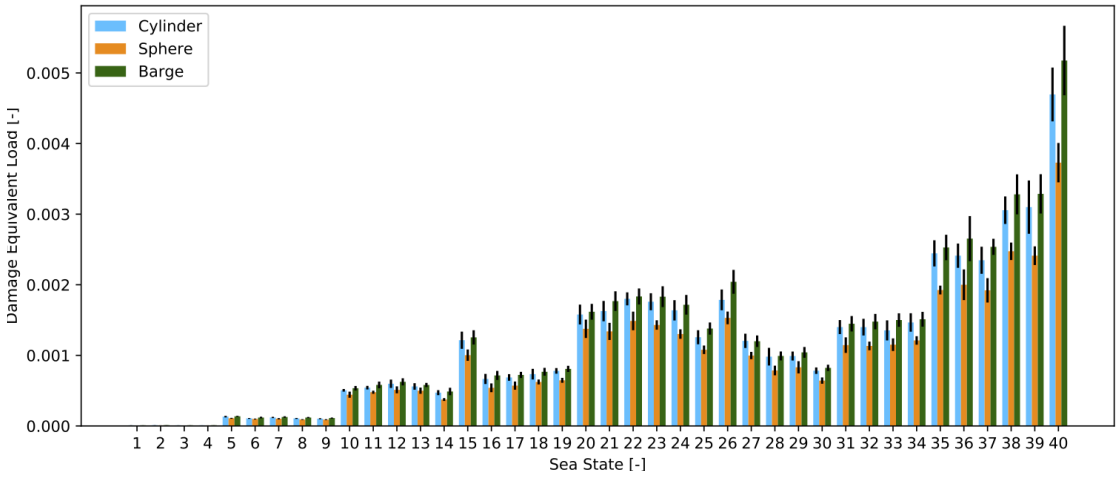

(a) DELs of a heaving WEC of varying shapes off the coast of Norway

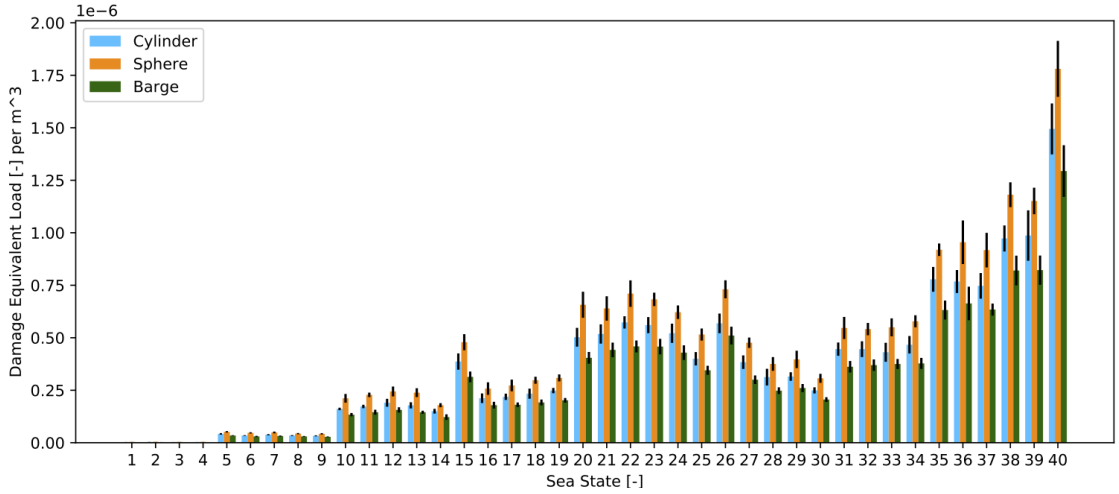

(b) DELs of a heaving WEC of varying shapes off the coast of Norway, normalized by volume

Figure 3.8: Damage equivalent loads across sea states for a WEC of varying shapes off the coast of Norway oscillating in (a) heave and (b) normalized for volume

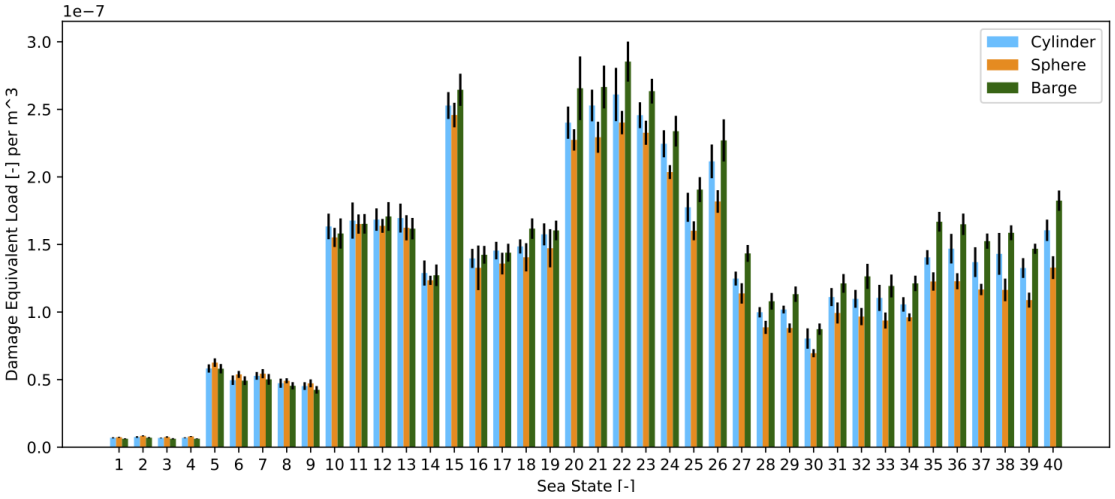

(a) DELs of a surging WEC of varying shapes off the coast of Norway

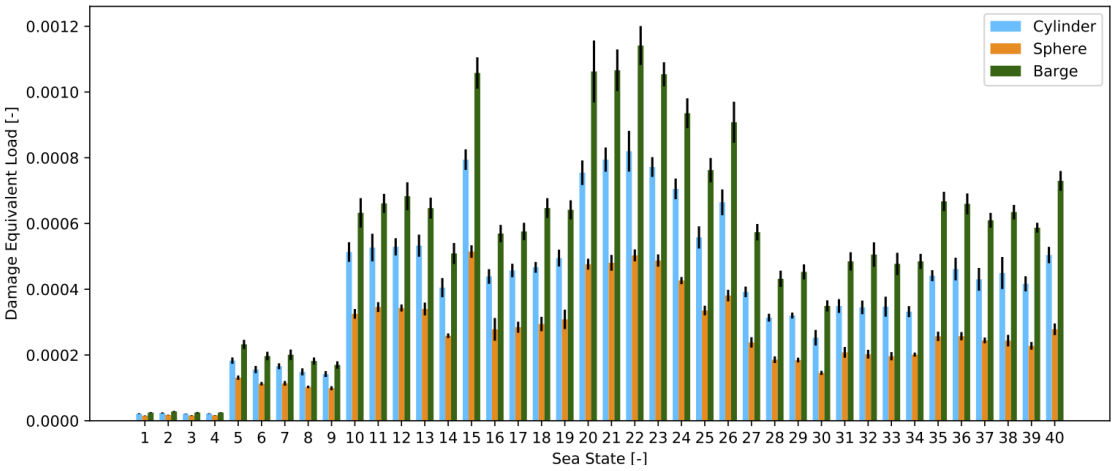

(b) DELs of a surging WEC of varying shapes off the coast of Norway, normalized by volume

Figure 3.9: Damage equivalent loads across sea states for a WEC of varying shapes off the coast of Norway oscillating in (a) surge and (b) normalized for volume

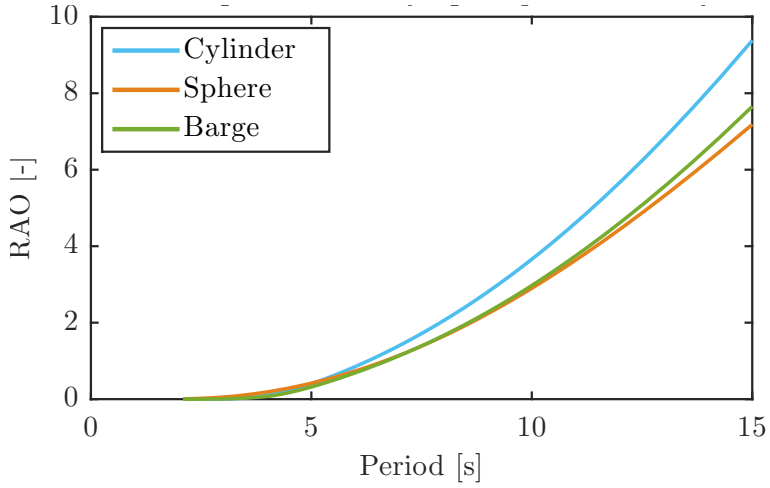

(a) Heave

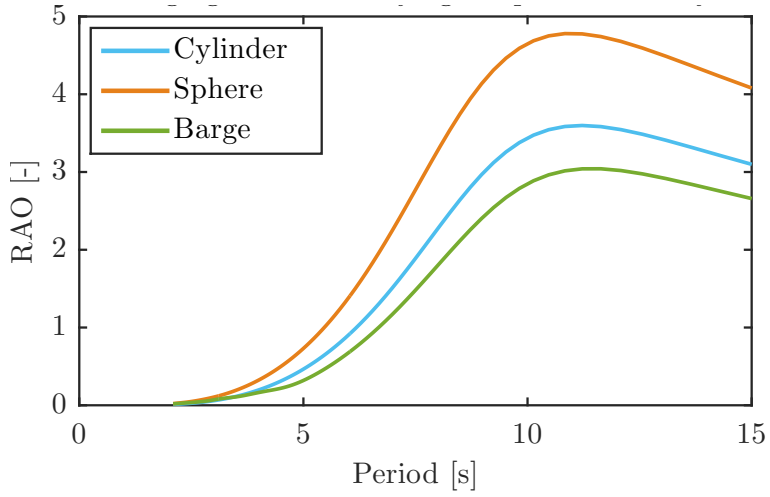

(b) Surge

Figure 3.10: RAOs of the different hull shapes of the coast of Norway oscillating in (a) heave and (b) surge

3.4.1.3 Across sites

The highest DELs are achieved in the heaving case in Norway, at the most energetic sea state. In the surging case the highest value is achieved in the North Sea in Sea State 22. It can be observed that peaks in DEL coincide either with higher energetic sea states (Norway, heave, Sea State 40) or with higher probability of occurrence of relatively high energetic sea states (North sea, surge, Sea State 22).

In the North Sea, the peak period T_p ranges from 6.06 to 9.89 s, whereas in Norway sea states start at a higher peak periods with a range from 9.48 to 13.81 s. When comparing, for instance, the heave RAOs of the three shapes, it can be observed that in Norway the RAO values are two times the ones in the North Sea for the relevant period range, which is reflected also in the difference in DELs for these two cases. This trend can also be observed in surge to a lower extent.

In the surging cases it can be observed that all shapes show a very similar performance when the DELs are normalized to the submerged volume. In the heaving case this is rather the opposite. The differences in DEL results become more accentuated when normalized to the submerged volume. This could point to a stronger dependency of DEL results from submerged volume in the surging case, and from shape in the heaving case.

Overall the performance of the different shapes, can be analysed considering also their annual average power production, shown in Table 3.6. The results indicate that the barge shape has the highest DELs across most cases and sea states, although it also achieves the highest power production in Norway in both heave

and surge, and the second highest in the North Sea, when compared to the other shapes. The reason for this, can be the higher submerged volume of the barge, which is approximately two times the submerged volume of the sphere and 1.2 times the submerged volume of the cylinder. In contrast, the spherical shape has the lowest DELs across most cases and sea states (agreeing with Beirao's results [10]), and produces the highest power in the North Sea in both heave and surge, and performs similarly to the barge in Norway. However, when looking at the submerged volume normalized DELs the sphere has the highest DELs in the North Sea and in the heaving case in Norway. This shows that the sphere with a lower volume than the barge achieves better overall results. When taking into account its submerged volume the sphere performs worse in terms of DELs, but better in terms of power.

Table 3.6: Power Production Across Cases

Case	**Location**	**Motion**	**Shape**	**Average Power [kW]**
1	North Sea	Heave	Cylinder	143
2	North Sea	Heave	Sphere	158
3	North Sea	Heave	Barge	145
4	North Sea	Surge	Cylinder	29
5	North Sea	Surge	Sphere	35
6	North Sea	Surge	Barge	30
7	Norway	Heave	Cylinder	547
8	Norway	Heave	Sphere	591
9	Norway	Heave	Barge	592
10	Norway	Surge	Cylinder	428
11	Norway	Surge	Sphere	524
12	Norway	Surge	Barge	528

3.4.2 WEC Hull Geometry Optimization

When considering resulting optimal hull shapes, the shapes are more similar among the type of motion (heave and surge) rather than the site wave conditions (North Sea and Norway). Therefore, the hull geometry optimization work is firstly divided by the motion type and secondly by site. Objectives are formulated in the optimization problem to be minimized, therefore, DEL is minimized (since reducing damage is preferred) and power is multiplied by -1 in the objective function to be minimized (since power production is preferred).

3.4.2.1 Heave Motion

Figures 3.11a and 3.11b shows Pareto fronts for a heaving WEC at the North Sea and Norway site. Generally, Pareto fronts show the set of optimal solutions for a given multi-objective problem; all points along the Pareto front could be the most optimal solution, depending on the preferred weighting of the objectives. These Pareto fronts show each objective (DEL and power) on each axis, so that the data point with the highest DEL weights the DEL objective fully, while the data point with the highest power weights the power objective fully. The data point that is closest to the origin achieves the optimal solution in the Pareto set that minimizes both objectives (achieving the optimal balance)(also called the Pareto point).

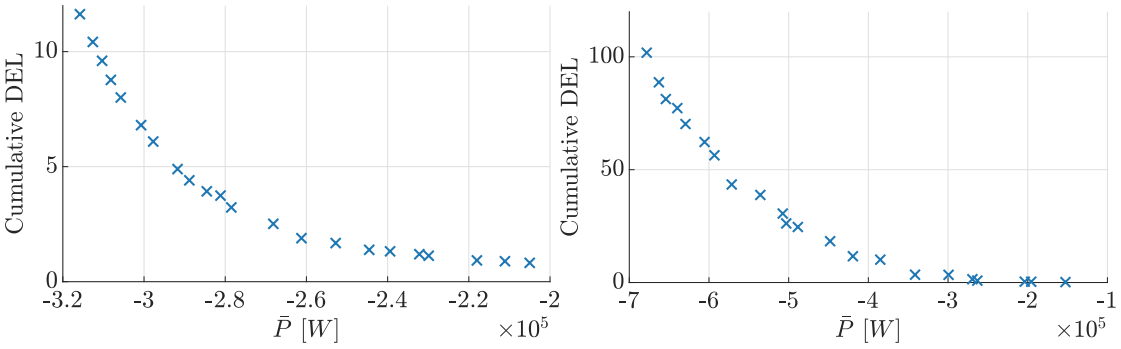

(a) Heave, North Sea

(b) Heave, Norway

Figure 3.11: Pareto fronts for multi-objective optimization with objective functions $-\bar{P}$ and DEL_{cum}

In the Pareto fronts in Figure 3.11, the Pareto point represents an objective in which DEL dominates over power, but only slightly. This means that DEL and power are relatively equal in influence over this objective. If I were to change the objective, however, this equal influence might change. For instance, if I were to assign a cost value to failure consequences and power produced, this dynamic might change to give the objective with the greatest revenue or cost dominance.

Additionally, between the two sites, there is a discrepancy in the magnitude of the two objectives. DEL values reflect a magnitude difference between the DEL values at the North Sea and Norway sites, while the power values have a much larger range. This is thought to have to do with the larger range of sea states at the sites, with the North Sea site having smaller sea states and a smaller range of sea states, whereas the Norway site not only experiences greater average and maximum nominal sea states, but also greater variability in the sea states. This underscores the sensitivity of each objective, particularly DELs, to site-specific sea

states. From a design perspective, this highlights an opportunity to design more robust WECs, so that they are minimally sensitive to changes in these factors that affect performance variability.

Figure 3.12 shows three optimal hull shapes for the solution that fully weights the DEL objective, the solution that fully weights the power objective, and the Pareto point, across the North Sea (Figures 3.12a, 3.12c, and 3.12e) and Norway sites (Figures 3.12b, 3.12d, and 3.12f).

There are two major characteristics that can be seen from the optimal shapes across sites and the Pareto front. First, the size of the device is inversely related to the DEL objective, and positively related to the power production. Larger device produce more power, but experience greater damage equivalent loads (Figures 3.12a, 3.12b. Therefore, the Pareto optimal point is medium-sized, relative to the two solutions at the boundaries of the Pareto front. Second, the shape of the hull is pointed on the bottom and flat on the top. This is thought to be related to the heave motion. A larger, more convex shape achieves a greater hull volume, buoyant force, and thus power. A smaller, more concave shape reduces the loading in the heave motion due to this buoyant force. Similarly, orientation of pointed features, especially evident in Figure 3.12c and 3.12e, are thought to be driven by the DEL objective, reducing surface area for oncoming waves so as to reduce loads.

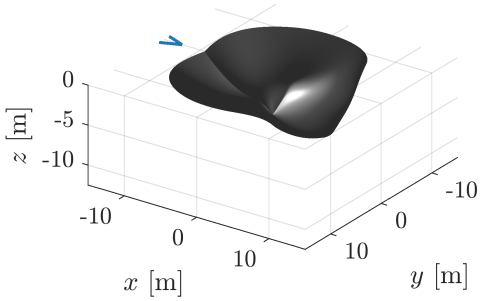

(a) DEL=11.627, $\bar{P} = 315.788$ kW

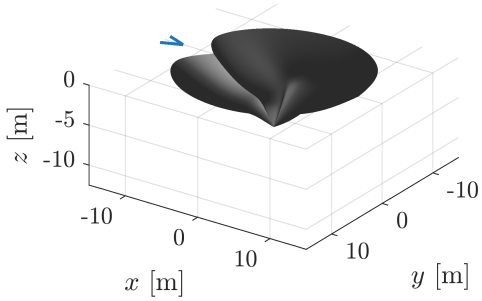

(b) DEL=101.827, $\bar{P} = 678.151$ kW

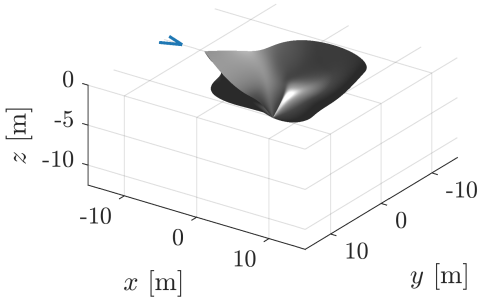

(c) DEL=3.742, $\bar{P} = 281.169$ kW

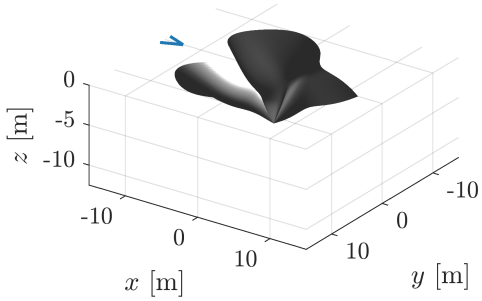

(d) DEL=26.180, $\bar{P} = 503.048$ kW

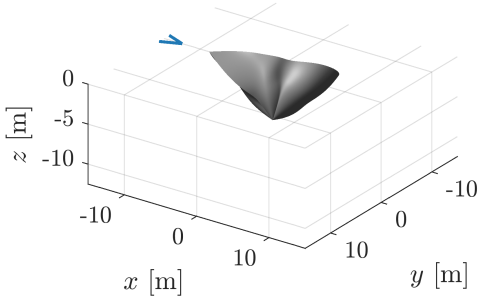

(e) DEL=0.817, $\bar{P} = 205.006$ kW

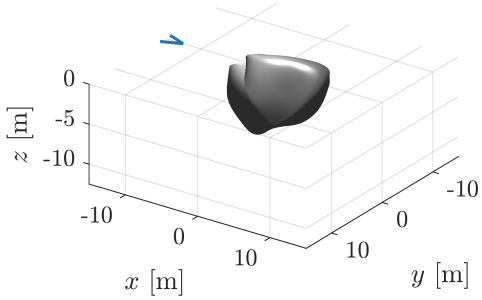

(f) DEL=0.205, $\bar{P} = 152.682$ kW

Figure 3.12: (a), (c) and (e) represent the optimal shapes on the DEL-$\bar{P}$-Pareto front for a heaving device in the North Sea, and (b), (d), (f) represent the optimal shapes for a heaving device off the coast of Norway. (a) and (b), and (e) and (f) represent the respective Pareto front limits, and (c) and (d) represent an optimal geometry in the central area of each Pareto front.

3.4.2.2 Surge Motion

Pareto fronts for a surging WEC at the North Sea and Norway sites are depicted in Figure 3.13. Compared to the Pareto fronts for the heaving cases, the cumulative DEL value is higher, especially at the North Sea site. Power and the range of power values, however, is reduced. Thus, the resulting Pareto optimal point for a surging device experiences higher DELs and lower power production. This suggests that a heaving point absorber type WEC could produce more power and experience fewer PTO weld failures than a surging device.

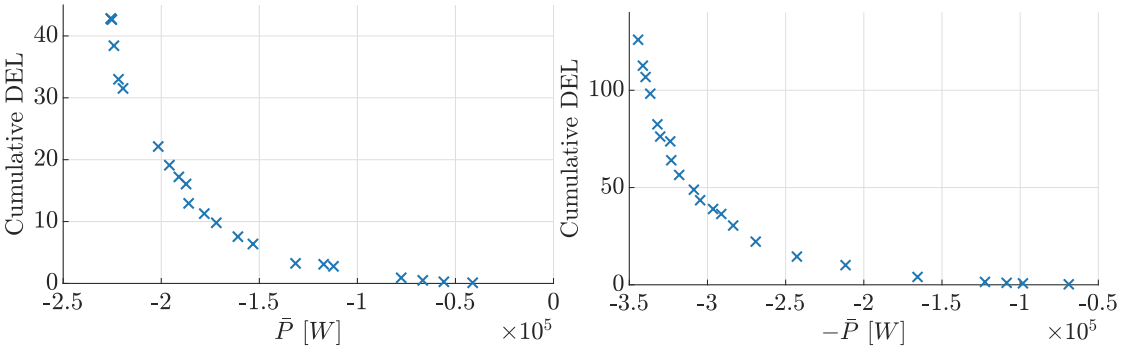

(a) Surge, North Sea

(b) Surge, Norway

Figure 3.13: Pareto fronts for multi-objective optimization with objective functions $-\bar{P}$ and DEL_{cum}

The hull geometries in Figure 3.14 are larger and more convex than their heaving counterparts (as seen in Figure 3.14c and 3.14d). Compared to the heaving case shapes which minimize DEL with their pointed bottoms, the geometries which minimize DEL in the surging cases have ridges facing the directions of motion, thought to decrease the loads by minimizing the surface area in this direction. For Figures 3.14a through 3.14d, there are less of these features, and more convex shapes,

which indicates that the power objective has more dominance in the surging case than the heaving case.

Collectively, these results indicate that geometry, size, as well as direction of motion and siting are important factors in PTO DEL loads. Geometry, both overall shape (sphere, barge, cylinder) and a more complex geometry (concavity, convexity, and pointed or edged features) affect DEL and power. Increased size and convexity result in increased power production, whereas smaller sizes and concavity produce minimized DELs. Heaving WECs have more variability in power production, especially across sites. Surging WECs have less variability in power produced (even across sites). Both heaving and surging cases experience more variability in DELs across sites, indicating that local sea state is a main driver of PTO DELs. While DEL and power objectives were relatively equally dominant in the heaving case, power dictated hull geometry more in the surging case. Overall, more optimal shapes were achieved through the heaving WEC, rather than the surging WEC.

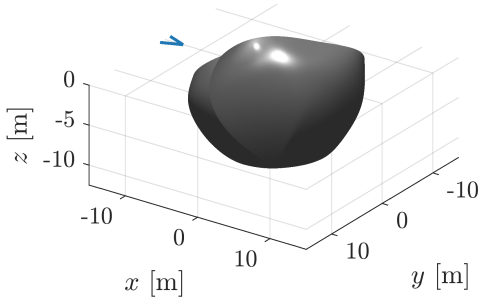

(a) DEL=42.806, $\bar{P} = 225.703$ kW

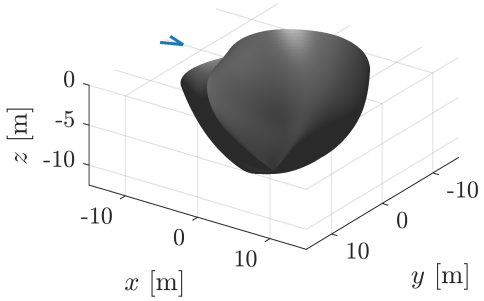

(b) DEL=125.961, $\bar{P} = 344.383$ kW

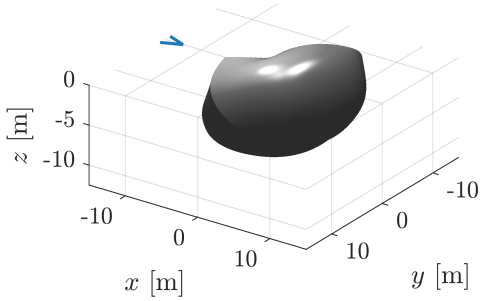

(c) DEL=12.941, $\bar{P} = 186.030$ kW

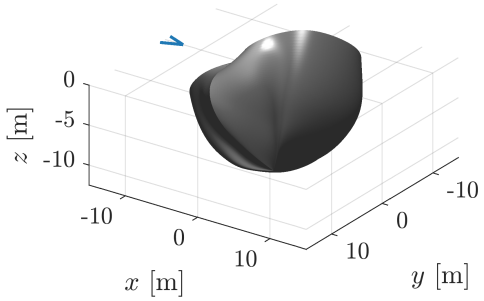

(d) DEL=43.481, $\bar{P} = 304.697$ kW

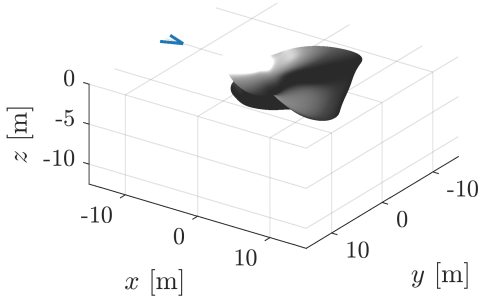

(e) DEL=0.102, $\bar{P} = 41.220$ kW

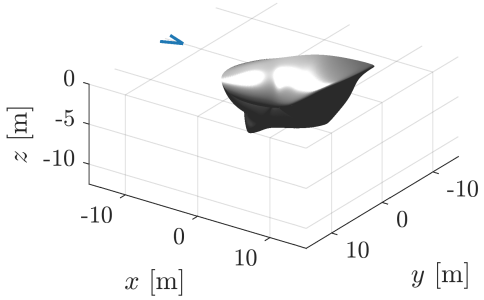

(f) DEL=0.260, $\bar{P} = 68.892$ kW

Figure 3.14: (a), (c) and (e) represent the optimal shapes on the DEL-$\bar{P}$-Pareto front for a surging device in the North Sea, and (b), (d) and (f) represent the optimal shapes for a surging device off the coast of Norway. (a) and (b), and (e) and (f) represent the respective Pareto front limits, and (b) and (c) represent an optimal geometry in the central area of each Pareto front.

3.5 Conclusions

In this study, I explore the relationship between WEC floater hull geometry and PTO reliability. First, I analyse twelve fixed-geometry cases, across two locations (North Sea and Norway), two modes of motion (heave and surge), and three shapes (barge, cylinder, and sphere). Based on these conditions, I measure the damage equivalent load (DEL) on the rod weld connecting the floater to the PTO. Following these fixed geometries, I envelop the fatigue analysis and power calculation methods established for the fixed-geometry cases in a Genetic Algorithm to optimize variable WEC hull geometries for power production and DELs.

Results indicate a clear dependence of DELs on location, oscillation direction, size, and geometry. In particular, heaving geometries produced more optimal solutions than surging geometries, but heaving geometries were more sensitive to location. In heaving cases, DEL and power objectives were relatively equally dominant, whereas surging cases reflected dominance of the power objective. Therefore, it is critical to consider all these parameters in the early design of WECs.

This study makes the case for incorporating reliability objectives into early design simultaneously with power production and cost, rather than secondary to them. Incorporating reliability in conjunction with power production and cost objectives will enable developers and researchers to design more optimal WECs, advancing the techno-economic feasibility of this technology.

Within a WEC hull geometry optimization process, the aim is to generate shapes that result in the optimal balance of large enough oscillations for power

production while minimising fatigue effects on the hull-PTO connection. For this reason, as found during this study, the inclusion of PTO-stroke constraints in the calculation of the force time series when using this method is not recommended, since it could lead to miss-leading results.

In future work, I plan to expand upon the methods included in this study to use a more detailed PTO model. More importantly, this study will be used as the basis for future reliability-based design optimization work that optimizes WEC floater hull geometry to improve PTO reliability, power production, and cost.

Chapter 4: Fatigue Load Reductions in Offshore Wind Turbine Monopile Foundations in Co-Located Wind-Wave Arrays

4.1 Introduction

As discussed in Chapters 1 and 1.2.1, offshore wind turbines are increasing in size and are being placed father offshore to achieve greater power production capacities. The offshore wind energy industry is achieving cost competitiveness and market maturity in the U.K. and Northern Europe, as well as market growth in emerging markets like the U.S. and China. With this kind of maturity, there is a new opportunity to leverage resources and infrastructure to more efficiently use ocean space and achieve global sustainability goals through co-location.

Previous work has suggested co-location of offshore wind energy with aquaculture, marine conservation areas, hydrogen production, desalination, ocean and meteorological observing, shipping and transportation, coastal defense, and more. The main motivation to co-locate other ocean uses is to alleviate current and future ocean use conflicts while most effectively and sustainably using ocean space [108, 19, 44, 16, 1, 136, 25, 95]. With the already installed electrical and structural infrastructure, as well as the established port infrastructure and capability and the technical expertise of port-side and at-ocean personnel, pairing wave energy conversion with offshore wind energy production could be a viable solution for

multi-use ocean sites.

Offshore wind and wave energy technology co-location could promise synergistic effects. Research suggests combining wind and wave technologies via co-location could have synergistic effects that reduce direct and indirect costs for developments through reducing system balancing costs [39, 40], increasing energy production per unit area, sharing costs in design and operations[24], and improving energy output quality and forecasting [90, 19]. While some synergistic effects have been identified, others have yet to be fully explored.

The current state of the industry lends itself increasingly to co-location opportunities. The design of offshore wind turbines is normally governed by extreme limit states, in which significant load contributions come from aerodynamic loads. But as wind turbines increase in size and are placed farther offshore, hydrodynamic loads have increased contribution and fatigue limit states become more important to consider in structural design. In previous literature, results showed that WECs reduce wave height in their lee [20]. If placed on the periphery of an offshore wind turbine array, this could result in a milder wave climate within the array through a reduction of wave heights [21, 5].

This reduction could affect the wave loads and fatigue damage of offshore wind turbine structural components resulting in cost ramifications for both design of foundation costs and O&M of the array. If fatigue reductions are considered in substructure design, the substructure reliability verification depends on the presence of WECs throughout the entire substructure design lifetime. With the current lower maturity level of wave energy compared to offshore wind energy, developers

might be reluctant to accept this prerequisite. However, due to large uncertainties taken into account in design, it will typically be possible to verify the substructure reliability during operations using load monitoring, structural health monitoring and inspections instead. If the fatigue load reductions are not exploited in the design, they can instead be exploited to reduce the need for inspections. Optimally, a risk-informed approach for decision making in relation to design and O&M could be applied. Given foundation costs account for 25% to 34% of the total cost of an offshore wind turbine [12], and O&M can account for up to 30% of the cost of energy [83], decreasing the fatigue loads of the offshore wind turbine support structure could significantly reduce the cost of energy and establish offshore wind energy and wave energy as a more competitive renewable energy source.

In this study, the effects of peripherally-distributing WECs seaward of an offshore wind turbine on the fatigue of the offshore wind turbine monopile support structure is investigated. Representative environmental conditions and device-specific transmission and reflection coefficients are used as in SWAN to quantify the relative wave height reductions from WECs. These relative wave height reductions are then used to evaluate the offshore wind turbine response using HAWC2. Using a case study with the DTU 10MW reference turbine supported by a monopile, and the overtopping WEC, WaveCat, at 30-meter water depths in the central North Sea, the fatigue damage for a co-located wind-wave system is compared to those of an offshore wind turbine-only system. These results are one of the first to begin quantifying the effects of co-location on fatigue in offshore wind turbine support structures, and will enable stakeholders to begin assessing the value of co-located

systems.

This study is divided into three sections. First, the methodology is described, which 1) defines the case study and environmental conditions, 2) quantifies the sea state modifications due to co-location, and 3) evaluates the structural response of the offshore wind turbine. The resulting sea state reduction and fatigue damage are then presented and discussed. Finally, a conclusion of the impact and limitations of the study is included.

4.2 Methods

This section describes the methods used to investigate the effect of co-location on fatigue load reduction in offshore wind turbines. The methods include four subsections as illustrated in Figure 4.1, and include 1) defining the case study area and wave conditions, 2) modeling the sea states in SWAN to quantify the modifications in wave height and period, 3) performing a structural dynamic analysis using HAWC2 to simulate the offshore wind turbine response to the environmental conditions, and 4) evaluating the fatigue damage for offshore wind turbines.

4.2.1 Study Area and Wave Conditions

The case study location is chosen to be the central North Sea, as described in Chapter 3 in Tables 3.2 and 3.1 and Figure 3.2. This site was chosen due to the large number of offshore wind energy installations in the region (and therefore

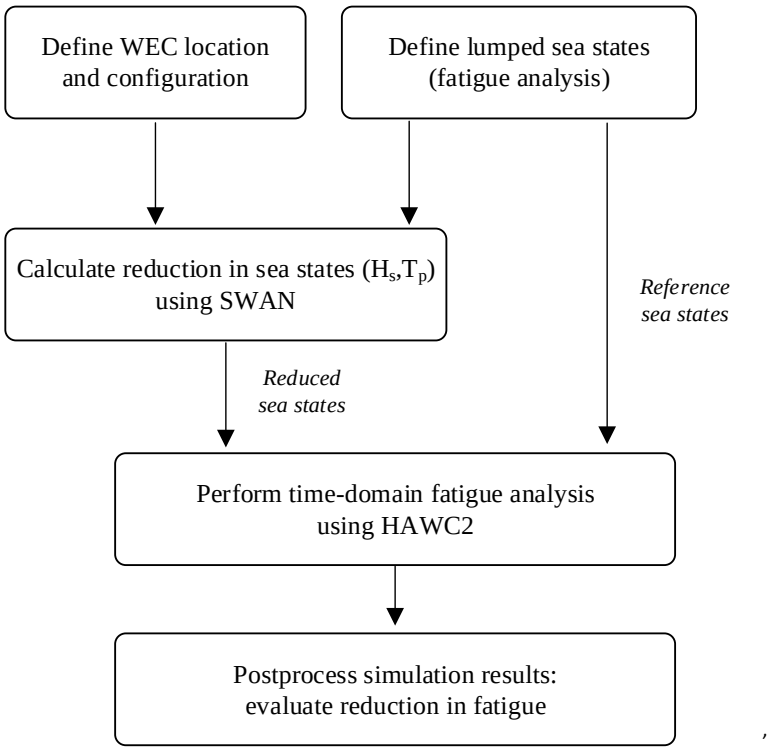

Figure 4.1: Workflow for fatigue analysis of a WEC-offshore wind turbine co-located array

the ideal infrastructure to host a co-located array) and availability of long-term description of the metocean environment [69].

4.2.2 Sea State Reduction Quantification

In this study, a nested grid approach is applied in SWAN to quantify sea state reductions. SWAN is a third-generation wave model which uses the wave action balance equation (using sources and sinks) to estimate wave parameters for wind-

generated surface gravity waves given wind, bottom, and current conditions [114]. This approach has been successfully applied to wave analysis in WEC arrays in previous work [1]. Nesting grids allows SWAN to perform fewer wave propagation calculations in areas outside the area of interest (in the coarse grid), while still maintaining high resolution in the area of interest, where finer mesh sizes and more calculations are required (in the nested grid). Thus, this nested approach decreases computational expense.

In SWAN, obstacles are treated as lines intersecting the computational grid. When calculating the action density flux from one grid point to its neighbors, SWAN first determines if the grid line connects an obstacle line. Only when this is true does SWAN apply the transmission and reflection coefficients to the flux between those nodes. Therefore, the nested grid mesh size is determined by the size of the obstacle, and must be sufficiently small to capture the size of the obstacle. The WEC obstacles was defined in this study as having a defining dimension of 90 m, therefore, the nested grid mesh size should be sufficiently smaller than 90 m.

The coarse grid is defined from 2.50°to 3.50°E and 54.50°to 55.75°N, with a mesh size or grid resolution of 200 m by 200 m, while the nested grid is defined from 3.20°to 3.50°E and 55.00°to 55.25°N with a mesh size of 80 m by 80 m as illustrated in Figure 5.1. The grids are defined using bathymetric data from the European Marine Observation and Data Network [36].

To represent the WECs, transmission and reflection coefficients are implemented in SWAN. This technique has been previously used in representing offshore wind turbines [93, 28] and WECs [1, 17, 121] in SWAN. The WEC chosen

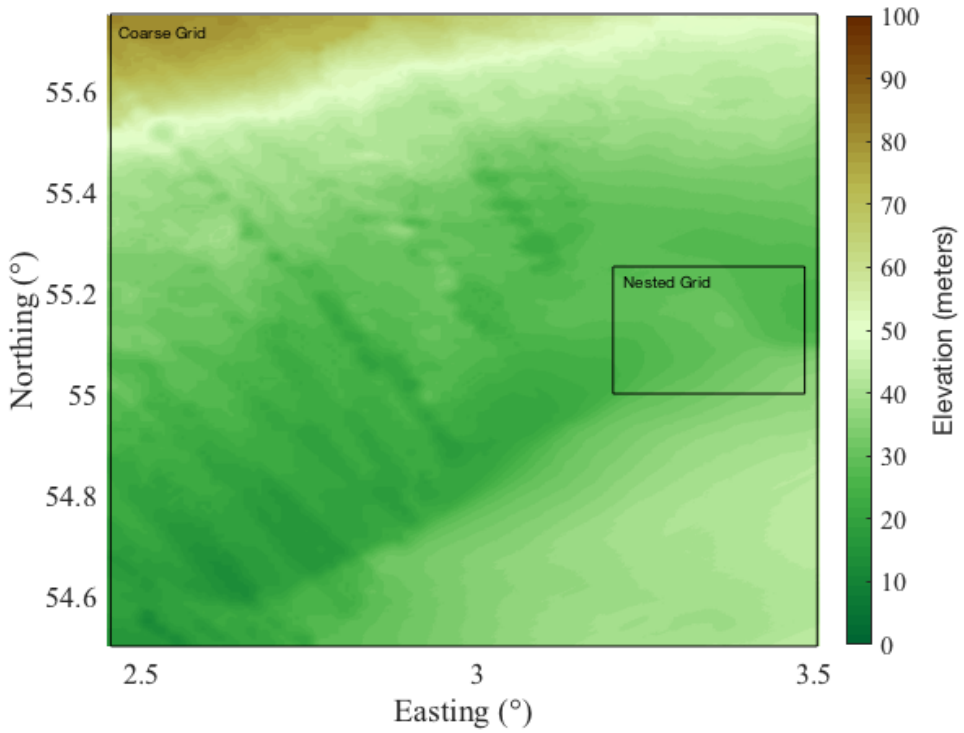

Figure 4.2: SWAN coarse and nested grids

for this study is the WaveCat [38], which is an overtopping WEC (Figure 4.3). This choice was made due to the availability of transmission and reflection coefficients for the WEC. The transmission and reflection coefficients used are 0.80 and 0.45, respectively.

Transmission coefficients range from 0 (all energy is absorbed) to 1 (all energy is transmitted past the obstacle). Reflection coefficients, similarly, can range from 0 (no energy is reflected) to 1 (all energy is reflected). Both transmission and reflection coefficients depend on the characteristics of the waves (H_s, T_p, and direction) and the characteristics of the device (device geometry, power conversion

efficiency, etc.). Therefore, in an ideal scenario, these coefficients would be derived empirically for each set of wave and device characteristics. An empirical study completed by Fernandez et al. [38], defines transmission and reflection coefficients specific to the WaveCat device, but they perform the study on a scaled system, with only four wave cases. These values can not simply be scaled for wave or device characteristics limiting their use in the current study, which considers a wider range of sea state conditions. Despite the shortcomings associated with using these values, these values represent the best information available, thus they have been used in studies comparable to the one at present [5, 6]. The transmission and reflection coefficients used in this study are within the range of the empirical study [38].

In this study, wind turbines were not represented as obstacles, but significant wave height (H_s) and mean absolute wave period (T_{m-10}) were measured at their proposed location. The reduction in H_s and T_{m-10} was calculated by measuring the difference between H_s and T_{m-10} at the wind turbine location with and without the presence of a WEC.

Four different co-located array layouts are investigated, with varying separation distance between the WECs and the offshore wind turbine, and also the number of WECs. These cases are defined in Table 4.1 and illustrated in Figure 4.4 and Figure 5.2. Cases 1, 2, and 4 are single WEC systems with varying separation distances. Case 4 has the maximum separation distance of seven times the offshore wind turbine rotor diameter ($7D_{OWT}$). This distance comes from previous literature detailing the layout of Horns Rev, but for wind turbines with a rotor

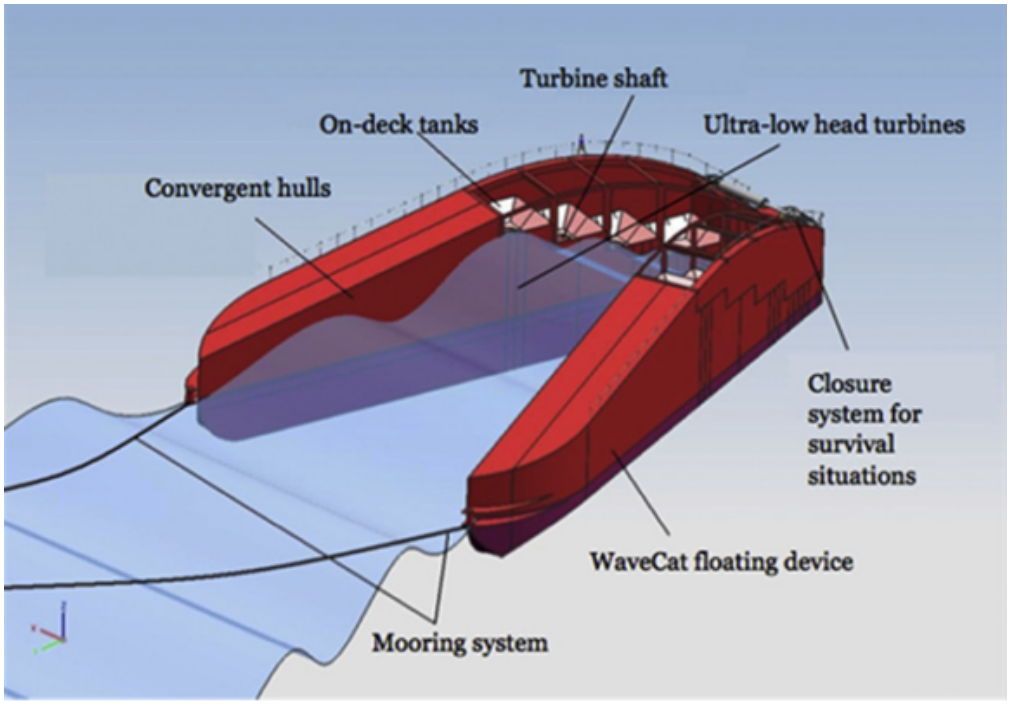

Figure 4.3: A schematic of the WaveCat device (designed and analyzed by Fernandez et al. [38]

diameter (D_{OWT}) of 80 m [82]. Case 1 decreases this separation distance closer to the absolute value of the minimum separation distance at Horns Rev, with a separation distance of 4 times the offshore wind turbine rotor diameter $4D_{OWT}$. Case 2 decreases the separation distance even further to the minimum separation distance required by the WaveCat, 2.2 times the distance between the twin bows of the WEC ($2.2D_{WEC}$) [5], which is 90 m. Case 3 is a staggered WEC array with $2.2D_{WEC}$ as the separation distance between the WECs, and $4D_{OWT}$ as the separation distance between the WEC array and offshore wind turbine. The offshore wind turbine is always placed leeward of the WEC. This is to investigate the

Table 4.1: Co-Located Array Cases

Case	WECs (#)	Separation	Separation Distance (m)
0	0	$4D_{OWT}$	720
1	1	$4D_{OWT}$	720
2	1	$2.2D_{WEC}$	396
3	5	$4D_{OWT}$	720
4	1	$7D_{OWT}$	1260

effects of co-location in a uni-directional wave case.

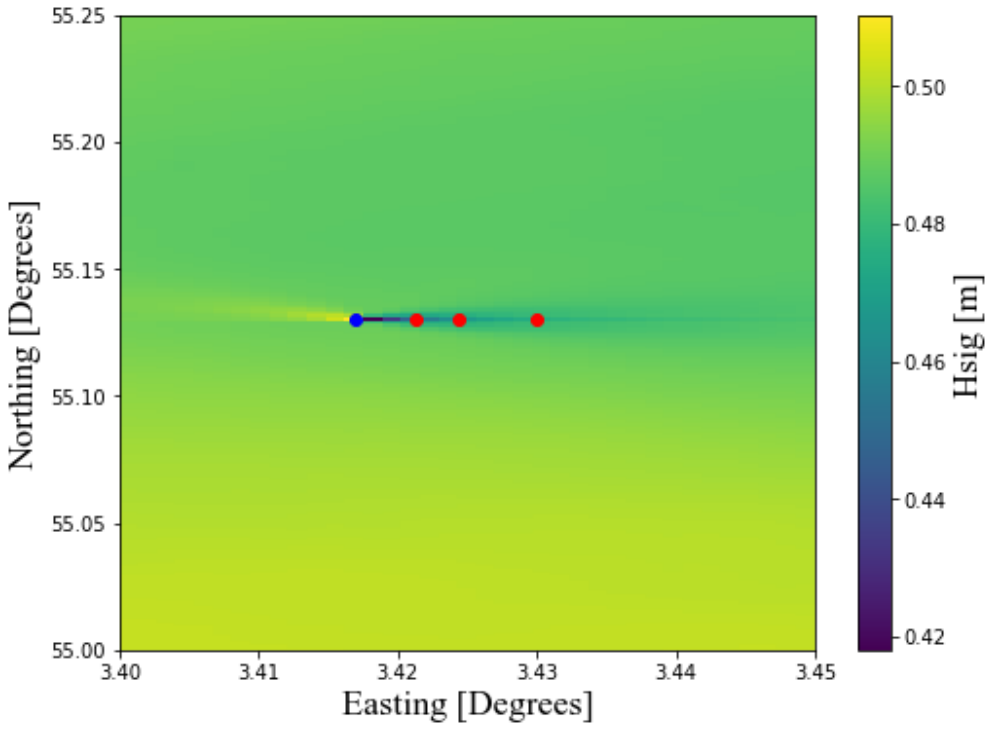

Figure 4.4: Cases 1, 2, 4: Varying separation distances (WEC location in blue, offshore wind turbine locations in red)

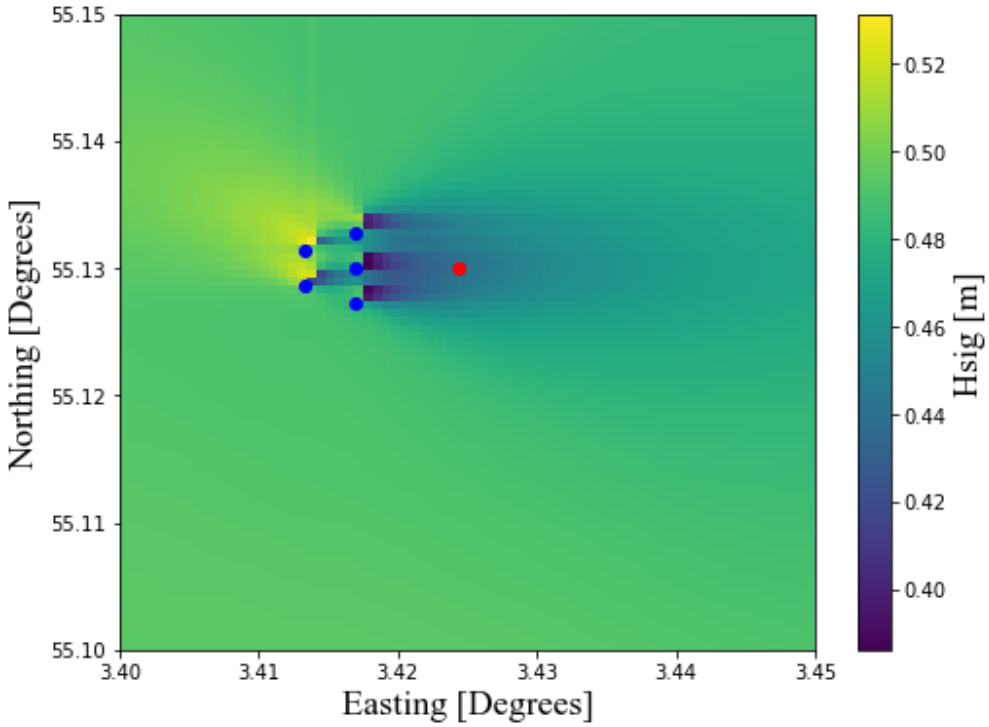

Figure 4.5: Case 3: Varying number of WECs (WEC locations in blue, offshore wind turbine location in red)

4.2.3 Offshore Wind Turbine Modeling

The DTU 10 MW reference wind turbine [9] is selected in performing the fatigue analysis. The main wind turbine and support structure design parameters are summarized in Table 4.2. The foundation design, which was evaluated against ultimate limit states and fatigue limit states at a water depth of 30 m, is taken from a numerical study [122, 124] with soil P-Y curves derived from the finite element tool, Plaxis 3D [14]. P-Y curves represent soil resistance, where P is the soil pressure per unit length of a pile and Y is the pile deflection, at a given soil

depth and type.

HAWC2 [68], an aero-hydro-servo-elastic modeling tool developed at DTU for both static and dynamic analyses of horizontal axis wind turbines, is used to model the DTU 10 MW reference wind turbine supported by a monopile foundation as shown in Figure 4.6. Each component of the structure is modeled as a multibody, where each body represented by Timoshenko beam elements. Both the tower and monopile are modeled as linear elastic material with Young's modulus E_s = 210 GPa and shear modulus G_s = 80.8 GPa. The nacelle and transition piece masses are modeled as concentrated loads at the hub height and foundation-tower interface, respectively. The soil-structure interaction is modeled using nonlinear P-Y curves at every 2.50 m along the embedment depth as illustrated in Figure 4.7. An overall damping of 1.0% is assumed for the offshore wind turbine.

The wind fields (32 x 32 x 8192 points) are generated using the Mann turbulence model [71] implemented in HAWC2. A power law wind profile is assumed with shear exponent, $\alpha = 0.15$. For the hydrodynamic waves, JONSWAP spectrum with peak enhancement factor, $\lambda = 3.3$ is used to generate linear irregular waves. Wheeler stretching is applied on the wave kinematics. Lastly, Morison's equation is used to calculate the loads with drag and inertia coefficients assumed as $C_D = 0.90$ and $C_M = 2.0$, respectively. More information about the offshore wind turbine modeling can be found in Ref. [124, 122].

Table 4.2: Main Design Parameters for the DTU 10MW reference wind turbine and monopile foundation

Parameter	**Value**
Rotor orientation, conFigure	Upwind, 3 blades
Control	Variable speed
Drivetrain	Multiple stage gearbox
Rotor, Hub diameter	178.3 m, 5.6 m
Hub height	119 m
Rated U_w	11.4 m/s
Cut-in, Cut-out U_w	4 m/s, 25 m/s
Cut-in, Rated rotor speed	6 RPM, 9.6 RPM
Rated tip speed	90 m/s
Overhang, Shaft tilt, Pre-cone	7.07 m, 5°, 2.5°
Tower height	115.6 m
Tower dia. at upper, lower end	6.25 m, 9.0 m
Pile dia., embedment depth	9.0 m, 45.0 m

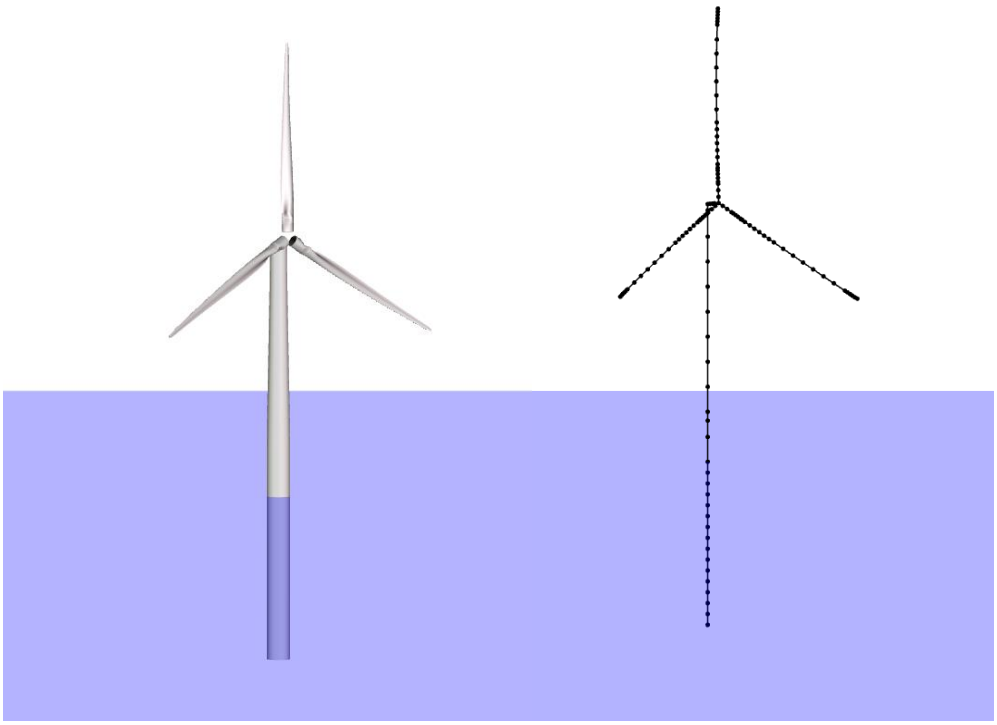

(a) Surface model (b) Beam elements

Figure 4.6: Offshore wind turbine model in HAWC2

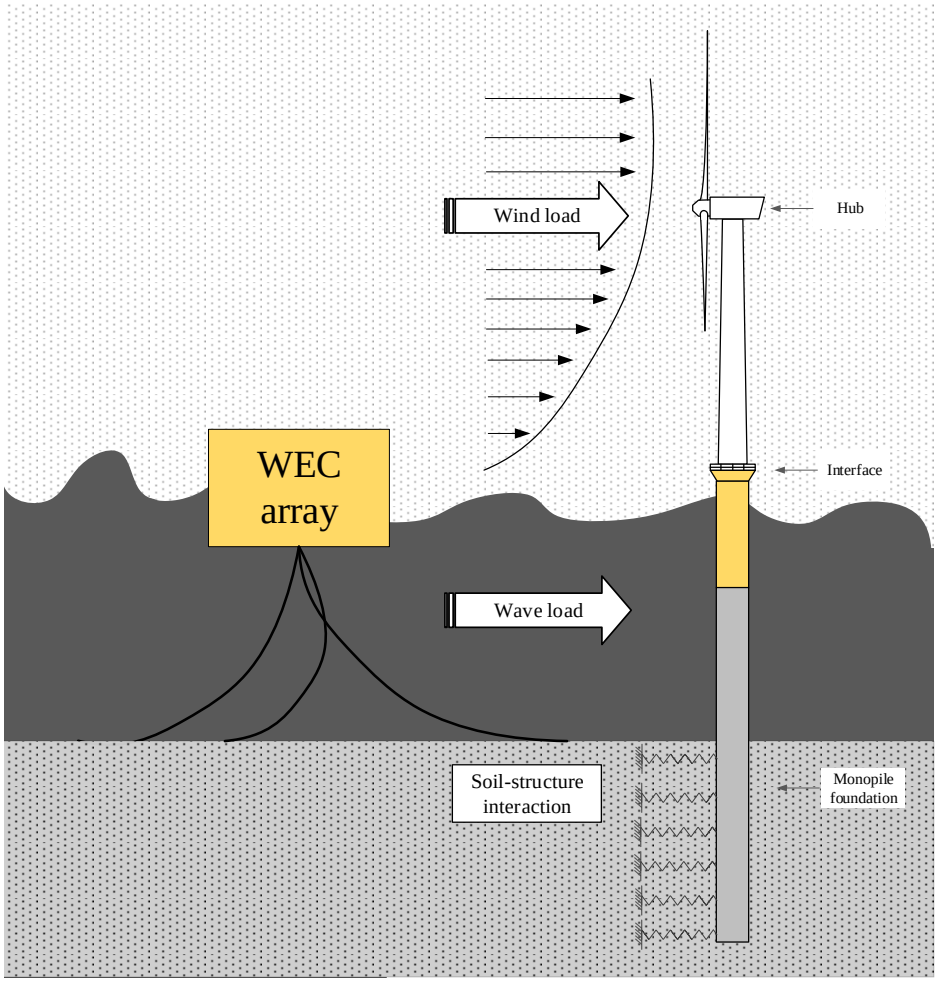

Figure 4.7: Co-located array load schematic

4.2.4 Fatigue Damage Assessment

The fatigue analysis focuses on fatigue during operational conditions, and is based on the design load case (DLC 1.2) of the IEC (International Electrotechnical Commission) design requirements for offshore wind turbines [27]. It is assumed that

the waves are long-crested and come from the west. For each representative sea state summarized in Table 3.2, fatigue simulations are performed in HAWC2 for ten minutes with six seeds each, based on relevant industry design standards [55]. The statistical uncertainties related to simulation duration and number of seeds are not considered. Given one reference case (Case 0) and three test cases with different WEC configurations (Cases 1, 2 & 3) results to a total of 648 simulations. Case 4 was not included in the fatigue load assessment because the wave height reduction was negligible. For simplicity, fatigue damage at the mudline section is evaluated, adjacent to the point of greatest fatigue damage, which occurs just below mudline (Figure 4.8) [123].

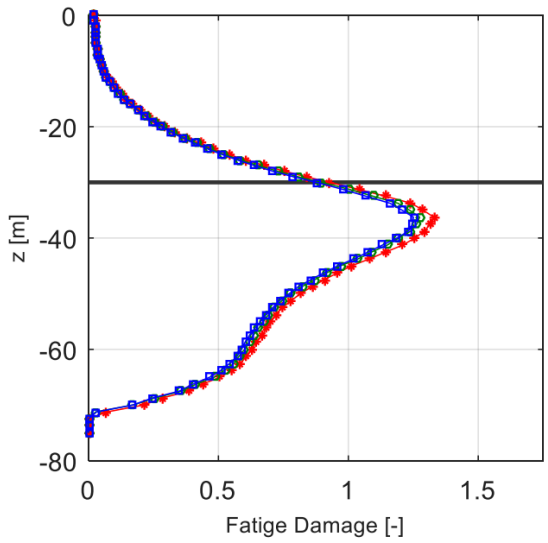

Figure 4.8: The point of maximum fatigue on the monopile at 30 m water depths occurs just below mudline [123]. The multiple colored lines represent monopile designs for the DTU 10MW reference wind turbine, and the black line represents the mudline.

Figure 4.9 illustrates wind and wave modeling, where the wave H_s and T_p are varied for different cases. To allow direct comparison, the same wind fields and wave seed numbers are used.

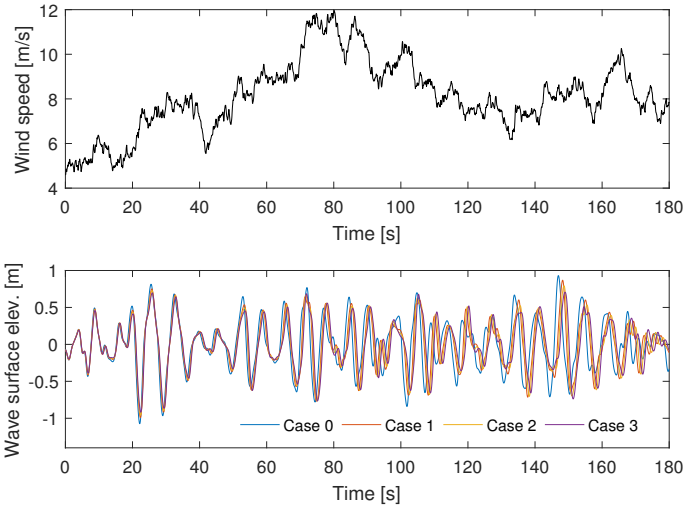

Figure 4.9: Wind and wave modeling (Sea State 6)

The fatigue damage is quantified in terms of damage equivalent load (DEL) as defined in Equation 4.1:

$$DEL = \left[\frac{\sum_{i=1}^{N_{total}} n_i A_i^m p}{n_{eq}} \right]^{1/m} \tag{4.1}$$

where N_{total} is the total number of cycles for each load time histories, n_i is the number of cycle for the load magnitude A_i, p is the probability of occurrence of each sea state, n_{eq} is the reference number of cycles assumed as $n_{eq} = 2.0 * 10^8$, and m is the inverse slope of the S-N curve taken as $m = 4$. This m value is the average characteristic value for steel in seawater with cathodic protection for 110

mm and 125 mm pile wall thickness. Again, more information about the fatigue damage assessment can be found in Reference [124, 122].

4.3 Results and Discussion

Based on the described methods of quantifying wave height reduction, simulating offshore wind turbine response, and calculating fatigue damage, results show that co-location of WECs and offshore wind turbines does reduce fatigue damage in offshore wind turbine support structures when the separation distance between the two devices is sufficiently small. The following sections will detail the sea state reduction quantification, as well as how that reduction affects fatigue in different array cases.

4.3.1 Wave Height Reduction Modeling with SWAN

Using wave height and wave period as indicators for sea state modification, the reductions in wave height are calculated and summarized in Figure 4.10. A negligible change in wave period was observed, so those results are not included.

The greatest change was in H_s, which experienced greater reductions as the number of WECs increased and the separation distance decreased. Figure 4.11 shows the variation in wave height reductions (sampling among sea states) across the different cases and not accounting for the probability of occurrence. The greatest reduction in wave height was in Case 3, comprised of a 5-WEC array.

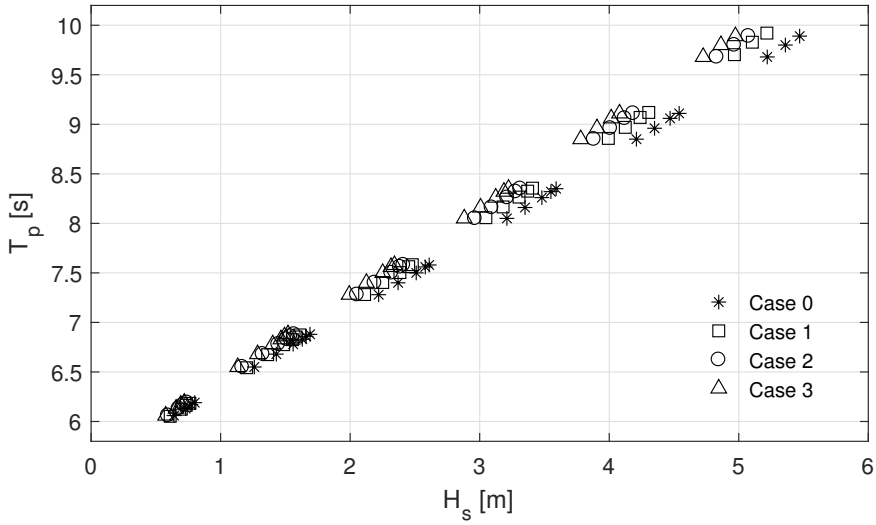

Figure 4.10: Reduced sea states for cases

Case 2 had the second largest wave height reduction, with a separation distance of $2.2D_{WEC}$, followed by Case 1 with a separation distance of $4D_{OWT}$. The variation in wave height reduction is greatest for Case 3, followed by Case 1, then Case 2. Case 4, with a separation distance of $7D_{OWT}$, had the lowest wave height reduction. Because the wave height reduction was negligible, fatigue damage assessment was not completed for this case. Thus, the study proceeded with Cases 0-3.

The result showing the largest decrease in wave height from an array and minimum separations distances indicates that, to maximize fatigue reduction benefits, developers of co-located arrays should minimize the separation distance between the WECs and offshore wind turbines, as well as implement WECs on an array scale. Furthermore, as can be seen from Figures 4.4 and 5.2, the shape and size of the "shadow effect" area in the WEC's lee is different between a single WEC and

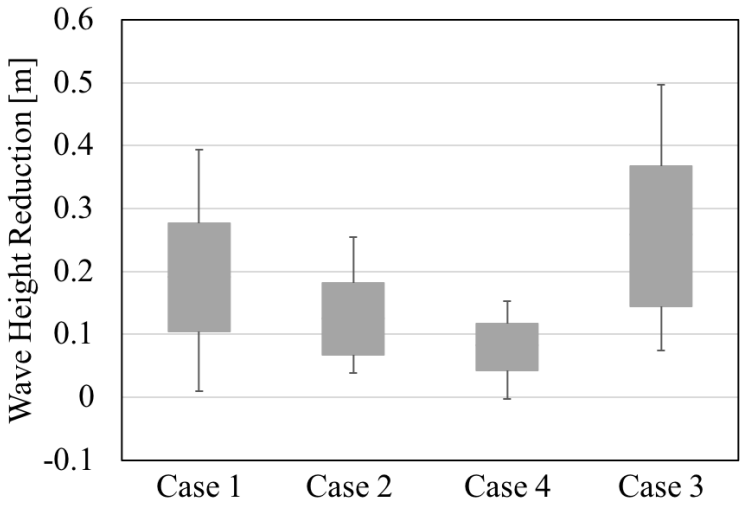

Figure 4.11: H_s reduction for each case

a WEC array and depends on the WEC array layout (the number and placement of the WECs seaward of an offshore wind turbine array). The number of devices increases the area and widens the geometry of the shadowed area, while the overlap of individual WEC shadows changes the magnitude of the wave height reduction. Although this study considers a single-offshore wind turbine system, the layout of a WEC array in front of a larger offshore wind turbine array will be important in determining how many offshore wind turbines in the array will benefit from co-location, and the extent to which they will benefit.

In the present study, the WEC is placed seaward of the offshore wind turbine in each case. This was dictated by the need to start investigating the effect of co-location in a unidirectional wave case. In a more realistic wave case, the waves would be multidirectional, vary with season, and be misaligned with the wind direction. The portion of the time that the offshore wind turbine would be directly

in the WEC's shadow would change depending on the wave direction and layout of the WEC array. The decrease in time that wave heights are reduced would result in a decrease in time that fatigue loads are reduced under the case that the WEC array is located only on one side of the offshore wind turbine array. In the case that the WECs are located on multiple sides of the offshore wind turbine array, the shadow effect could be maintained, at least for more wave directions.

Misalignment between incoming wind and wave directions would also change the results of this study. In this study, only co-directional wind-wave cases are considered. Under the same WEC array layout as considered in this study, if wind came from a different direction than the waves, the WEC would still reduce wave height around the offshore wind turbines, but the fatigue on the offshore wind turbine monopile would decrease from aerodynamic damping. In future work, multidirectional waves, seasonality of wave conditions, and their affect on fatigue load reductions should be considered.

For each sea state, an almost constant reduction in H_s can be observed as shown in Figure 4.12. The minor decrease at the three highest sea states is explained by the relative size of the waves compared to the size of the WEC. While the smaller sea states are affected by the WEC and thus produce a shadow of diffracted sea states behind the WEC, the sea states with larger significant wave heights and periods surround the WEC and do not exhibit as much diffraction. When diffraction increases, the wave height reduction increases.

It is important to note that using empirically-derived transmission and reflection coefficients that vary with wave conditions and device characteristics would

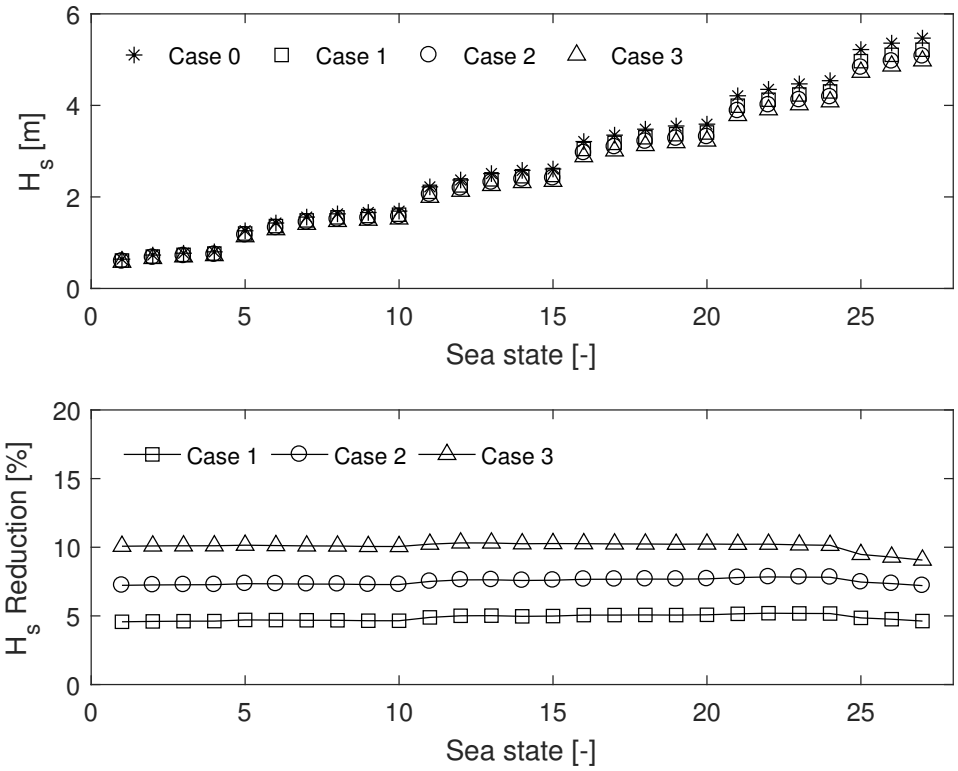

Figure 4.12: Significant wave height reduction

change the significant wave height reduction. WEC performance depends on wave conditions, converting more or less energy at different wave conditions. When the WEC is operating at optimal conditions, the energy conversion, and thus transmission and reflection, would change. There is an opportunity for future work to empirically define transmission coefficients over the characteristic sea states and incorporate them into further analysis of WEC shadowing. Even more promising, however, is alternate ways of modeling WEC interactions with waves that do not rely on fixed and empirically-derived transmission and absorption coefficients.

For instance, Boundary Element Method more accurately details the dynamics of a WEC and its interaction with waves, and there is ongoing work to accurately describe downstream effects. Limiting this work is the computational expense of Boundary Element Method, so research is shifting to developing models which blend the use of Boundary Element Method directly around the device with wave propagation methods like SWAN beyond the device's immediate vicinity. With continued advancement, these codes will become available for use.

4.3.2 Fatigue Analysis

The normalized fatigue damage equivalent load (DEL) at the mudline on the monopile for each sea state is summarized in Figure 4.13. The higher DELs are given by sea states associated with higher wind speeds (refer to Table 3.2), indicating that the wind loads still dominate fatigue during operational conditions. For each case, the damage reduction (in %) is calculated as shown in Figure 4.14. The effective reduction accounts for the occurrence probability of each sea state. This indicates that even though there is higher gross reduction in DEL from higher sea states, the actual DEL reduction comes mostly from sea state 6, which has the highest occurrence probability at the chosen environment.

The total fatigue DEL can be calculated by considering contributions from each individual sea state as shown in Figure 4.15. The total DEL at the mudline section of the monopile foundation is normalized with respect to the reference case (Case 0) value. The results indicate that Case 1 and Case 2 lead to about 8% reduction

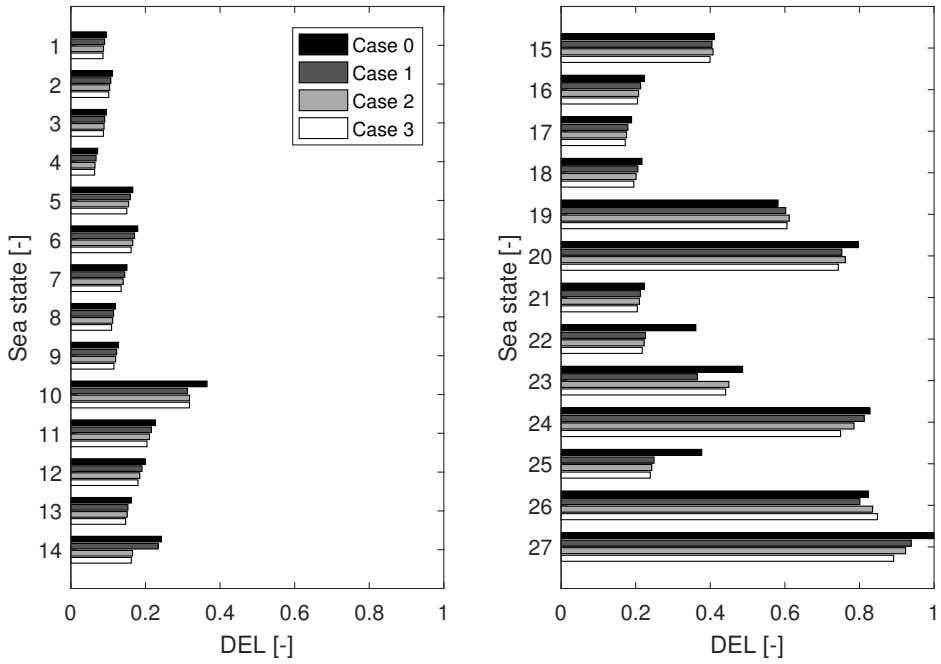

Figure 4.13: Fatigue damage equivalent load (DEL) for each sea state

in fatigue, while Case 3 leads to a fatigue reduction of about 10%.

While this fatigue analysis covers the design load case for the DTU 10 MW reference wind turbine monopile under operational conditions, it is expected that greater fatigue damage reductions can be observed during parked or idling conditions, where wave loads dominate the response of the offshore wind turbine structure. Further studies can be performed to investigate relevant cases such as wind-wave misalignment, extreme load cases, and other WEC and offshore wind turbine designs.

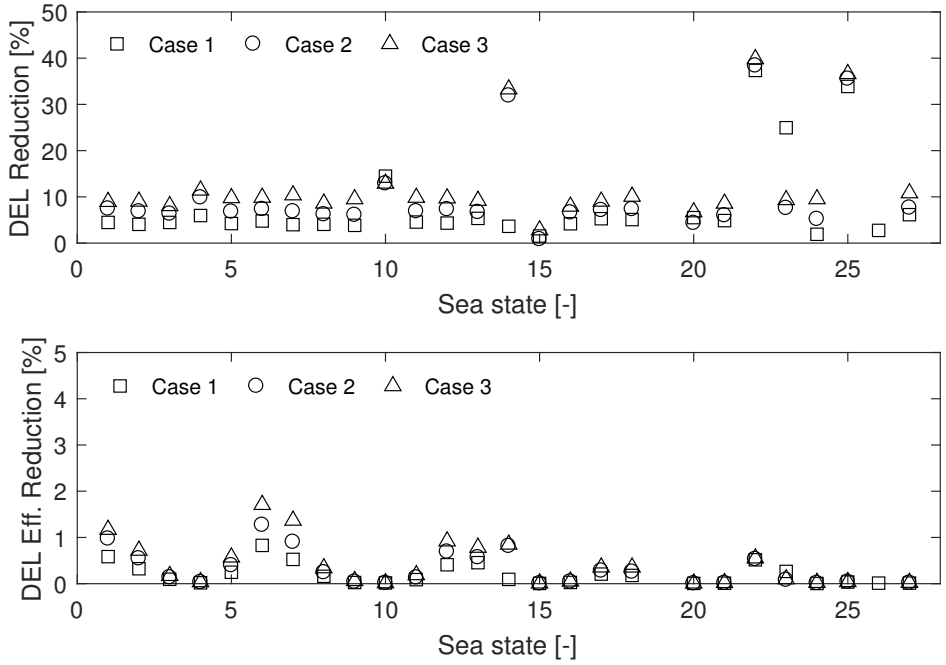

Figure 4.14: DEL reduction and effective reduction (accounts for occurrence probability)

4.4 Conclusions

In this study, the effect of WEC-offshore wind turbine co-location on offshore wind turbine monopile fatigue is investigated. Four different cases were investigated with varying WEC-offshore wind turbine separation distance and WEC array size. The reduction in sea states are quantified using a nested grid approach in SWAN. A fully-coupled model in HAWC2 is used to simulate the offshore wind turbine response and perform the fatigue analysis.

Results indicate that placing a WEC system (either a single WEC or WEC

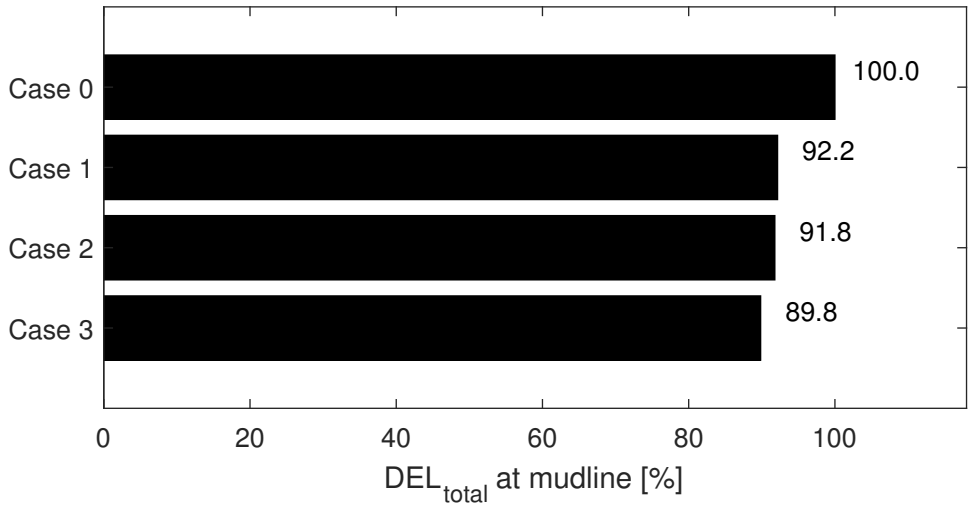

Figure 4.15: Total reduction in fatigue DEL

array) as defined by Cases 1, 2 and 3 results in H_s reductions of 5%, 7.5% and 10%, respectively. These wave height reductions lead to an 8-10% decrease in fatigue DEL at the mudline section of the monopile. These results indicate structural benefits to offshore wind turbine support structures from co-location, and can be used as basis for concept assessment.

Opportunities for future work include the inclusion of more complex wave and wind cases, enhanced WEC modeling, and varying array sizes. First, including multi-directional, seasonally-dependent, and misaligned wave cases will give a better understanding of how these co-located arrays behave under more realistic environmental conditions. Second, the use of custom transmission and reflection coefficients will allow for greater certainty about device performance given specific environmental and device characteristics. Finally, varying WEC array size and

placement around a more realistic, larger offshore wind turbine array will provide insight about how to best use co-location in commercial scenarios.

Chapter 5: Effects of Co-Located Floating Wind-Wave Systems on Fatigue Damage of Floating Offshore Wind Turbine Mooring Cables

5.1 Introduction

The cost of floating wind technology currently limits technology implementation, despite its necessary development. Levelized cost of energy estimates exceed \$0.20/kWh [78], which is nearly 1.5 times the cost of fixed-bottom offshore wind, twice as expensive as solar photovoltaic cells, and 4 times more expensive than hydropower [57]. Despite its economic impracticability, to realize offshore wind energy technology's full potential, floating systems are required. For instance, 60% of the U.S. offshore wind energy resource exists at depths that require floating technology to convert [127]. Industrial realization of floating offshore wind technology requires reductions in the current high levelized cost of energy.

Mooring systems are predicted to contribute 5-10% of total levelized cost of energy of floating offshore wind turbines (FOWT) and remain one of the greatest barriers to their implementation [77]. A significant portion of this cost is expected to come from their O&M, or the cost of scheduled and unscheduled inspection, maintenance, and repair. Because fatigue loading contributes to the degradation of FOWT mooring cables over time, reductions in fatigue loads could lower O&M costs for permanently moored structures via increased cable life and increasing

time between failures or planned maintenance.

Reductions in levelized cost of energy for floating offshore wind technology could be made possible through the co-location of WECs and FOWTs. Combining these technologies in the same leased ocean space through co-located array development is being investigated as a potential opportunity for future offshore renewable energy development, made possible by the continued advancement of FOWT and WEC industries.

As discussed in Chapter 4, research suggests combining wind and wave technologies via co-location could have synergistic effects. Floating offshore wind energy technology, however, has added benefits to fixed-bottomoffshore wind turbines. Offshore wind and wave energy resources are co-located, and increase with distance from shore. Because of the location of these resources, floating offshore wind and wave energy technologies are better suited to serve communities with deep coastal waters and good wave and wind resources than fixed-bottom wind turbines alone. In addition, because of the similarity in floating structure technology, infrastructure and resources (port-side and at-ocean technical personnel and equipment) could be shared.

This study explores how placing WECs seaward of a FOWT could reduce fatigue damage incurred by FOWT mooring cables. Given that fatigue damage is often an important design driver for mooring systems [130], reduced fatigue damage could have ramifications for decisions involving maintenance, lifetime extensions, and re-powering. To quantify the effects of co-location on FOWT mooring cable fatigue damage, I use SWAN to simulate and estimate sea state reductions from

wave transmission and reflection past the WEC array. I then use WEC-Sim [78] and MooDy [88], to model mooring cable behavior. Fatigue analysis with Rainflow Counting and relevant design standards [31, 32] are used to quantify the fatigue loading on the mooring cables and calculate the damage incurred.

This study is divided into four sections. First, I describe the methods I use to measure fatigue damage reductions from co-location. Following this, I summarize the results from implementing these methods in case studies to describe how co-location modifies fatigue damage of FOWT mooring. Lastly, I discuss the impact and limitations of the results.

5.2 Methods

In this section, I describe the methods used to explore the effect of co-location on fatigue load reduction in FOWT mooring cables. These methods include 1) defining the case study area and wave conditions, 2) modeling the sea states in SWAN to produce wave spectra at the FOWT location 3) performing a time-domain simulation of the mooring cable in WEC-Sim and MooDy [88], and 4) post-processing the response simulation results with Rainflow Counting to calculate the fatigue loading on the FOWT mooring cable.

5.2.1 Study Area and Wave Conditions

I chose the location of the case study to be off the southwestern coast of Norway [108] (Figure 3.2). The methods for modeling these sea states and the resulting data is included in Chapter 3, in Tables 3.1 and 3.3, as well as in Figure 3.2. This site was chosen for its suitability for floating offshore wind and wave energy technology based on identified water depths and wind and wave resources.

5.2.2 Modified Wave Spectra Generation

In this study, I applied SWAN using a nested grid approach, as in Chapter 4. I defined the coarse grid to be from 3.0°to 4.5°E and 61°to 62.8°N, with a mesh size or grid resolution of 200 m by 200 m. I defined the nested grid from 4.0°to 4.40°E and 61.5°to 62°N with a mesh size of 80 m by 80 m (Figure 5.1). I sourced the bathymetric data for these grids from the European Marine Observation and Data Network [36].

To represent the WECs, I implemented transmission and reflection coefficients for the WaveCat overtopping device in SWAN using the same methods as in Chapter 4.

A total of nine cases were tested to understand the relationship between separation distance and WEC array size on FOWT mooring chain fatigue. These cases are summarized in Table 5.1.

The cases consist of three WEC array sizes: a single WEC array, a five-WEC array, and an eleven-WEC array. For each of these WEC array sizes, the FOWT

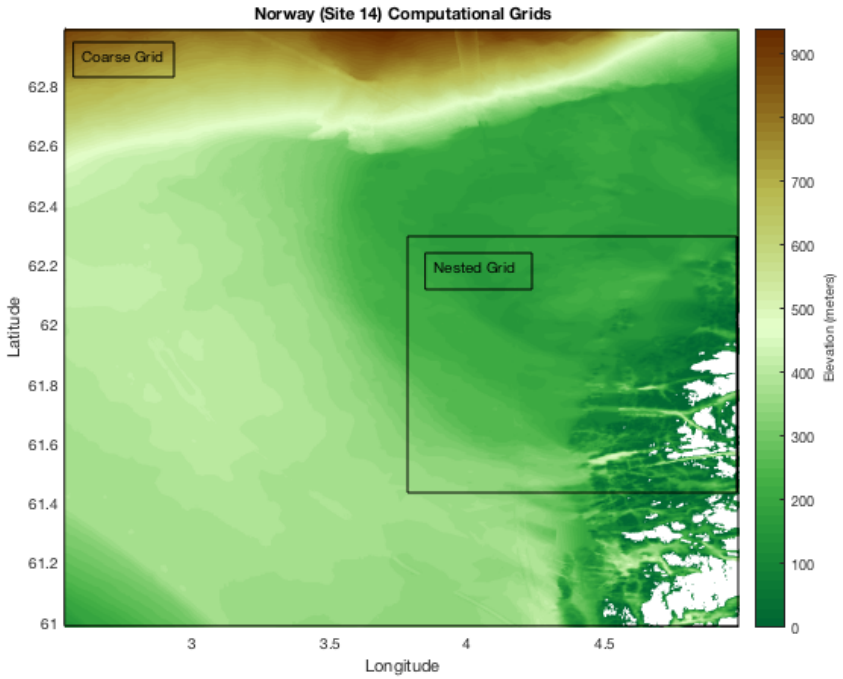

Figure 5.1: SWAN course and nested grids

is separated by $2.2D_{WEC}$, $4D_{FOWT}$, then $7D_{FOWT}$. The FOWT rotor diameter is 120m, and the WEC characteristic length is 90m. These array layouts are visualized in Figure 5.2.

Table 5.1: FOWT-WEC Co-Located Array Cases

Case	WECs (#)	Separation	Separation Distance (m)
0 (Baseline)	0	n/a	n/a
1	1	$2.2D_{WEC}$	198
2	1	$4D_{FOWT}$	480
3	1	$7D_{FOWT}$	840
4	5	$2.2D_{WEC}$	198
5	5	$4D_{FOWT}$	480
6	5	$7D_{FOWT}$	840
7	11	$2.2D_{WEC}$	198
8	11	$4D_{FOWT}$	480
9	11	$7D_{FOWT}$	840

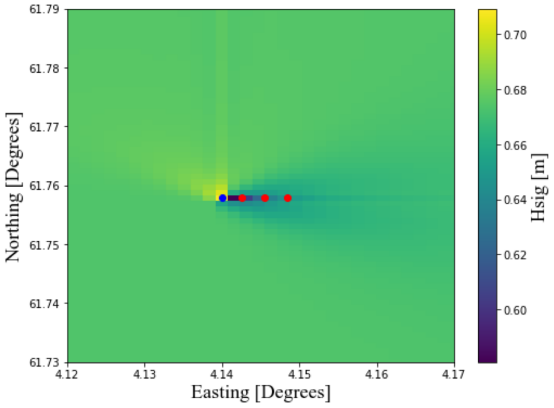

(a) A single WEC

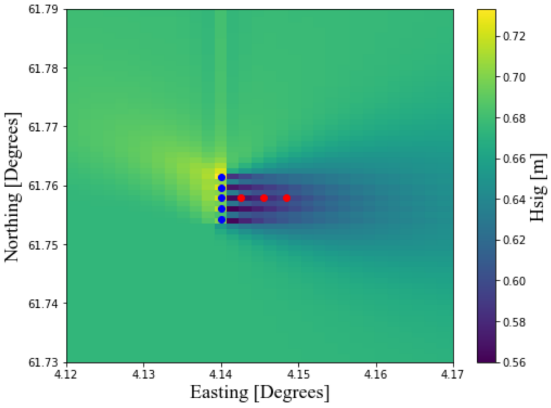

(b) A five-WEC array

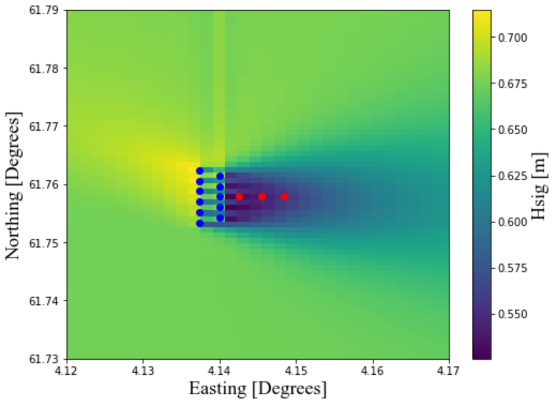

(c) An eleven-WEC array

Figure 5.2: Nine tested array layouts (WEC locations are in blue and FOWT locations are in red)

5.2.3 Floating Offshore Wind Turbine Modeling

The FOWT is a semi-submersible platform based on the DeepCwind concept used in the OC4 and OC5 [99, 100] projects (Figures 5.3 and 5.4). The platform has three columns arranged in a triangular array with a fourth central column supporting the tower.

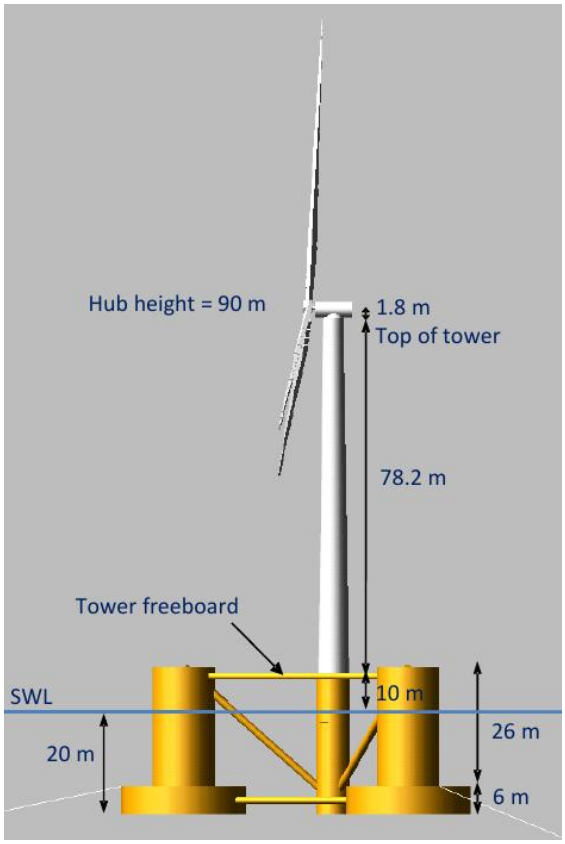

Figure 5.3: Representation of the FOWT used in this study (from [100])

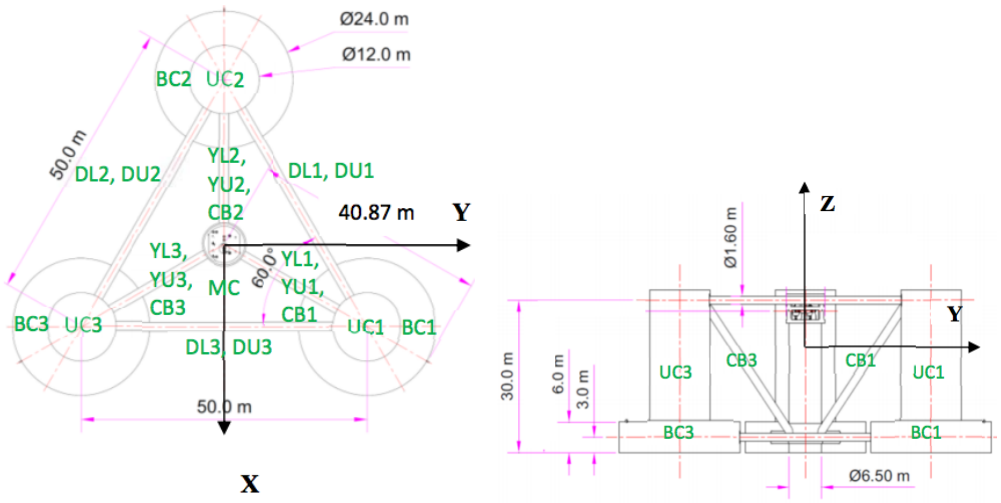

(a) Top view (b) Side view

Figure 5.4: Dimensions of the semi-submersible foundation of the FOWT from the a) top view and b) side view (from [100])

A right-handed local reference system for the FOWT is located at the mean water level, on the axis of the central column, as seen in Figure 5.4. The x-axis points to one of the outer columns, and the z-axis points upwards. When deployed, the x-axis is pointing westward.

The FOWT was modeled in WEC-Sim using the mass and geometry data listed in Table 5.2 and hydrodynamic coefficients computed in WAMIT, provided by NREL [99]. WEC-Sim [79] is a linear radiation and diffraction simulation tool for WECs, developed in MATLAB and Simulink. It uses hydrodynamic coefficients computed by potential flow hydrodynamic codes, such as WAMIT or NEMOH, and does not account for second order drift forces.

By default, to perform simulations of moored devices, WEC-Sim is coupled to the lumped-mass method code for mooring cables, MoorDyn [52]. However,

Table 5.2: Properties of the FOWT, relative to the local platform reference system

Parameter	**Value**
Mass [kg]	1.4265×10^7
Roll inertia[kg m^2]	1.3947×10^{10}
Pitch inertia [kg m^2]	1.5552×10^{10}
Yaw inertia [kg m^2]	1.3692×10^{10}
Displacement [m^3]	1.3917×10^4
Centre of gravity [m]	-8.07
Centre of buoyancy [m]	-13.18

in this study, I coupled WEC-Sim [78] and MooDy [88]. I chose to use MooDy because it is a higher order discontinuous Galerkin mooring cable solver using elemental expansion basis of arbitrary order p. It is especially suited to capture snap loads and is able to provide highly accurate solutions with few degrees-of-freedom. This means that it requires less computational effort than first order codes to obtain solutions with similar accuracy, as shown in [76]. The theory describing the coupling of MooDy to external solvers for floating body dynamics is described in [87].

No data is presented for the specific characteristics of the wind turbine (such as blade design), because the scope of this study focuses on the wave loads on the FOWT mooring that were modified by the presence of a WEC. In this analysis, I assumed that the presence of the WEC did not significantly affect the wind loads experienced by the wind turbine.

The FOWT is moored using three chain catenaries, with an angular spacing of 120° between them, (Figure 5.5). The cables connect to the semi-submersible

platform at the fairleads, placed at each of the outer columns 14 m below the static water level.

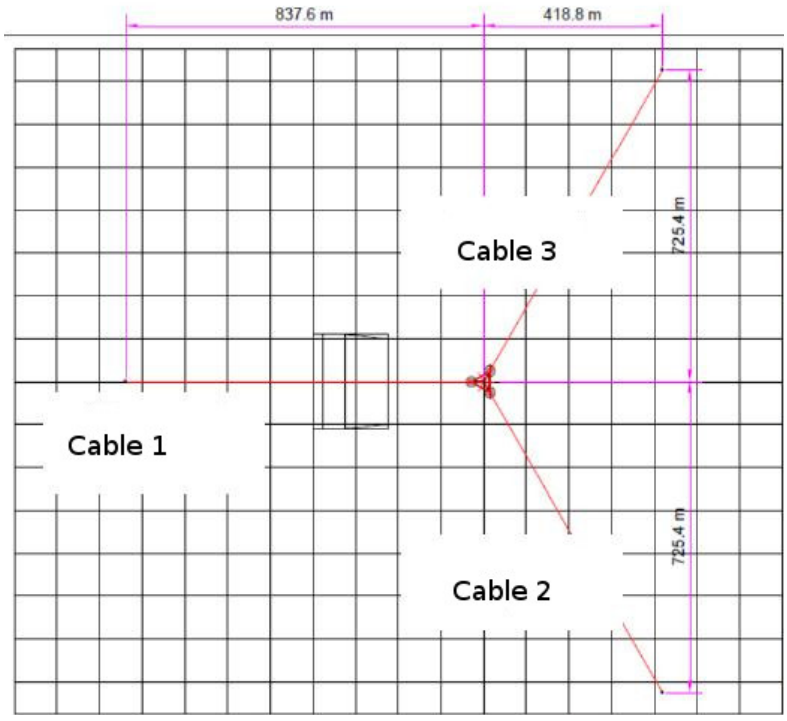

Figure 5.5: Layout of the mooring system (adapted from [100])

In Tables 5.3 and 5.4, I present the characteristics of the mooring cables and of the mooring system, respectively, as outlined by [99]. The equivalent line diameter listed in Table 5.3 is the diameter of a uniform circular cable made of the same material, and having the same mass and submerged weight per unit length as the chain. It is a parameter used by MooDy and other mooring codes to estimate the hydrodynamic forces acting on mooring chains. Each mooring cable was modeled in MooDy using ten elements with a polynomial order of $p = 5$. In the coupled WEC-Sim-MooDy simulations of the moored FOWT, each sea state was simulated

Table 5.3: Properties of the mooring chain.

Parameter	**Value**
Link diameter [m]	0.0766
Equivalent line diameter [m]	0.1427
EA (Young's Modulus $\times$ Area) [N]	753.6×10^6
Mass per unit length [$\mathrm{kg\,m^{-1}}$]	113.35
Submerged weight per unit length [$\mathrm{N\,m^{-1}}$]	1065.7
Added mass coefficient	1.0
Hydrodynamic drag coefficient	1.1
Seabed drag coefficient	1.0

Table 5.4: Mooring system properties relative to the platform reference system

Parameter	**Value**
Anchor 1 position [m]	$(837.6; 0.0; -200.0)$
Anchor 2 position [m]	$(418.8; -725.4; -200.0)$
Anchor 3 position [m]	$(418.8; 725.4; -200.0)$
Fairlead 1 position [m]	$(40.9; 0.0; -14.0)$
Fairlead 2 position [m]	$(20.4; -35.4; -14.0)$
Fairlead 3 position [m]	$(20.4; 35.4; -14.0)$
Unstretched cable length [m]	835.5

for a duration of three hours.

In a commercial deployment, the mooring system would be designed for the deployment site. The mooring design used in this study is generalized, as it was in the OC4 project.

5.2.4 Fatigue Damage Calculation

The tension time series at the fairlead is obtained from the coupled simulations of the FOWT and its mooring system subjected to waves. Because the upper end-point of the cables (the fairlead position) is usually the point of maximum tension – and the most susceptible to damage from corrosion and out-of-plane bending – I chose it for fatigue analysis. Therefore, following each of the three mooring cables simulations, the time series of the fairlead for each cable is extracted from the tension time series of ten points along the mooring cable. I analyzed the time series with WAFO's Rainflow Counting algorithm [115] to quantify the stress cycle time series data, discarding the first 800 s of each record due to transient effects in the simulation.

I binned the counted stress cycles by their amplitudes in 20 bins, as suggested by Wægter [126]. I then used Palmgren-Miner's rule to estimate the chain fatigue caused by each binned stress range for each sea state. That is, for each bin, I divide the number of cycles in that bin by the number of cycles to failure for the given stress range as outlined in DNV-OS-E301 Standard for Offshore Position Mooring [31]. The cycles to failure, or the component capacity against tension fatigue, is determined by Equation 5.1 from [31].

$$n_c(s) = a_D s^{-m} \tag{5.1}$$

where $n_c(s)$ is the number of stress ranges (or the number of cycles) in a given amplitude, a_D is the intercept parameter of the S-N curve (equal to 6.0×10^{10} for

studless chains (open link)), s is the stress range (double the amplitude) in MPa, and m is the slope of the S-N curve (equal to 3.0 for studless chains (open link)).

The results for each sea state are then multiplied by their probability of occurrence to obtain a measure of the total fatigue damage over the lifetime of the structure. In the calculation of the fatigue damage, I assumed a structural lifetime of twenty years.

5.3 Results and Discussion

In this section, results are divided into two sections. The first section describes the results from a single array case for a single catenary, chronicling how the fatigue reduction varies over sea states and over the lifetime of the mooring chain. The second section then extends the study to investigate how much fatigue changes between catenaries, as well as across multiple array cases. The array cases vary by WEC array size and the separation distance between the WEC array and the FOWT.

5.3.1 Single Array Results

In this section, I focus on the results for Cable 1 because it experiences the highest fatigue loads of the three catenaries.

Figures 5.6 and 5.7 illustrate the difference in fatigue damage for a FOWT-only system and for a co-located FOWT-WEC system. Figure 5.6 shows the damage

caused on a three-hour period, while 5.7 shows the damage caused by each sea state during the twenty year lifetime of the structure. Because of the large variation in magnitude between fatigue damage at low and high sea states, Figure 5.6 and 5.7 have embedded plots to show sea states 1-14. The percentage of fatigue reduction for each sea state is shown in Figure 5.8.

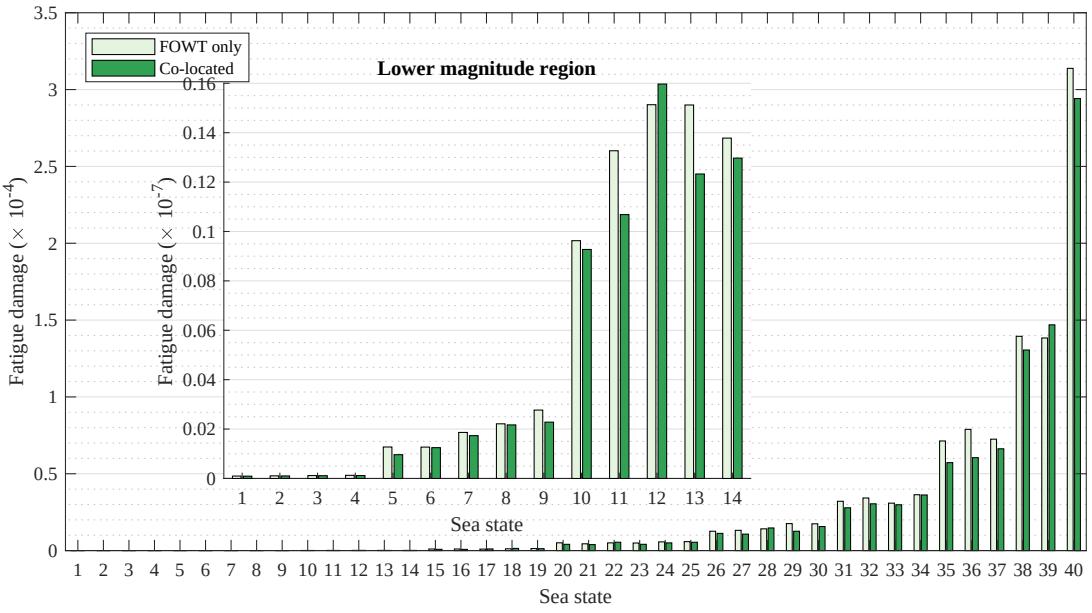

Figure 5.6: Fatigue damage in Cable 1 caused by each sea state on a three-hour period

As can been seen from Figures 5.6- 5.8, in 35 out of 40 simulated sea states, fatigue damage is reduced. In the 5 cases where fatigue increased, it increases by 6% to 22%. The reason for this is not fully understood, and requires further study. Possible reasons for this are attributed to variability in sea state simulations, such as diffraction of waves as they pass the WEC, together with refraction from varying bathymetry. With a replicated, seeded simulations of the same conditions,

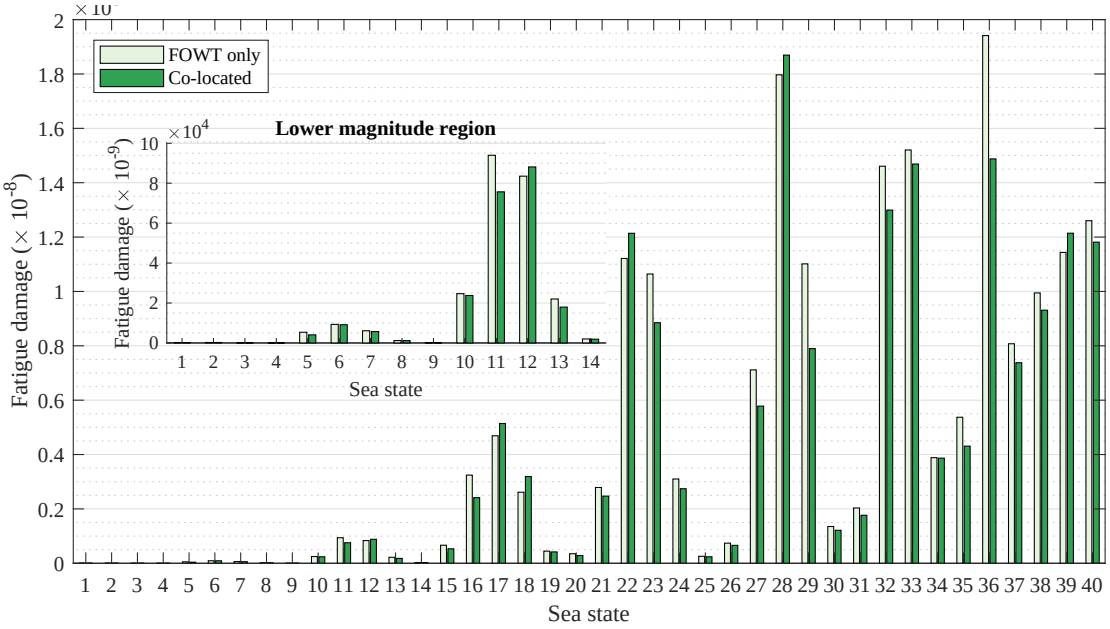

Figure 5.7: Fatigue damage in Cable 1 caused by each sea state over the 20 year lifetime of the FOWT

the variability and uncertainty associated with this fatigue reduction should be able to be quantified.

Figure 5.6 show that, as wave height and period increase (in a three-hour simulated sea state), the fatigue damage in each sea state increases. The value of the fatigue reduction increases as the magnitude of the fatigue damage increases. This trend is not true for Sea States 3, 4, 10, 11, and 30. These sea states show fatigue damage increases. Cumulatively over over the lifetime of the mooring cable and across all sea states, the fatigue damage caused by first order wave loads was reduced, on average, by 8.3%.

Over the lifetime of the structure the total fatigue damage increases with wave height and period. The value of fatigue damage reductions increase as wave height

and period increase (Figure 5.7). Again, this is not true for Sea States 3, 4, 10, 11, and 30, which show fatigue damage increases. The relative percentage of fatigue reduction, however, does not show a trend with increasing wave height and period (Figure 5.8).

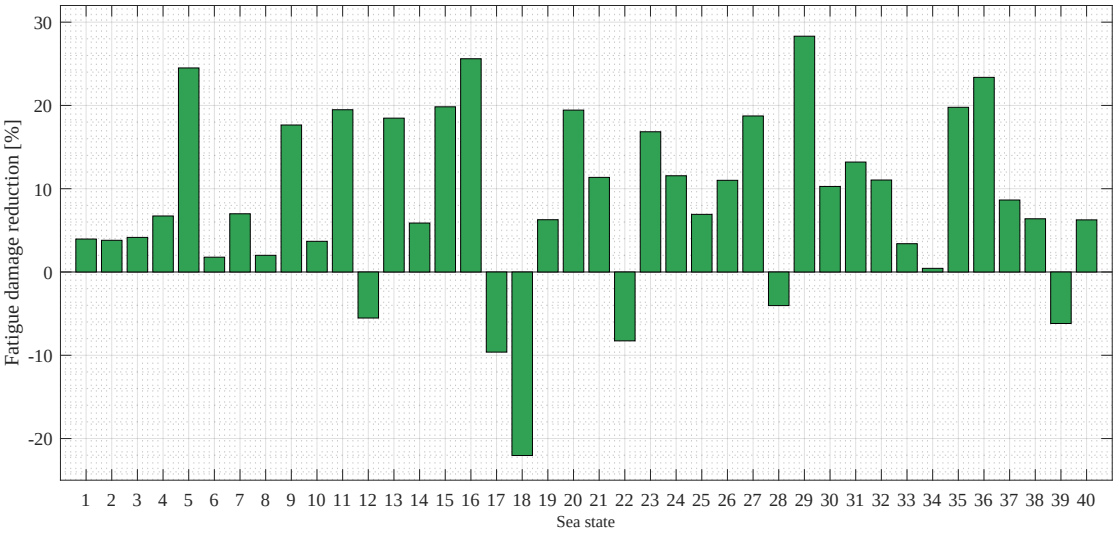

Figure 5.8: Relative fatigue reduction due to co-location

Although the differences are small in some cases, the fatigue damage in the mooring cables in the co-located case is almost always less compared with when the FOWT is deployed alone. The reduction in fatigue damage is in part due to the physical shadowing effect of the WEC, but also in part due to the absorption of energy.

Figure 5.9 illustrates an example of displacement and tension time series, comparing the FOWT-only and co-located cases. Although the two simulations were run with different random phases, and so the time series are not simply scaled versions of each other, it is still possible to draw some conclusions.

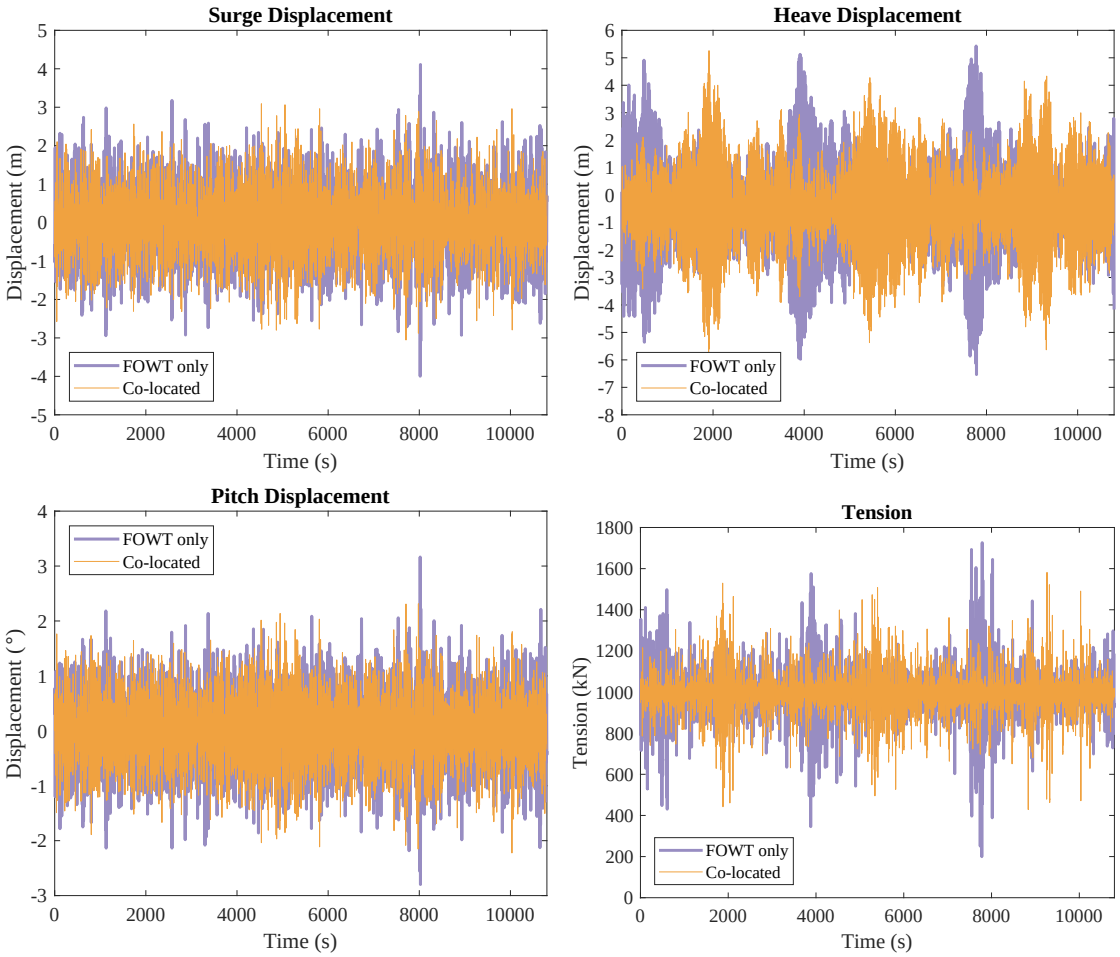

Figure 5.9: Example of displacement and tension time series: Case 19

The first conclusion is that there is correlation between the surge and pitch motions, and a correlation between the heave motion and the tension. Most of the tension variation seems to be driven by the heave motion. This could be due to heave motion having larger displacement amplitudes than surge. Realistically, second-order drift forces, an excitation in the surge direction, have a significant influence in the tension. These second-order drift forces, however, are not accounted

for in WEC-Sim, and have yet to be incorporated into these types of simulation codes. To validate whether heave and tension variation are strongly correlated, second-order drift forces would need to be considered, but this requires model advancements not currently available.

In the surge and pitch motions, although there is a small difference in the displacement amplitudes between the two scenarios, the envelope of the displacements is, in general, smaller for the co-located case than for the FOWT-only case. The maximum displacements are also smaller in the co-located case than in the FOWT-only case. This explains part of the reduction in fatigue damage caused by the shielding effect of the WEC on the FOWT.

For heave, the maximum value of the displacement happens in the co-located case. However, this only occurs once. In general, for both heave and tension time series, the motion amplitudes are smaller in the co-located case than in the FOWT-only case, as can be seen in both the heave displacement and tension timeseries envelopes for the FOWT-only and co-located case. As heave is the main driver of the tension, the smaller heave amplitude could explain the reduced fatigue damage in the co-located case when compared with the FOWT-only case.

These results indicate the potential for WECs to benefit FOWT reliability. While the case of placing a WEC 840 m in front of the FOWT showed fatigue reductions, this distance may not be realistic for developers. More realistically, developers would want to produce as much power in the leased ocean space as possible (which usually means placing as many devices as possible in the space), while still maintaining space between devices for O&M vessels. I hypothesize

that reducing the distance between the WEC and FOWT would decrease fatigue damage further without compromising structural safety or O&M logistics.

Moreover, I hypothesize that placing a multi-WEC array in front of the FOWT would result in further fatigue reduction compared to the case study analyzed here. More realistically, commercial realization of both technologies will be on the scale of larger arrays, from tens to hundreds of devices. When arrays are instituted, with more devices to reflect and absorb energy, the effect on the sea state will presumably be different (larger). Therefore, large array-scale experiments are investigated in Section 5.3.2 to measure the realistic impact of a co-located WEC and FOWT array.

5.3.2 Comparison of WEC Array Size and Separation Distance

In this section, results compare the fatigue damage across the three mooring cables for varying WEC array sizes and separation distances between the WEC array and FOWT.

First, I compare the estimated lifetime of the mooring cables given the sea state (and thus fatigue) reduction across separation distances and WEC array sizes for each cable. Cycles to failure, or the life of the mooring chain, is determined via the SN-curve established in equation 5.1 These resulting estimations are depicted in Figure 5.10.

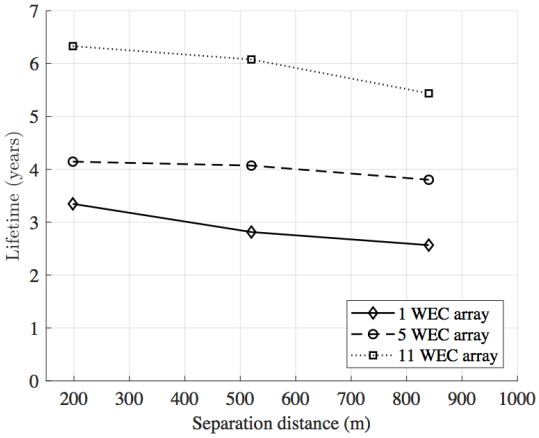

(a) Cable 1

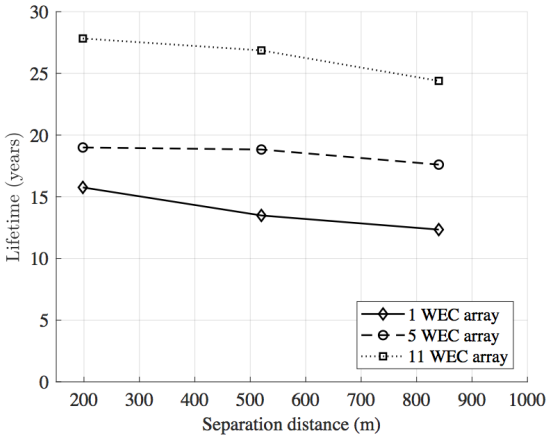

(b) Cable 2

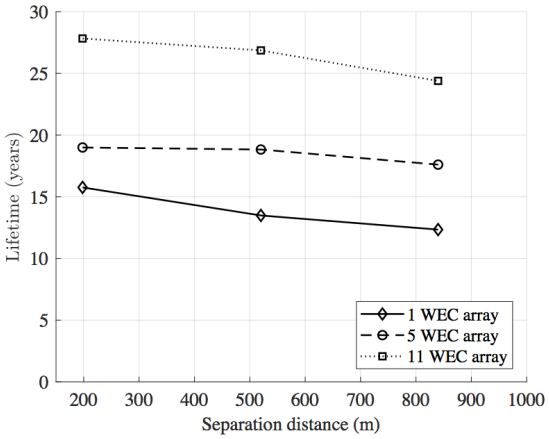

(c) Cable 3

Figure 5.10: Lifetime fatigue damage to the three mooring cables for varying separation distances and WEC array sizes

Figure 5.10a, 5.10b, and 5.10c show two main patterns. First, as WEC array size increases, the mooring cable lifetime increases. This is thought to be due to increasing number of WECs reducing the sea state, and therefore the fatigue damage. Second, as separation distance increases, the mooring cable lifetime decreases.

This is due to the "shadow" of the WEC array with decreased sea state recovering with distance from the array.

The magnitude differences are of particular interest. Cable 1 is the most seaward cable and thus experiences the greatest loads. This increased loading equates to a decreased lifetime equal to one-fifth of that experienced by the other cables. Cable 2 and 3 experience nearly equal loading, so that their lifetime plots appear nearly identical. This is due to the symmetry of their location (being equidistant from Cable 1) and to the regular, unidirection wave conditions implemented (so that Cable 2 and 3 both are equally oriented towards the oncoming wave direction, and are not experiencing irregular waves).

The majority of the cable lifetime estimates fall below the expected design life of 20 years. This suggests that the generalization of the design as in the OC4 project is not suitable. This generalization was thought acceptable originally because of the focus of this study on fatigue loads, rather than ultimate limit states caused by extreme conditions; Fatigue damage is caused mostly by commonly-occurring sea states, which do not require the total load bearing capacity of the mooring systems, as extreme sea states do. However, for the deep North Sea site we used off the coast of Norway, where the sea state conditions are much larger than in the more protected part of the North Sea (even for nominal sea states, which drive fatigue loads), for which most standards are written and reference turbines are designed. Relative to the baseline however, all co-located arrays have an increased lifetime. In the cases of reduced separation distances and a large WEC array, the lifetime is extended to meet or exceed the design life of Cable 2 and 3.

This is in accordance with the maximum tension calculations from the tension time series for each cable, shown in Figure 5.11.

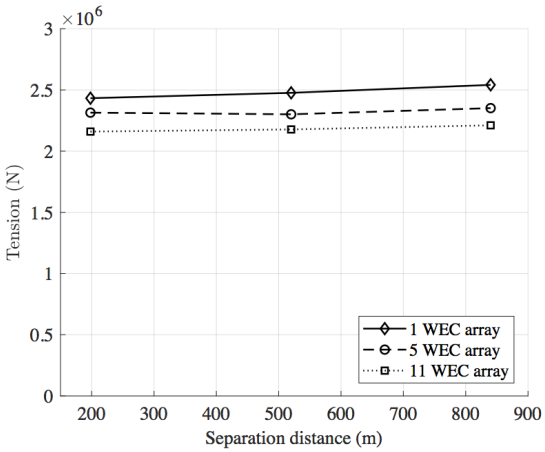

(a) Cable 1

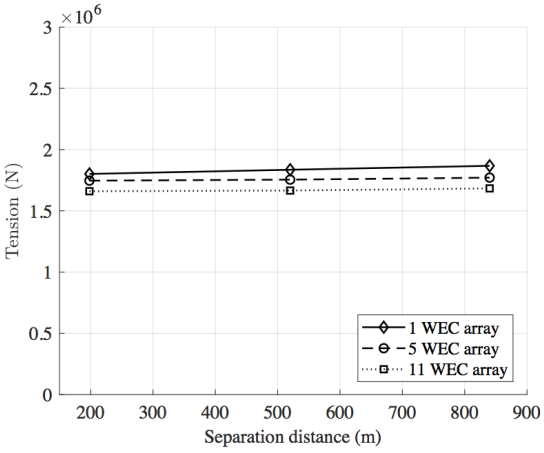

(b) Cable 2

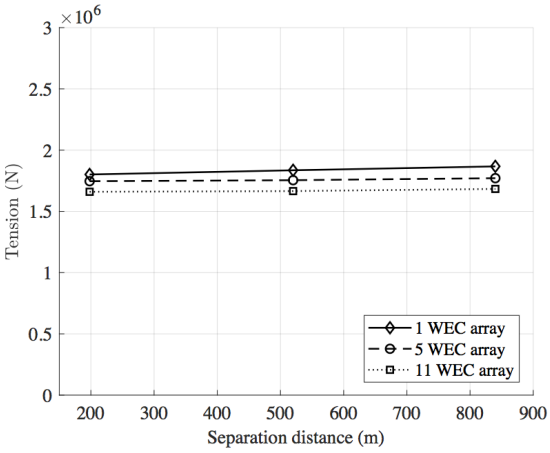

(c) Cable 3

Figure 5.11: Maximum tension experienced by the three mooring cables for varying separation distances and WEC array sizes

In Figure 5.11, Cables 2 and 3 show similar tension patterns across separation distances and WEC array size. Cable 1 shows increased tension, and also variation

in tension between the three array sizes and across separation distances.

5.4 Limitations and Future Work

While this study shows co-location of WECs and FOWTs in the same ocean space can reduce fatigue damage in FOWT mooring cables, there are aspects of this investigation that can be further explored.

Due to the limitations of the simulations tools, drift forces were not accounted for, even though they are responsible for a significant portion of the load on mooring cables. However, since the WEC blocks and absorbs energy, it is expected that second order loading caused by drift forces to decrease (or in the worst case, remain constant). As such, even in more detailed simulations, co-location can still be expected to reduce fatigue damage. Investigating the sensitivity of fatigue damage reduction to drift forces requires further consideration.

Effects of wind and current were also not accounted for in this analysis. WECs have a small draught and freeboard when compared with FOWTs. Therefore, they are not expected to have a significant effect on current and wind loading. It is important to note that wind loading will change the magnitude of the fatigue damage, and thus the relative impact the WEC has on percent fatigue reduction.

As a final note, the fatigue reduction experienced by the FOWT mooring must be considered in the context of the entire system's performance. The WaveCat does change shape, collapsing its two arms, when sea states increase beyond its optimal power producing range. This kind of shutdown, in the presence of extreme wave

conditions or simply larger nominal wave conditions, would cause short periods of increased fatigue damage. Likewise, this would also occur if the WEC was being repaired or maintained.

The design of the device used in this study is such that its power production is less influenced by its mooring system. However, in other WEC designs–in particular wave activated buoys and point absorbers–the performance depends on the mooring system. When considering the complex relationship between mooring, fatigue reduction, and cost in co-located arrays, the optimal solution becomes context-dependent. Cost reductions from co-locating WECs and FOWTs might enhance each technologies' viability. Conversely, the cost and complications associated with these novel technologies might outweigh the benefits of co-location, which could endanger the viability of their deployment.

An analysis of fatigue reduction, such as the one completed in this study, must be considered as part of a full technical and economic appraisal in which the specific context of the project is considered. Then, offshore renewable energy stakeholders can fully weigh the potential benefits of reducing fatigue damage in mooring cables with the risks associated with co-location.

5.5 Conclusions

In this study, I quantified the effect of co-located arrays on the fatigue damage of FOWT mooring cables by comparing fatigue damage in co-located and FOWT-only systems. The location selected for the study was offshore Norway, with wave

height and period based on site-specific data, but simplified to be uni-directional for the purposes of this study, approaching from the west. With summarized sea states for this location, I used SWAN to generate wave spectra at the location of the FOWT. I then input the spectra in a coupled floating body-mooring cable solver (WEC-Sim and MooDy) to simulate the dynamic behaviour of the moored FOWT. From the simulated behavior, I calculated and compared the fatigue and lifetime of the FOWT mooring cables with and without WECs placed seaward of the FOWT.

Based on these methods, I verified that co-location reduces the fatigue damage in the seaward FOWT mooring cable by an average of 8.3% over the lifetime of the structure given the probability of characteristic sea states. The magnitude of the fatigue damage reduction varies proportionally with the characteristics of the sea state. As the WEC array size increases, so does the lifetime estimate of the cable. As the separation distance between the WEC array and the FOWT decreases, the lifetime of the cable decreases. By their magnitude, Cable 2 and 3 experience similar fatigue damage over their lifetime, whereas Cable 1 experiences much higher fatigue damage, resulting in a reduced lifetime.

These results provide insight into the benefits and limitations of co-location and mooring design. While co-location could have benefits for improved reliability of mooring cables through modification of wave height (and thus, heave displacement), the variation in fatigue damage between the cables is significant. Because of the use of unidirectional wave conditions, the seaward catenary had a significantly reduced life. Including more realistic wave conditions through the use of a

probabilistic wave rose that includes not only seasonal, but inter-annual variability, will be important in assessing the impact of the wave height reduction on Cables 2 and 3.

In future work, the inclusion of second order drift forces will result in more accurate loading and fatigue data. Current and wind loads can also be studied, although WECs are not expected to reduce the effects of the loads on the structure. The simulation of short-crested sea states, or inclusion of direction spreading, is fundamental for a better understanding of the effects of co-location.

The results of this study begin to quantify the effects of co-locating WECs and FOWTs, and enable later investigations into how co-location affects cable inspection and replacement intervals, optimal O&M planning, and cable design. The results from this study also ultimately enable stakeholders to discern the validity and value of future co-located array development. As floating offshore wind and wave energy technologies continue to advance towards commercialization, the potential effects of co-location need to be further investigated.

Chapter 6: Conclusions

This thesis is a collection of studies which explore ways of incorporating reliability into offshore renewable energy design and optimization through method development and analysis. This work suggests the value of applying a holistic framework for decision making considering system-level effects of component reliability, and conceptually demonstrates the validity of this analysis. Both the frameworks used for this reliability-based design optimization and their results contribute to the field of offshore renewable energy design, and provide stakeholders (mainly researchers, designers, and developers) with information and methods to make more informed decisions.

The first study chronicles the development and results of a reliability-based layout optimization framework for offshore wind energy systems. In this study, a surrogate model is developed to estimate planet bearing L_{10} and power production from a given wind array layout. This reliability analysis framework is then wrapped into a gradient-based optimization algorithm for computationally-efficient optimization based on those L_{10} and power production values. This framework enables the incorporation of reliability into the objective function of wind array layout optimization, and also highlights the key ways in which this kind of framework benefits the understanding of the wind energy community, and also its limitations as one of the first forays into this kind of work.

Incorporating reliability again as an objective rather than a constraint in an optimization problem, the second study describes fatigue analysis and geometry optimization method development and implementation for reliability-based geometry optimization of a point absorber type WEC. Results indicate that geometry, size, oscillation direction, and site-specific wave conditions all affect damage equivalent loads and power production of a WEC. Further, the study indicates that not only general shape (barge, sphere, cylinder), but also more variable geometries (concavity and convexity, non-symmetrical) impact these two objectives. The impact of this study is two-fold. First, the study underlines the importance of considering reliability dynamically in the early design of WECs for more optimal solutions. Second, this study makes available a means by which to complete this kind of work, with the aspiration of aiding developers and researchers in WEC design.

The last two studies of this thesis explore the special use case of co-locating offshore wind turbines (both floating and fixed) and WECs in the same ocean space for the purpose of reduced fatigue loading on monopile and mooring chain. Effects of co-location are relatively unknown, thus these studies provide some insight into the potential benefits and risks associated with this kind of development.

Limitations specific to each study have been described in each corresponding chapter, however, there are overarching advances of this work that have yet to be realized that I want to describe here.

The specificity, granularity, and context-dependency that is required to demonstrate these methods and produce accurate results juxtapose the need for extensive system modeling and generalized methods to make results actionable for offshore

renewable energy developers. Outlined future work details plans to expand this work to incorporate more realistic conditions and more components, as well as to make the methods accessible for others' development so that they can expand the work. Despite these plans, there are still areas which require further development to ensure these methods and results are relevant and impactful to the offshore renewable energy community.

One of these areas revolves around the differences in risk- and reliability-based design optimization methods, both of which this dissertation includes. Reliability-based methods incorporate the probability of a component's failure into design optimization. Risk-based methods introduce consequence associated with that failure into design optimization. While an attempt was made to move towards risk-based analyses, risk requires definition of consequence, and is context-dependent. In future work, I want to continue to seek ways to incorporate risk that affect the offshore renewable energy industry, while creating methods and tools others can adapt to their own context-specific uses.

Second, the pace at which this work can be developed, the pace at which this work can be adopted and adapted within industry, the pace to generate accurate, complete, and relevant results to inform decision-makers, and the pace at which developers make their decisions are currently not congruent. For instance, in the time it took to develop the reliability-based layout optimization techniques, the largest offshore wind turbine available on market increased by several MW capacity, with its design moving from a gearbox design, in which planet bearings are integral, to a direct drive system. The reference turbine used in this same study is now smaller

than the average wind turbine installed offshore. To further complicate, the use of well-studied, validated models like the NREL 5MW turbine drivetrain are critical to developing models like those developed in this dissertation and producing accurate, trustworthy results. However, the very frameworks I developed are most impactful in the early design of emerging technologies, for which there are few models with limited testing and validation. Therefore, there is a need to 1) distill the lessons learned from these studies so that they can govern future model development in research and industry, 2) generalize the framework of these methods so that others can better adapt them to an increasingly wide range of component and system designs, 3) hone the computational methods that underlie the conceptual framework of system design so that they run at maximum efficiency while also retaining relevant accuracy and resolution, and are robust enough to withstand different levels of fidelity for different components, and 4) enable these frameworks to account for different forms of information, not just analytical models, but potentially data-driven models, expert knowledge, or probabilistic frameworks. It is important to not only discover what drives reliability-based systems design, but to also create lasting frameworks with which to determine those drivers as new designs emerge.

While offshore renewable energy technologies are at various stages of development on their way to commercial viability and cost competitiveness, I argue that incorporating reliability more dynamically in early design could benefit all technologies. By moving reliability from a constraint to an objective, the methods included in this dissertation expand current reliability-based design optimization

methods. Further, this dissertation suggests a holistic approach to systems design and decision making in offshore renewable energy systems, and conceptually demonstrates methods to do so by incorporating reliability into systems design.

In the coming decades, the world will continue to be challenged to provide equitable, affordable, and modern energy services while increasing renewable energy shares in global energy production. With further research, offshore renewable energy has the potential to fundamentally shift the national and global energy portfolio. Exploring how to improve reliability and power production while reducing cost of energy for these technologies will help dissolve implementation barriers for offshore renewable energy, enabling policy makers and developers to make informed economic decisions.

Bibliography

[1] J. Abanades, D. Greaves, and G. Iglesias. Wave farm impact on the beach profile: A case study. *Coast. Eng.*, 86:36–44, 2014.

[2] K. A. Abhinav and Nilanjan Saha. Dynamic analysis of an offshore wind turbine including soil effects. *Procedia Eng.*, 116(1):32–39, 2015.

[3] Simon Ambühl, Morten Kramer, and John Dalsgaard Sørensen. Reliability-Based Structural Optimization of Wave Energy Converters. *Energies*, 7:8178–8200, 2014.

[4] Tino Andresen. Offshore Wind Farms Offer Subsidy-Free Power for First Time, 2017.

[5] Sharay Astariz, C. Perez-Collazo, J. Abanades, and G. Iglesias. Towards the optimal design of a co-located wind-wave farm. *Energy*, 84:15–24, may 2015.

[6] Sharay Astariz Núñez. *Combined wave and wind energy : synergies and implementation*. PhD thesis, Universidade de Santiago de Compostela, 2016.

[7] A Babarit and A H Clément. Shape optimisation of the SEAREV wave energy converter. *9$ˆ{th}$ World Renew. Energy Congr.*, 2006.

[8] A. Babarit, J. Hals, M.J. Muliawan, A. Kurniawan, T. Moan, and J. Krokstad. Numerical benchmarking study of a selection of wave energy converters. *Renew. Energy*, 41:44–63, may 2012.

[9] Christian Bak, Frederik Zahle, Robert Bitsche, Taeseong Kim, Anders Yde, Lars Christian Henriksen, Morten Hartvig Hansen, José Pedro Albergaria Amaral Blasques, Mac Gaunaa, and Anand Natarajan. The dtu 10-mw reference wind turbine. In *Danish Wind Power Research 2013*, 2013.

[10] Pedro Jorge Borges Fontes Negrão Beirão and Cândida Maria dos Santos Pereira Malça. Design and analysis of buoy geometries for a wave energy converter. *Int. J. Energy Environ. Eng.*, 5(2-3):91, jul 2014.

[11] Nuno Bento and Margarida Fontes. Emergence of floating offshore wind energy: Technology and industry. *Renew. Sustain. Energy Rev.*, 99(February 2018):66–82, 2019.

[12] Subhamoy Bhattacharya. Challenges in Design of Foundations for Offshore Wind Turbines. *Eng. Technol. Ref.*, pages 1–9, 2014.

[13] Marcos Blanco, Pablo Moreno-Torres, Marcos Lafoz, and Dionisio Ramírez. Design parameter analysis of point absorber WEC via an evolutionary-algorithm-based dimensioning tool. *Energies*, 8(10):11203–11233, 2015.

[14] RBJ Brinkgreve, E Engin, WM Swolfs, D Waterman, A Chesaru, PG Bonnier, and V Galavi. Plaxis 3d 2012. *Plaxis bv*, 2012.

[15] Marshall Buhl. The NWTC Design-Codes Suite: An Overview. *43rd AIAA Aerosp. Sci. Meet. Exhib.*, pages 1–11, 2005.

[16] Maria Campbell, Jiska De Groot, Matthew Ashley, and Lynda Rodwell. The Fisheries and Marine Renewable Energy Working Group : creating an agenda for improved co-existence. page 33, 2014.

[17] R Carballo, N Arean, M Sanchez, V Ramos, M Alvarez, A Castro, and G Iglesias. Intra-annual power performance of WECs : a decision-aid tool for wave farm planning. pages 2–8, 2017.

[18] James Carroll, Alasdair McDonald, and David McMillan. Failure rate, repair time and unscheduled O&M cost analysis of offshore wind turbines. *Wind Energy*, 19(August 2015):1107–1119, 2016.

[19] M. Casale, C.; Serri, L.; Stolk, N.; Yildiz, I.; Cantu. Synergies , innovative designs and concepts for multipurpose use of conversion platforms. Technical report, 2011.

[20] Grace Chang, Jason Magalen, Craig Jones, and Jesse Roberts. Investigation of Wave Energy Converter Effects on Wave Fields : A Modeling Sensitivity Study in Monterey Bay , CA. page 65, 2014.

[21] Caitlyn E Clark. *Offshore Renewable Energy: An Exploration of Techno-Economic Feasibility and Reliability through a Computational Optimization Perspective*. Master of science, Oregon State University, 2017.

[22] Caitlyn E Clark. RBLO (Reliability-Based Layout Optimization) Repository, 2019.

[23] Caitlyn E Clark and Bryony DuPont. Reliability-based design optimization in offshore renewable energy systems. *Renew. Sustain. Energy Rev.*, 97(June):390–400, 2018.

[24] Caitlyn E Clark, Annalise Miller, and Bryony DuPont. Analytical Cost Modeling for Co-Located Wind-Wave Energy Arrays. *Eur. Wave Tidal Energy Conf.*, Submitted:1–11, 2017.

[25] Simon Claus. *MERMAID: Innovative Multi-Purpose Offshore Platforms*. 2014.

[26] Ryan Coe, Yi-Hsiang Yu, Jennifer van Rij, Ryan G. Coe, Yi-Hsiang Yu, and Jennifer van Rij. A Survey of WEC Reliability, Survival and Design Practices. *Energies*, 11(1):4, dec 2017.

[27] International Electrotechnical Commission et al. Iec 61400-3. *Wind Turbines—Part 3: Design Requirements for Offshore Wind Turbines*, 2009.

[28] Bill Cooper and Frank Beiboer. Potential Effects of Offshore Wind Developments on Coastal Processes. Technical report, ABP Marine Environmental Research Ltd, 2002.

[29] Odeh Dababneh, Timoleon Kipouros, and James F. Whidborne. Application of an efficient gradient-based optimization strategy for aircraft wing structures. *Aerospace*, 5(1):1–27, 2018.

[30] DNV. RP-C203- Fatigue design of offshore steel structures. *Recomm. Pract. DNV-RPC203*, (October):126, 2014.

[31] DNV-GL. Offshore Standard DNV-OS-E-301 - Position Mooring, 2010.

[32] DNV-GL. OS-J103 Design of Floating Wind Turbine Structures. (June):124, 2013.

[33] Christopher N Elkinton, James F Manwell, and Jon G McGowan. Offshore Wind Farm Layout Optimization (OWFLO) Project: Preliminary Results. *44th AIAA Aerosp. Sci. Meet. Exhib. Reno, Nevada, Jan. 2006*, pages 1–9, 2006.

[34] Christopher N Elkinton, James F Manwell, and Jon G Mcgowan. Algorithms for Offshore Wind Farm Layout Optimization. *Wind Eng.*, 32(1):67–84, 2008.

[35] U.S. Office of Energy Efficiency Energy and Renewable. Inside a Wind Turbine, 2019.

[36] European Marine Observation and Data Network. EMODNet Bathymetry, 2017.

[37] Peter Fairly. China's Potent Wind Potential. *MIT Technol. Rev.*, sep 2009.

[38] H. Fernandez, G. Iglesias, R. Carballo, A. Castro, J.A. Fraguela, F. Taveira-Pinto, and M. Sanchez. The new wave energy converter WaveCat: Concept and laboratory tests. *Mar. Struct.*, 29(1):58–70, dec 2012.

[39] Julia Fernández Chozas, Jens Peter Kofoed, and H.C. Sorensen. Predictability and Variability of Wave and Wind Wave and Wind Forecasting and Diversified Energy Systems in the Danish North Sea. 2013.

[40] Julia Fernández Chozas, H.C. Sorensen, and N.E. Helstrup Jensen. Economic Benefit of Combining Wave and Wind Power Productions in Day-Ahead Electricity Markets. *4th Int. Conf. Ocean Energy*, 2012.

[41] Christos Galinos, Nikolay Dimitrov, Torben J Larsen, Anand Natarajan, and Kurt S Hansen. Mapping Wind Farm Loads and Power Production - A Case Study on Horns Rev 1. *J. Phys. Conf. Ser.*, 753:032010, 2016.

[42] Xiaoxia Gao, Hongxing Yang, Lu Lin, and Prentice Koo. Wind turbine layout optimization using multi-population genetic algorithm and a case study in Hong Kong offshore. *J. Wind Eng. Ind. Aerodyn.*, 139:89–99, 2015.

[43] Nikolay T. Garabedian, Benjamin J. Gould, Gary L. Doll, and David L. Burris. The cause of premature wind turbine bearing failures: Overloading or underloading?, 2018.

[44] Elizabet Garcia. H2OCEAN Report Summary: Periodic Report Summary 1. Technical report, AWS Trupower SL, Spain, 2014.

[45] Anna Garcia-Teruel. Progress Report for 2nd Annual Review : Cost and Perfomance Optimization of Wave Energy Converters, 2017.

[46] Anna Garcia-Teruel. *Cost and Performance Optimization of Wave Energy Converters*. Doctoral, The University of Edinburgh, 2020.

[47] Anna Garcia-Teruel and David Forehand. Optimal wave energy converter geometry for different modes of motion. In *Adv. Renew. Energies Offshore Proc. 3rd Int. Conf. Renew. Energies Offshore (RENEW 2018)*, pages 299–305, Lisbon, 2018.

[48] Pieter Gebraad, Jared J. Thomas, Andrew Ning, Paul Fleming, and Katherine Dykes. Maximization of the annual energy production of wind power plants by optimization of layout and yaw-based wake control. *Wind Energy*, 2017.

[49] Global Wind Energy Council. GWEC Global Wind 2017 report—A Snapshot of Top Wind Markets in 2017: Offshore Wind. Technical report, 2018.

[50] B. J. Gould and D. L. Burris. Effects of wind shear on wind turbine rotor loads and planetary bearing reliability. *Wind Energy*, 2016.

[51] Yi Guo, Jonathan Keller, and William LaCava. Planetary gear load sharing of wind turbine drivetrains subjected to non-torque loads. *Wind Energy*, 18:757–768, 2015.

[52] Matthew Hall and Andrew Goupee. Validation of a lumped-mass mooring line model with DeepCwind semisubmersible model test data. *Ocean Engineering*, 104:590–603, 2015.

[53] Xiaoqing Han, Jing Guo, Peng Wang, and Yanbing Jia. Adequacy study of wind farms considering reliability and wake effect of WTGs. *IEEE Power Energy Soc. Gen. Meet.*, (1):1–7, 2011.

[54] Gordon Hughes. The Performance of Wind Farms in the United Kingdom and Denmark. *Renew. Energy Found. London, UK*, page 52, 2012.

[55] IEC 61400-3. Wind turbines - Part 3: Design requirements for offshore wind turbines. Technical report, 2009.

[56] Bryce Taylor Ingersoll. *Efficient Incorporation of Fatigue Damage Constraints in Wind Turbine Blade Optimization*. Master of science, Brigham Young University, 2018.

[57] International Renewable Energy Agency (IRENA). Renewable Power Generation Costs in 2017. Technical report, 2014.

[58] IRENA International Renewable Energy Agency. *Renewable Power Generation Costs in 2017*. 2018.

[59] Carlos M. Ituarte-Villarreal and Jose F. Espiritu. Optimization of wind turbine placement using a viral based optimization algorithm. *Procedia Comput. Sci.*, 6:469–474, 2011.

[60] P. Jacobson, G. Hagerman, and G. Scott. Mapping and Assessment of the United States Ocean Wave Energy Resource. Technical report, Electric Power Research Institute, Palo Alto, CA, 2011.

[61] B. J. Jonkman. TurbSim User's Guide Version 2.0. Technical Report October, National Renewable Energy Laboratory, Golden, CO, 2018.

[62] J M Jonkman. FAST.Farm User's Guide and Theory Manual. Technical report, National Renewable Energy Laboratory, Golden, CO.

[63] J. M. Jonkman, S Butterfield, W Musial, and G Scott. Definition of a 5-MW reference wind turbine for offshore system development. Technical Report February, National Renewable Energy Laboratory, Golden, CO, 2009.

[64] J Keller, Y Guo, W Lacava, and H Link. Gearbox Reliability Collaborative Phase 1 and 2: Testing and Modeling Results Preprint. *Leuven Conf. Noise Vib. Eng.*, (May), 2012.

[65] Hagkwen Kim, Chanan Singh, and Alex Sprintson. Simulation and estimation of reliability in a wind farm considering the wake effect. *IEEE Trans. Sustain. Energy*, 3(2):274–282, 2012.

[66] Alexios Koltsidopoulos Papatzimos, Tariq Dawood, and Philipp R. Thies. Data Insights from an Offshore Wind Turbine Gearbox Replacement. *J. Phys. Conf. Ser.*, 1104(1), 2018.

[67] Adi Kurniawan and Torgeir Moan. Optimal geometries for wave absorbers oscillating about a fixed axis. *IEEE J. Ocean. Eng.*, 38(1):117–130, 2013.

[68] Torben J Larsen and Anders Melchior Hansen. How 2 hawc2, the user's manual. 2007.

[69] Lin Li, Zhen Gao, and Torgeir Moan. Joint Environmental Data at Five European Offshore Sites for Design of Combined Wind and Wave Energy Devices. *Vol. 8 Ocean Renew. Energy*, 8(7491):V008T09A006, 2013.

[70] Feng Liu and Zhifang Wang. Offshore Wind Farm Layout Optimization Using Adapted Genetic Algorithm: A different perspective. 2014.

[71] Jakob Mann. Wind field simulation. *Probabilistic engineering mechanics*, 13(4):269–282, 1998.

[72] Will Mathis and Christian Wienberg. Offshore Wind Gets a Warning from Its Biggest Developer. *Bloomberg*, oct 2019.

[73] Wayne Mays. Personal Correspondence, Avangrid Renewables, 16 March, 2017.

[74] A.P. McCabe. Constrained optimization of the shape of a wave energy collector by genetic algorithm. *Renew. Energy*, 51:274–284, mar 2013.

[75] G. Mosetti, C. Poloni, and B. Diviacco. Optimization of wind turbine positioning in large windfarms by means of a genetic algorithm. *J. Wind Eng. Ind. Aerodyn.*, 51(1):105–116, 1994.

[76] Guilherme Moura Paredes, Claes Eskilsson, Johannes Palm, Jens Peter Kofoed, and Lars Bergdahl. Coupled BEM/hp-FEM Modelling of Moored Floaters. In *Submitted to The First Vietnam Symposium on Advances in Offshore Engineering*, page 6, Hanoi, 2018.

[77] Anders Myhr, Catho Bjerkseter, Anders Ågotnes, and Tor A. Nygaard. Levelised cost of energy for offshore floating wind turbines in a life cycle perspective. *Renew. Energy*, 66:714–728, 2014.

[78] National Renewable Energy Laboratory. 2016 Offshore Wind Technologies Market Report. Technical report, U.S. Department of Energy, 2016.

[79] National Renewable Energy Laboratory and Sandia Corporation. WEC-Sim (Wave Energy Converter SIMulator) — WEC-Sim documentation, 2015.

[80] Amir Rasekhi Nejad, Yi Guo, Zhen Gao, and Torgeir Moan. Development of a 5 MW reference gearbox for offshore wind turbines. *Wind Energy*, (19):1089–1106, 2016.

[81] New Energy Update. Wind Turbine Common Failures and Solutions. In *Wind O&M Canada 2017*, Toronto, CA, 2017.

[82] AW Nielsen, BM Sumer, and TU Petersen. Sinking of scour protections at Horns Rev 1 offshore wind farm. *Coast. Eng.*, pages 1–14, 2014.

[83] Jannie Sønderkær Nielsen. *Risk-based operation and maintenance of offshore wind turbines*. Number February. 2013.

[84] S. Andrew Ning, Rick Damiani, and Patrick J. Moriarty. Objectives and constraints for wind turbine optimization. *J. Sol. Energy Eng. Trans. ASME*, 2014.

[85] Wind Energy Technologies Office. Statistics Show Bearing Problems Cause the Majority of Wind Turbine Gearbox Failures, 2015.

[86] U. Aytun Ozturk and Bryan a. Norman. Heuristic methods for wind energy conversion system positioning. *Electr. Power Syst. Res.*, 70(3):179–185, 2004.

[87] Johannes Palm and Claes Eskilsson. MooDy - Mooring Dynamics, 2018.

[88] Johannes Palm, Claes Eskilsson, and Lars Bergdahl. An hp-adaptive discontinuous Galerkin method for modelling snap loads in mooring cables. *Ocean Engineering*, 144(September):266–276, 2017.

[89] Beatriz Pérez, Roberto Mínguez, and Raúl Guanche. Offshore wind farm layout optimization using mathematical programming techniques. *Renew. Energy*, 53:389–399, may 2013.

[90] Carlos Pérez-Collazo, D. Greaves, and G. Iglesias. A review of combined wave and offshore wind energy. *Renew. Sustain. Energy Rev.*, 42:141–153, feb 2015.

[91] Daniele Peri and Federica Tinti. A multistart gradient-based algorithm with surrogate model for global optimization. *Commun. Appl. Ind. Math. Vol 3, No 1*, pages 1–22, 2012.

[92] Georg Pirrung, Helge Madsen, and Scott Schreck. Trailed vorticity modeling for aeroelastic wind turbine simulations in stand still. *J. Phys. Conf. Ser.*, 753(4), 2016.

[93] S. Ponce de León, J. H. Bettencourt, and N. Kjerstad. Simulation of irregular waves in an offshore wind farm with a spectral wave model. *Cont. Shelf Res.*, 31(15):1541–1557, 2011.

[94] Sittichoke Pookpunt and Weerakorn Ongsakul. Optimal placement of wind turbines within wind farm using binary particle swarm optimization with time-varying acceleration coefficients. *Renew. Energy*, 55:266–276, jul 2013.

[95] E Quevedo, M Cartón, E Delory, A Castro, J Hernández, O Llinás, J Bard, J De Lara, H Jeffrey, and D Ingram. Multi-use offshore platform configurations in the scope of the FP7 TROPOS Project. In *MTS IEEE Ocean.*, number 288192, Bergen (Norway), 2013.

[96] J. Quick, K. Dykes, P. Graf, and F. Zahle. Optimization under Uncertainty of Site-Specific Turbine Configurations. In *J. Phys. Conf. Ser.*, 2016.

[97] Pierre-Elouan Réthoré, Peter Fuglsang, Gunner C Larsen, Thomas Buhl, Torben J Larsen, and Helge A Madsen. TopFarm: Multi-fidelity Optimization of Offshore Wind Farm. *ISOPE Int. Soc. Offshore Polar Eng. 2011.*, (2007):516–524, 2011.

[98] Rajai Aghabi Rivas, Jens Clausen, Kurt S. Hansen, and Leo E. Jensen. Solving the Turbine Positioning Problem for Large Offshore Wind Farms by Simulated Annealing. *Wind Eng.*, 33(3):287–297, 2009.

[99] A. Robertson, J. Jonkman, M. Masciola, H. Song, A. Goupee, A. Coulling, and C. Luan. Definition of the Semisubmersible Floating System for Phase II of OC4. Technical report, National Renewable Energy Laboratory, Golden, CO, 2014.

[100] A. Robertson, J. Jonkman, F. Wendt, A. Goupee, and H. Dagher. Definition of the OC5 DeepCwind Semisubmersible Floating System. Technical report, 2016.

[101] Amy Robertson, Latha Sethuraman, Jason Jonkman, and Julian Quick. Assessment of Wind Parameter Sensitivity on Ultimate and Fatigue Wind Turbine Loads: Preprint. (February):23, 2018.

[102] S.F. Rodrigues, R. Teixeira Pinto, M. Soleimanzadeh, Peter A.N. Bosman, and P. Bauer. Wake losses optimization of offshore wind farms with moveable floating wind turbines. *Energy Convers. Manag.*, 89:933–941, jan 2015.

[103] S. Salcedo-Sanz, D. Gallo-Marazuela, a. Pastor-Sánchez, L. Carro-Calvo, a. Portilla-Figueras, and L. Prieto. Offshore wind farm design with the Coral Reefs Optimization algorithm. *Renew. Energy*, 63:109–115, 2014.

[104] Marc Schwartz, Donna Heimiller, and Steve Haymes. Assessment of Offshore Wind Energy Resources for the United States. *Natl. Renew. Energy Lab.*, (June):NREL/TP–500–45889, 2010.

[105] SciPy.org. numpy.histogram, 2019.

[106] S. Sheng, M. McDade, and R. Errichello. Wind Turbine Gearbox Failure Modes - A brief. Technical report, 2011.

[107] SKF. Equivalent Dynamic Load, 2019.

[108] Mikel Sojo Armentia and Gunther Auer. MARINA Platform Final Summary Report. Technical report, 2014.

[109] J. D. Sørensen, S. Frandsen, and N. J. Tarp-Johansen. Effective turbulence models and fatigue reliability in wind farms. *Probabilistic Eng. Mech.*, 23(4):531–538, 2008.

[110] John Dalsgaard Sørensen. Optimal, reliability-based turbine placement in offshore wind turbine parks. *Civ. Eng. Environ. Syst.*, 24(2):99–109, 2007.

[111] Andrew P J Stanley, Jennifer King, and Andrew Ning. Wind Farm Layout Optimization with Loads Considerations. In *North Am. Wind Energy Assoc.*, Amherst, Massachusettes, 2019.

[112] Andrew P. J. Stanley and Andrew Ning. Coupled wind turbine design and layout optimization with nonhomogeneous wind turbines. *Wind Energy Sci.*, 2019.

[113] Bryan M. Stockton. INSIGHT: Unleashing the Potential of Offshore Wind, jun 2018.

[114] The SWAN Team. USER MANUAL SWAN - Cycle III version 41.01A, 2015.

[115] The WAFO Group. WAFO—a Matlab toolbox for analysis of random waves and loads. Technical Report March, Lund University, Lund, Sweden, 2011.

[116] Phlipp R Thies. *Reliability of wave energy converters*. 2009.

[117] Frank C Uherek. What is L10 Life?, 2018.

[118] U.S. Department of Energy. Wave Energy Prize, 2015.

[119] U.S. Office of Energy Efficiency and Renewable Energy. Advance Wind Turbine Drivetrain Trends and Opportunities, 2019.

[120] Jennifer van Rij, Yi-Hsiang Yu, Kathleen Edwards, and Mike Mekhiche. Ocean power technology design optimization. *Int. J. Mar. Energy*, 20:97–108, dec 2017.

[121] M Veigas, V Ramos, and G Iglesias. A wave farm for an island : Detailed effects on the nearshore wave climate. *Energy*, 69:801–812, 2014.

[122] Joey Velarde. Design of monopile foundations to support the dtu 10 mw offshore wind turbine. Master's thesis, NTNU, 2016.

[123] Joey Velarde. *Design of monopile foundations to support the DTU 10MW wind turbine*. Master of science, Norwegian University of Science and Technology, 2016.

[124] Joey Velarde and Erin E Bachynski. Design and fatigue analysis of monopile foundations to support the dtu 10 mw offshore wind turbine. *Energy Procedia*, 137:3–13, 2017.

[125] John Waegter. Stress range histories and Rain Flow counting. Number June, pages 1–13. 2009.

[126] John Waegter. Stress range histories and Rain Flow counting. Number June, pages 1–13. 2009.

[127] Musial Walter, Beiter Philipp, Paul Spitsen, Jake Nunemake, and Vahan Gevorgian. 2018 Offshore Wind Technologies Market Report. pages 1–94, 2019.

[128] Chunqiu Wan, Jun Wang, Geng Yang, and Xing Zhang. Particle swarm optimization based on Gaussian mutation and its application to wind farm micro-siting. *49th IEEE Conf. Decis. Control*, (2):2227–2232, 2010.

[129] Thomas Michael Welte, Iver Bakken Sperstad, Elin Espeland Halvorsen-Weare, Øyvind Netland, Lars Magne Nonås, and Magnus Stålhane. Operation and Maintenance Modelling. In Olimpo Anaya-Lara, John O. Tande,

Kjetil Uhlen, and Karl Merz, editors, *Offshore Wind Energy Technol.*, chapter Chapter 7:, pages 269–304. John Wiley & Sons Ltd., first edit edition, 2018.

[130] Fabian F Wendt, Morten Thøtt Andersen, Amy N Robertson, and Jason M Jonkman. Verification and Validation of the New Dynamic Mooring Modules Available in FAST v8. *26th Int. Ocean Polar Eng. Conf.*, (August):352–363, 2016.

[131] Sanne Wittrup. Horns Rev lærte Vattenfall lektien, 2015.

[132] Julian Wolfram. On Assessing the Reliability and Availability of Marine Energy Converters: The Problems of a New Technology. *Risk Reliab.*, 220, 2006.

[133] Yuan Kang Wu, Wen Chin Wu, and Jyun Jie Zeng. Key issues on the design of an offshore wind farm layout and its equivalent model. *Appl. Sci.*, 9(9), 2019.

[134] L.M. Yang, T. Hals, and T. Moan. A wear model for assessing the reliability of wave energy converter in heave with hydraulic power take-off. *Proc. 8th Eur. Wave Tidal Energy Conf.*, (September):874–881, 2009.

[135] Wenxian Yang, Shuangwen Sheng, and Richard Court. Operational-Condition-Independent Criteria Dedicated to Monitoring Wind Turbine Generators. *Int. J. Progn. Heal. Manag.*, 117(Special Issue on Wind Turbines PHM):1–8, 2013.

[136] Barbara Zanuttigh, Elisa Angelelli, Andreas Kortenhaus, Kaan Koca, Yukiko Krontira, and Phoebe Koundouri. A methodology for multi-criteria design of multi-use offshore platforms for marine renewable energy harvesting. *Renew. Energy*, 85:1271–1289, jan 2016.